

3-16-2022

Polarimetric Imaging of the Uterine Cervix

Mariacarla Gonzalez
mgonz211@fiu.edu

Follow this and additional works at: <https://digitalcommons.fiu.edu/etd>



Part of the [Bioimaging and Biomedical Optics Commons](#)

Recommended Citation

Gonzalez, Mariacarla, "Polarimetric Imaging of the Uterine Cervix" (2022). *FIU Electronic Theses and Dissertations*. 4927.

<https://digitalcommons.fiu.edu/etd/4927>

This work is brought to you for free and open access by the University Graduate School at FIU Digital Commons. It has been accepted for inclusion in FIU Electronic Theses and Dissertations by an authorized administrator of FIU Digital Commons. For more information, please contact dcc@fiu.edu.

FLORIDA INTERNATIONAL UNIVERSITY

Miami, Florida

POLARIMETRIC IMAGING OF THE UTERINE CERVIX

A dissertation submitted in partial fulfillment of the

requirements for the degree of

DOCTOR IN PHILOSOPHY

in

BIOMEDICAL ENGINEERING

by

Mariacarla Gonzalez

2022

To: Dean John L. Volakis
College of Engineering and Computing

This dissertation, written by Mariacarla Gonzalez, and entitled Polarimetric Imaging of the Uterine Cervix, having been approved in respect to style and intellectual content, is referred to you for judgment.

We have read this dissertation and recommend that it be approved.

Joshua Hutcheson

Wei-Chiang Lin

Anuradha Godavarty

Purnima Madhivanan

Jessica C. Ramella-Roman, Major Professor

Date of Defense: March 16, 2022

This dissertation of Mariacarla Gonzalez is approved.

Dean John L. Volakis
College of Engineering and Computing

Andres G. Gil
Vice President of Research and Economic Development
and Dean of the University Graduate School

Florida International University, 2022

©Copyright 2022 by Mariacarla Gonzalez

All rights reserved.

Authorship attribution statement:

This dissertation contains material from 3 published papers found in the following peer-reviewed journals:

Chapter 3 has been published by the Journal of Biomedical Optics as Mariacarla Gonzalez, Karla Montejo, Karl Krupp, Vijaya Srinivas, Edward DeHoog, Purnima Madhivanan, Jessica C. Ramella-Roman, titled as “Design and implementation of a portable colposcope Mueller matrix polarimeter”.

Chapter 4 has been published by the Journal of Physics D: Applied Physics as Mariacarla Gonzalez, Razvigor Ossikovski, Tatiana Novikova, Jessica C. Ramella-Roman, titled as “Introduction of a 3 x 4 Mueller matrix decomposition method”.

Chapter 1 is being submitted to a peer-reviewed journal as Mariacarla Gonzalez, Tananant Boonya-Ananta, Purnima Madhivanan, Jessica C. Ramella-Roman, titled as “Cervical imaging in the low resource setting: a review”.

DEDICATION

This dissertation is dedicated to my parents, Agustin and Jacqueline, who have moved heaven and earth for me to accomplish my goals. Their sacrifice of leaving everything behind to find freedom and new opportunities has bred one more success.

ACKNOWLEDGMENTS

I would like to thank my major advisor Dr. Jessica Ramella-Roman for the guidance and mentorship during this academic journey, as well as my committee members Dr. Wei-Chiang Lin, Dr. Anuradha Godavarty, Dr. Joshua Hutcheson and Dr. Purnima Madhivanan for their feedback and support. I am grateful for the continuous support from my lab members (past and present) and all my colleagues and close friends that have held a hand when in need.

I am thankful to Dr. Sonja Montas-Hunter, a mentor that never lost belief in me and always offered her support. I am also thankful for the supporting staff in the Biomedical Engineering department that is always willing to help, especially Claudia Estrada. Moreover, this journey would not have been possible without the Florida Education Fund McKnight fellowship that gave me the time and independence I needed to complete my work.

Last, but not least, I am eternally grateful for the best support system I could ask for: my parents, Agustin and Jacqueline, my brother Carlos, my boyfriend Cesar and my best friend Ivett. They have offered me endless support and unconditional love.

ABSTRACT OF DISSERTATION
POLARIMETRIC IMAGING OF THE UTERINE CERVIX

By

Mariacarla Gonzalez

Florida International University

Miami, Florida, 2022

Professor Jessica C. Ramella-Roman, Major Professor

Cervical cancer is the fourth most common cancer in women, with more than half a million women diagnosed each year due to persistent human papillomavirus (HPV) infection and a mortality of 311,000 women. According to the World Cancer Research Fund, developing countries have 84% of the global burden of the disease and 80% of the mortality due to a lack of effective screening programs. Several screening techniques have been developed and implemented to aid in low resource setting cervical screening, however, most require physician interpretation of color images. Other modalities utilize contrast agents to highlight pathological tissue but have small field of view. This dissertation investigates the use of polarimetric imaging techniques to image uterine cervix with particular focus to the needs of underserved communities.

We have used Mueller matrix imaging, to noninvasively image the uterine cervix *in vivo*. Mueller matrix (MM) can provide structural information of the cervix extracellular matrix (ECM) that could be leveraged for early diagnosis of cervical cancer and other pathologies of the uterine cervix. We have developed a Savart-based portable Mueller matrix polarimeter to conduct a pilot study to characterize polarimetrically healthy human cervixes. The results showed high depolarization and retardance, as is expected of healthy tissue.

The availability of new equipment, such as microgrid polarized cameras, led to the simplification of the polarimetric setup from a 4 x 4 MM to a reduced 3 x 4 MM. To facilitate image acquisition using this camera, we have devised a novel algorithm capable of decomposing the Mueller Matrix from its reduced (3 x 4) form. The algorithm was compared and shown to provide similar results to two established decomposition methods. Finally, we have used this approach to obtain depolarization and azimuthal angle values of biological tissue including *ex vivo* samples and *in vivo* cervix. This work paves the way to non-invasive studies of cervical structure *in vivo*.

TABLE OF CONTENTS

CHAPTER	PAGE
CHAPTER 1: Cervical imaging in the low resource setting: a review.....	1
1.1 Introduction.....	1
1.1.1 Anatomy of the cervix.....	2
1.1.2 Disease progression.....	3
1.1.3 Cervical testing and treatment.....	4
1.1.3.1 HPV DNA testing, cytology, colposcopy, and biopsy.....	5
1.1.3.2 Visual inspection.....	6
1.1.3.3 Treatments.....	7
1.1.4 HPV vaccines.....	8
1.2 Limits of cervical screening in low resource setting.....	8
1.3 Cervical imaging targeted for neoplastic detection.....	9
1.3.1 Callascope.....	9
1.3.1.1 Device.....	9
1.3.1.2 Clinical testing.....	10
1.3.2 High resolution microendoscope (HRME).....	12
1.3.2.1 Device.....	12
1.3.2.2 Clinical testing.....	13
1.3.3 Snapshot Mueller matrix polarimeter.....	14
1.3.3.1 Device.....	14
1.3.3.2 Clinical testing.....	15
1.3.4 Enhanced Visual Assessment (EVA) System.....	15
1.3.4.1 Device.....	15
1.3.4.2 Clinical testing.....	17
1.3.5 Gynocular.....	17
1.3.5.1 Device.....	17
1.3.5.2 Clinical testing.....	18
1.3.6 Images taken by the devices.....	21
1.4 Conclusions.....	24
1.5 Dissertation outline.....	25
CHAPTER 2: Polarization concepts and cervical anatomy.....	27
2.1 Polarization.....	27
2.1.1 Stokes vector.....	28
2.1.2 Mueller matrix polarimetry.....	30
2.2 Mueller matrix decomposition.....	31
2.2.1 Diattenuation.....	32
2.2.2 Depolarization.....	34
2.2.3 Retardance.....	35
2.2.4 Mueller matrix and cervical tissue.....	36
CHAPTER 3: Design and implementation of a portable colposcope Mueller matrix polarimeter.....	38

3.1 Introduction.....	38
3.2 Methods.....	41
3.3.1 Image processing.....	45
3.3.1.1 Fourier reconstruction.....	45
3.3.1.2 Sliding reconstruction.....	49
3.3.2 Anisotropic and ex vivo biological samples.....	51
3.3.3 Clinical deployment.....	52
3.3 Results.....	53
3.4 Discussion.....	60
3.5 Conclusion.....	61
CHAPTER 4: Introduction of a 3×4 Mueller matrix decomposition method.....	63
4.1 Introduction.....	63
4.2 Methods.....	65
4.2.1 Validation.....	68
4.3 Results and discussion.....	69
4.4 Conclusion.....	79
CHAPTER 5: Testing the 3×4 Mueller matrix decomposition in biological tissue.....	81
5.1 Introduction.....	81
5.2 Methods.....	83
5.2.1 Specifications.....	83
5.2.2 Image analysis.....	85
5.2.3 Ex vivo testing.....	86
5.2.4 In vivo testing.....	86
5.3 Results.....	87
5.3.1 Ex vivo chicken tendon.....	87
5.3.2 Paraffin embedded porcine cervix.....	88
5.3.3 In vivo human cervix.....	89
5.3.3.1 Insertion: patient feedback.....	89
5.3.4 Clinical deployment.....	91
5.4 Conclusions and future work.....	92
CHAPTER 6: Conclusions.....	94
References.....	98
VITA.....	112

LIST OF TABLES

TABLE	PAGE
Table 1.1 Callascope cervical quadrant visualization.....	11
Table 1.2 Summary of the portable devices introduced for cervical imaging.....	20
Table 2.1 Stokes vector for degenerate cases of the polarization ellipse.....	29
Table 3.1 Patient age and clinical evaluation performed by a physician.....	57
Table 4.1 The decomposition parameters (Δ , δ , θ) for the matrix M (Equation 4.10a). (First column) values from Ghosh et al. ¹ , (second column) values from the LC decomposition, (third column) D decomposition and (fourth column) decomposition of the reduced 3 x 4 matrix.....	71

LIST OF FIGURES

FIGURE	PAGE
Figure 1.1 Anatomy of the uterine cervix highlighting the epithelium found on the surface, as well as the transformation zone and squamocolumnar junction (SCJ).....	3
Figure 1.2 Schematic of the Callascope device, designed for self-insertion and aiming of the uterine cervix. [Reproduced from Asiedu et al. 2020 ²].....	10
Figure 1.3 Schematic of HRME device used for fluorescence measurement of the cervical epithelium. [Reproduced from Pierce et al. 2011 ³].....	13
Figure 1.4 The snapshot Mueller matrix polarimeter used for polarization imaging of the uterine cervix is shown. [Reproduced from Gonzalez et al. 2020 ⁴].....	15
Figure 1.5 The EVA system, as well as the visualization of the uterine cervix through the speculum is shown. [Reproduced from Marta et al. 2016 ⁵].....	16
Figure 1.6 The portable colposcope, Gynocular, from Gynius Plus AB. [Reproduced from Gynius Plus AB website].....	18
Figure 1.7 Sample images taken with the Callascope while self-imaging. [Reproduced from Asiedu et al. 2020 ²].....	22
Figure 1.8 Representative cervix images of (A,D) the whole cervix, (B,E) the nuclei as seen by the HRME and the (C,F) histopathology. [Reproduced from Quinn et al. 2012 ⁶].....	22
Figure 1.9 Cervical images taken by the snapshot Mueller matrix polarimeter, showing the (a-c) raw images and polarization information of (d-f) depolarization and (g-i) retardance. [Reproduced from Gonzalez et al. 2020 ⁴].....	23
Figure 1.10 Example of images taken with the EVA system showing different quality of images, ranging from very poor to excellent. [Reproduced from Mayoore et al. 2018 ⁷].....	24
Figure 1.11 Images taken with the Gynocular, showing a normal cervix (left) and a cervix with high grade lesions (right). [Reproduced from Kallner et al. 2015 ⁸].....	24
Figure 2.1 Light propagation through a diattenuator, where P_y and P_x are the attenuation coefficients.....	33
Figure 2.2 Example of depolarizing material due to multiple scattering.....	34
Figure 2.3 Illustration of light propagating through a retarder, where phase shifts $-\phi/2$ and $\phi/2$ can be seen in the y and x axis, respectively.....	36

Figure 3.1. Optical layout of the PSA portion of the system.....	41
Figure 3.2. MTF of the Savart Polarimeter.....	42
Figure 3.3. The snapshot Mueller matrix polarimeter.....	43
Figure 3.4. Polarization state generator. H is a horizontally aligned polarizer (with respect to the reference frame, optical bench), V is a vertically aligned polarizer, P is a 45 degrees aligned polarizer, and R is a circular polarizer.....	44
Figure 3.5. An input Stokes vector was created with a USAF target (top figure). The status of polarization corresponds to a linear orientation of 22.5 degrees for the background and 0 degrees for the lines. The bottom figure shows the Stokes vector after reconstruction. There are still visible artifacts (traces from the target) where the Fourier reconstruction failed.....	46
Figure 3.6. (a) Interferogram associated with the USAF test target as seen by a camera sensor, (b) Fourier transform of the interferogram of the USAF target, featuring the peaks (along with the full frequency profile) where the Stokes vectors are spatially encoded within the interferogram.....	47
Figure 3.7. Stokes vector of a USAF target reconstructed with the sliding reconstruction method (a) showing traces of the (b) largest and (c) smallest blocks of resolution dashes. As can be observed from the changes from the raw signal to the reconstructed signal, strong discontinuities create artifacts in the Stokes images.....	51
Figure 3.8. Mueller Matrix of air. The portable device was tested in transmission to understand the error of the polarimetric response. Although some structural artifacts are present (small white lines in the matrix), the expected values of ones in main diagonal elements are present.....	54
Figure 3.9. Extruded silicone sample recovered orientation. The silicone sample was placed at a 22 degrees shift (marked in the red line) from the frame of reference. (a) Raw image (gray scale) with the recovered mean angle of a region of interest (colormap), (b) circular histogram of the recovered angles.....	55
Figure 3.10. Ex vivo paraffin embedded porcine cervix. (a) Raw image highlighting region of interest, (b) Mueller matrix decomposed depolarization, (c) Mueller matrix decomposed retardance (d) distribution of depolarization and (e) distribution of retardance angle.....	56
Figure 3.11. In vivo healthy human cervixes with negative clinical evaluations (a-c) raw images with the highlighted region of interest, (d-f) the depolarization and (g-i) the retardance portrayed as a binary high (H, red)/low (L, green) with zero background (B, white) using a threshold of 25 degrees.....	57
Figure 3.12. The depolarization (top) and retardance (bottom) of the 16 healthy subjects are summarized. The healthy cervixes show a pattern of high depolarization, with the	

lowest value (patient 1) being the polyp. The retardance shows a trend of high values as well, with only two cervices having a median value below the 25 degree threshold.....	59
Figure 4.1. Experimental setup consisting of a light source with collimating lens, a PSG consisting of a polarizer on a rotational stage, a quarter-wave plate (QWP1), and PSA utilizing the polarized camera with lens and a quarter wave plate (QWP) that is inserted only when measuring the 4 x 4 Mueller Matrix.....	68
Figure 4.2. Error analysis of the minimization algorithm used for the decomposition of a reduced 3 x 4 Mueller matrix. The left figure shows a slice of error values for all θ and δ with d_1 fixed at 0.7. The right figure shows the error contour plots in selected volume sections.....	70
Figure 4.3. Comparison between the decomposition of a reduced 3 x 4 Mueller matrix (3 x 4), LC and D decompositions of 4 x 4 Mueller matrix of the QWPs oriented at (a,d) -20 degrees, (b,e) -30 degrees and (c,f) -60 degrees with respect to the polarization axis of the incident beam. The red lines delineate the median value of the data set.....	75
Figure 4.4. Reduced 3 x 4 Mueller matrix of a silicone sample oriented at -70 degrees, showing the striation direction. The weakly depolarizing nature of the sample is confirmed by the dominance of the diagonal values that are close to one.....	75
Figure 4.5. The images of (a,d,g) the depolarization, (b,e,h) the retardance and (c,f,i) the angle of orientation calculated from Mueller matrix of a silicone phantom oriented at -70 degrees using the three decomposition methods: (first row) 3 x 4 decomposition, (second row) LC decomposition, and (third row) D decomposition. The white box indicates a region of interest at which the sample is assumed to be homogeneous (for comparison purposes).....	76
Figure 4.6. Comparison between the reduced 3 x 4 Mueller matrix decomposition, LC and D decompositions of the complete 4 x 4 Muller matrix of silicone phantom oriented at (a,d,g) 80 degrees, (b,e,h) 70 degrees and (c,f,i) 60 degrees with respect to the reference plan of the incident beam. The red lines delineate the median values within the ROI.....	76
Figure 4.7. The images of the depolarization, the retardance and the orientation angle of human skin model section mounted on the glass slide with focus on the dermis. The parameters calculated with three different decompositions: 3 x 4, LC and D are shown from top to bottom, respectively. The saturated and background pixels have been rendered in white. The white box indicates a region of interest in the dermis at which the sample is assumed to be homogeneous.....	78
Figure 4.8. Comparison of the results of three decompositions of the Mueller matrix of human skin model section, where we can observe the similitude of the 3 x 4	

decomposition with the 4 x 4 LC decomposition as well as the D. Red lines indicate median value of the data set.....	78
Figure 5.1 (Top left) Design assembly and (top right) exploded view. (Bottom) Exploded section in 2D along with description of full assembly itemized 1-8. [Reproduced from Boonya-ananta et al. ⁹].....	84
Figure 5.2 Gynecological training system used to evaluate image quality of the PPRIM.....	85
Figure 5.3 Chicken tendon sample showing (a) the intensity image, M11, (b) the depolarization and (c) the orientation, as shown by the azimuth angle. The black bars indicate the preferred alignment of the tissue within a 10 pixel range.....	88
Figure 5.4 Porcine tendon embedded in paraffin sample one showing (a) the intensity image, M11, (b) the depolarization and (c) the orientation, as shown by the azimuth angle. The black bars indicate the preferred alignment of the tissue within a 10 pixel range.....	89
Figure 5.5 Porcine tendon embedded in paraffin sample two showing (a) the intensity image, M11, (b) the depolarization and (c) the orientation, as shown by the azimuth angle. The black bars indicate the preferred alignment of the tissue within a 10 pixel range.....	89
Figure 5.6 PPRIM device showing inserter and imager. The left image shows the inserter with a condom used to aid slide it into position. The dashed line shows where the condom is cut to not interfere with the image quality. The right image shows the device fully assembled including the inserter and imager.....	90
Figure 5.7 <i>In vivo</i> human cervix sample showing (a) the intensity image, M11, (b) the depolarization and (c) the orientation, as shown by the azimuth angle. The black bars indicate the preferred alignment of the tissue within a 10 pixel range.....	92
Figure 5.8 <i>In vivo</i> human cervix sample two showing (a) the intensity image, M11, (b) the depolarization and (c) the orientation, as shown by the azimuth angle. The black bars indicate the preferred alignment of the tissue within a 10 pixel range. The os can be seen as the black semi-circle in the top right corner.....	92

ABBREVIATIONS AND ACRONYMS

MMP	Mueller matrix polarimetry
MMI	Mueller matrix imaging
ECM	Extracellular matrix
HPV	Human papillomavirus
PPRIM	Portable Preterm Imaging system
HRME	High resolution microendoscope
EVA	Enhanced visual assessment
FOV	Field of view
USAF	United States Air Force
PSG	polarization state generator
PSA	polarization state analyzer
CMOS	complementary metal-oxide-semiconductor

CHAPTER 1 : Cervical imaging in the low resource setting: a review

1.1. Introduction

Cervical cancer is the fourth most common cancer in women, with more than half a million women diagnosed each year due to persistent human papillomavirus (HPV) infection and a mortality of 311,000 women¹⁰. According to the World Cancer Research Fund, developing countries have 84% of the global burden of the disease and 80% of the mortality due to a lack of effective screening programs¹¹. This causes cervical cancer to be an example of global health inequity, since the slow-progressing disease provides time for detection and treatment of pre-cancerous lesions. Many women in low and middle income countries (LMICs) seek clinical care once there are persistent cancer symptoms, whereas cervical cancer screening programs in high income countries have helped reduce the mortality significantly¹². Several screening techniques have been developed and implemented to aid in low resource setting cervical screening.

Literature reviews describing the optical modalities available for cervical cancer detection have been introduced by Novikova¹³, Hill et al.¹⁴ and Olpin et al.¹⁵ and others^{16,17} where they have covered modalities, such as ultrasound, optical coherence tomography and spectroscopy (among others), as well as their clinical outcomes. Softland et al. looked at two handheld colposcopes, the Gynocular and the Enhanced Visual Assessment (EVA) System by Mobile ODT, and compared their capabilities for the use in female genital schistosomiasis¹⁸.

This manuscript focuses on reviewing existing cervical imaging devices for deployment in low resource settings that are being or can potentially be implemented for cervical cancer screening and diagnosis.

1.1.1. Anatomy of the cervix

The cervix is a cylindrical structure that connects the vaginal canal (ectocervix) to the uterus (endocervix). It is 2-3 cm long, composed mainly of epithelium and stroma. There are two main types of epithelia present in the cervix: columnar and stratified squamous. The columnar epithelium is the lining found in the endocervix and secretes mucus. The stratified squamous epithelium is found in the ectocervix and is a continuation of the vaginal epithelium. The location where these two epithelia meet is called the squamocolumnar junction (SCJ). The location of the SCJ varies depending on continuous cervical remodeling, the main factors being age and hormones (e.g., the SCJ is found in the external os in younger women)^{19,20}. The cervix contains a thick layer of stroma under both types of epithelia, which is mainly composed of muscular, elastic and fibrous tissues. The fibrous stroma occupies three areas with unique orientation surrounding the cervical canal. The inner canal and outer cervix is composed of longitudinally aligned collagen and in between can be found circumferentially aligned collagen²¹. Figure 1.1 illustrates an anatomical representation of the cervix.

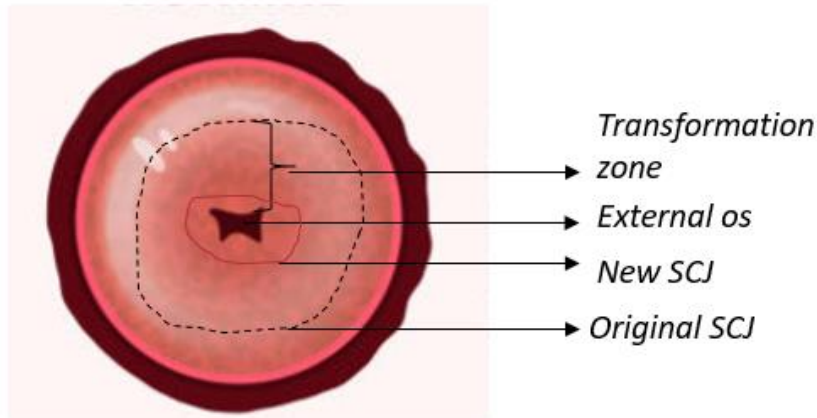


Figure 1.1 Anatomy of the uterine cervix highlighting the epithelium found on the surface, as well as the transformation zone and squamocolumnar junction (SCJ)

HPV infection is the principal cause of cervical cancer. Types 16 and 18 are responsible for 71% of cases, however, when including HPV types 4, 11, 16, 18, 31, 33, 45, 52 and 58, the percentage of cervical cancer cases due to HPV rises to 90%. HPV is a family of DNA viruses (approximately 15 that can infect the genital tract) that target basal epithelial cells and can cause benign and malignant lesions ^{22,23}. Common types of cancers include squamous cell, adenocarcinomas, sarcomas and small cell neuroendocrine tumors. Most infections are cleared by the immune system, if not, the virus proceeds to attack the cells in the cervical SCJ ^{13,23,24}. A persistent infection can spread and break through the basal membrane to become an invasive cancer¹³.

1.1.2. Disease progression

During disease progression, three types of neoplastic states affect the epithelium. Cervical intraepithelial neoplasia (CIN) of 1st grade or CIN 1, affects one-third of the epithelium and is considered mild and likely caused by a transient HPV infection, which should clear

naturally. CIN 2, which affects two-thirds of the epithelium is a moderate case and is a combination of self-clearing and pre-cancerous lesion. CIN 3 is considered severe as it affects the whole epithelium, it is a pre-cancer state since the lesions are unlikely to clear up naturally. Using the Bethesda System (classification system used for cytological diagnosis and treatment decisions), CIN 1 is a low-grade squamous intraepithelial lesion (LSIL) and CIN 2 and 3 are high-grade squamous intraepithelial lesions (HSIL). Invasive cervical cancer is a slow progressing disease, taking in generally more than 10 years to fully develop from infection.

Cervical neoplasia is related to changes in both the stroma and epithelial cells^{25,26,27,28}. Stromal changes stimulate and precede neoplastic progression. Moreover, carcinogenesis is the result of a defective communication between the epithelium and the stroma^{26,28}. The extracellular matrix (ECM) can regulate growth, death, gene expression, migration, among other processes, all of which regulate physiologic processes such as angiogenesis, tissue morphogenesis, embryonic development and pathological processes. Furthermore, stroma and tumor cells can exchange growth factors to activate neighboring ECM and aid the expansion of neoplastic cells²⁵. The deregulation between the stroma and the epithelium communication promotes carcinogenesis^{26,27}. Neoplastic progression results in changes to the stroma, and therefore the collagen matrix, which leads to changes in stromal scattering, and can be used for optical contrast in diagnostic measurement of neoplastic tissues²⁸.

1.1.3. Cervical testing and treatment

The standard procedure for cervical cancer diagnosis in the United States includes liquid-based cytology (Pap test) and DNA testing for high-risk HPV. If abnormal results are

obtained, then colposcopy, biopsy and histological confirmation are performed. This procedure, however, requires a high level of quality standards such as trained personnel, medical coverage and follow-up visits. Therefore, the World Health Organization (WHO) recommends a screen and treat approach, where the primary screening test should be HPV DNA detection every five to ten years after the age of 30²⁹. Due to previous recommendations, current screening practices include HPV testing, visual inspection with acetic acid (VIA) and cytology, all followed by treatment. Another commonly used screening option is visual inspection with Lugol's iodine (VILI), although not explicitly recommended by the WHO. Some of the aforementioned practices cannot be used in the general population, for example, VIA testing is not appropriate for women older than 50 years of age since the transformation zone (where the lesions normally start) moves into the endocervical canal after menopause. The choice of screening techniques depends highly on the resources in the settings, although the latest recommendations by WHO highly recommends the switch from previously mentioned methods to HPV DNA screening due to the objectivity of the test and lack of need for interpretation ²⁹.

1.1.3.1. HPV DNA testing, cytology, colposcopy, and biopsy

Cervical cancer screening in the United States consists of multiple stages. HPV DNA co-testing along with cytology (or Pap smear) are the first steps for every cervical cancer diagnosis, wherein a speculum is inserted into the vaginal canal in order to collect cells from the cervix. The cells are analyzed for abnormality and apparent changes. Cytology results are difficult to score as it has been shown there is low interobserver agreement. Stoler et al. found that there was only 47.1% agreement in interpretation of HSIL for cytology results when comparing original diagnosis with a quality control group³⁰. HPV

DNA testing determines the presence of high-risk HPV with a specificity and accuracy of 55.6% and 75.8%, respectively, and a positive predictive value of 84.8%³¹.

When abnormal cells are found (i.e., positive Pap smear), a second step in the cervical screening is colposcopy. Colposcopy is a visual inspection conducted by trained physicians with a colposcope (clinical microscope with 3-15 times magnification) that allows for a closer look at the uterine cervix. The accuracy of this procedure is highly dependent on the training level and experience of clinicians. The diagnostic value of the technique has been reported to have high sensitivity (85%) but low specificity (69%), meaning the abnormal location can be found but the severity of the lesion is often inaccurate^{32,33,34,35}. Furthermore, the interobserver variability for colposcopic data has a kappa value of 0.40³⁶. As part of the colposcopy, a biopsy is normally performed where a small portion of the cervix is sampled with a punch biopsy. Similar to cytology, biopsies have low interobserver agreement. A study conducted on 2237 cervical histologies showed that the agreement between the original pathologist and the quality control group overlapped only 42.7% of the times for CIN1 cases³⁰.

1.1.3.2. Visual inspection

VIA consists of applying a 3-5% acetic acid solution to the ectocervix. This application will turn abnormal cells in the epithelium to an opaque white color (referred to acetowhite) and the tissue is considered VIA positive. These acetowhite lesions are due to the coagulation of proteins in the cells with acetic acid since neoplastic tissue will have a higher protein content than normal tissue. The positive predictive value of VIA is 16.7% and the negative predictive value of 99%. The specificity and sensitivity are 79.4% and 71.8%,

respectively^{37,38}. These results translate to a high number of false positives leading to overdiagnosis and overtreatment.

Another visual inspection technique, VILI, consists of the application of Lugol's iodine to the cervical epithelium. This solution reacts with glycogen, which is present in normal healthy tissue, and turns black upon exposure. In the presence of neoplastic tissue, the glycogen is reduced or absent and the solution turns the epithelium yellow. The positive predictive value of VILI is 16.8% and the negative predictive value of 99.7%, resulting in a large number of false positives. The specificity and sensitivity of VILI is 86% and 88%, respectively^{38,39}.

Visual inspection for cervical screening suffers from low reproducibility and results in variation depending on the subjectivity of the interpretation of the results⁴⁰. It has also been shown that age, parity, menopause and HPV presence can influence the outcome of visual inspection tests, as well as the level of training of the healthcare providers⁴¹. However, the low cost and real time results from visual inspection tests make it ideal for the low resource settings, and the screen and treat approach^{39,40}, especially in areas of high cervical cancer incidence and low medical resources⁴². In order to overcome the current screening issues using VIA and VILI, better training of healthcare personnel is needed. Moreover, Raifu et al. recommends specifically better training of personnel on definition and interpretation of acetowhite lesions of the cervical epithelium in these settings⁴¹.

1.1.3.3. Treatments

The treatments recommended for cervical neoplasia is directed at removing or destroying the transformation zone and/or abnormal areas found in the cervix. Two main treatment

routes include ablation and excision. Using ablative treatment, the abnormal tissue is destroyed by heating through thermal coagulation or freezing it via cryotherapy. The excisional route removes tissue by large loop excision of the transformation zone (LLETZ) or by cold knife cone (CKC), also known as conization of the cervix²⁹.

1.1.4. HPV vaccines

There have been three HPV vaccines available since 2006, although only one is currently used in the United States. Gardasil 9 is a 9-valent vaccine that targets HPV types 6, 11, 16, 18, 31, 33, 45, 52 and 58. The vaccine has an efficacy close 100% for young adolescents 9-15 years old⁴³. The vaccine targets infections in other anatomical areas other than the cervix (e.g., vulva, penis, anus). Although HPV vaccination has reduced the number of infections in women since its introduction⁴⁴, it does not cover all 15 high-risk HPV types. Moreover, it is expensive and difficult to implement in developing countries, leaving screening and treatment of precancerous lesions⁴⁵ as the main preventive methods.

The slow progression of cervical cancer, the anatomic accessibility and the possible treatment of precancerous lesions, make early screening an effective management^{13,46}. Due to the high costs of traditional cervical screening procedures, several devices have been developed for use in the low resource setting to increase access to cervical testing. This review paper introduces current cervical imaging devices designed for deployment in the low resource setting, their specifications and clinical outcome.

1.2. Limits of cervical screening in low resource setting

Limitations on cervical screening in low resource settings include an array of reasons. Common issues include the lack of regular participation in screening from patients due to

social and cultural taboos, health literacy, inadequate sampling and management of smears by clinicians, interpretation errors from pathologists and lack of screening programs that can reach target populations⁴⁷. Operational limitations to existing screening tests, such as cytology, VIA/VILI and HPV DNA-based tests, include lack of trained manpower, timeliness of test result availability, possibility of overtreatment, the need for laboratory setup, among others^{48,49}. Moreover, screening with colposcopes are difficult to implement, since they are costly and electricity dependent, as well as need high maintenance⁵⁰. They are also voluminous and heavy, making it difficult to transport outside a clinical setting.

It has been previously noted by the World Health Organization that even a once in a lifetime Pap smear screening can significantly reduce the incidence and mortality of cervical cancer⁴⁸. The introduction of portable, low-cost devices aim to close this very gap on screening limitations.

1.3. Cervical imaging targeted for neoplastic detection

1.3.1. Callascope

1.3.1.1. Device

The Callascope^{2,51,52,53} is a speculum free device used for capturing images of the cervix. The Callascope was developed at the Department of Biomedical Engineering at Duke University, North Carolina. The Callascope is designed to create a speculum-free imaging system composed of an introducer and a slender camera. The introducer is a Calla Lily² shaped silicone hollow tube which can be inserted into the vagina (Figure 1.2). The introducer is approximately 30 mm at the larger proximal end and 12 mm at the distal end⁵¹. The asymmetric tip is designed to allow rotation of the introducer to tilt the cervix into a

favorable viewing position. The light source is composed of a ring illuminator with four white LEDs. The camera and housing can be inserted into the introducer to be positioned for imaging the cervix. The camera body is a slim 9 mm diameter tube with length approximately 120 mm. The camera is a 2 to 5 Megapixel CMOS^{2,51} sensor with a lens. The camera is fitted with a hydrophobic window at the tip and is positioned into the center of the ring illuminator. When inserted into the introducer, the camera is positioned to a working distance of 25 to 30 mm from the cervix. The Callascope has a field of view of 35 mm. At a working distance of 30 mm and 4x magnification the smallest resolved feature on a USAF 1951 resolution target was 99.2 μm .

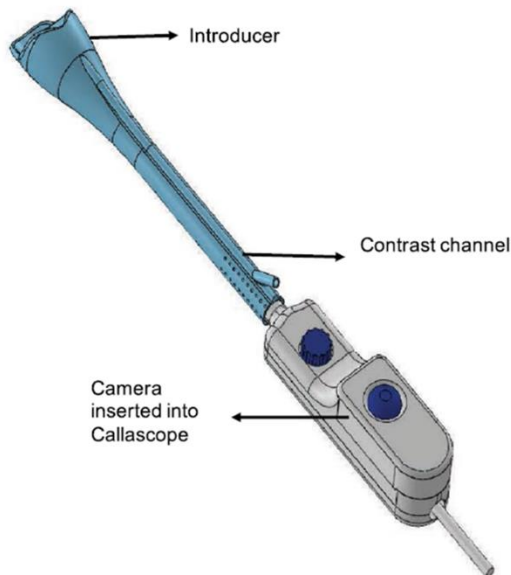


Figure 1.2 Schematic of the Callascope device, designed for self-insertion and aiming of the uterine cervix. [Reproduced from Asiedu et al. 2020²]

1.3.1.2. Clinical testing

Clinic testing of the device has been performed in both the United States and Ghana looking at two different environments of the Callascope: clinician usage and self-conducted

imaging of the cervix². Participant eligibility included healthy females of 18 years or older. Numbers of participants in Ghana comprised of 25 for clinician testing and 10 for individual usage. In the U.S., 28 participants for clinicians and 12 for self-imaging. Participants underwent a pre-exam survey to document demographical information and perceptions on the use of a speculum, Callascope, clinician vs. self-examination. Post-examination survey was conducted using a modified Universal Pain Assessment tool alongside a written description. Image quality was assessed using one point for visualization of the os and one for each of the four cervical quadrants.

Overall assessment shows higher preference to the Callascope vs. a standard speculum of above 75% in both testing sites (CITE SR 2020). On studies performed by clinicians, the Callascope enabled visualization of the os for 78.6% in U.S. and 80% in Ghana participants. The speculum-based imaging shows visualization of the os for 96% in U.S. and 100% in Ghana. Table 1.1² provides the assessment of cervical quadrant visualization for clinician usage. In for self-imaging, over 60% of participants in both sites found the Callascope easy to insert and use. No patients indicated extreme discomfort and over 70% of participants indicated no or slight discomfort in the post-examination survey.

Table 1.1 Callascope cervical quadrant visualization

View of at least # Cervical Quadrants	Callascope	
	U.S.	Ghana
	[%]	
2	89	84
3	72	71
4	50	44

1.3.2. High resolution microendoscope (HRME)

1.3.2.1. Device

The high resolution microendoscope (HRME) is a fluorescence optical imaging system that has been employed for cervical cancer screening. The system light source consists of a 455 nm LED, which is coupled to a fiber bundle. This wavelength is used to excite proflavin, an FDA approved fluorescent DNA label used to dye nuclei from the cytoplasm of cells. A topical solution of proflavin is needed to be used along the HRME, where the fluorescent emission (510 nm) is captured with a CCD camera (also coupled to the fiber bundle) after passing through a 475 nm dichroic mirror. The probe, consisting of the fiber bundle, requires insertion through a speculum. To be in focus, probe contact with the cervical epithelium is required. The HRME can provide real time morphology and epithelial architecture with a field of view of 720 μm and a lateral resolution of 4 μm ^{3,6}. The device is portable and weighs 2.3 kg—although a new iteration has reduced the weight to 0.91 kg⁵⁴. The HRME costs approximately \$2450 mainly due to the computer tablet, although costs have been reduced with the introduction of a Raspberry Pi computer⁵⁵. The device can be seen pictured in Figure 1.3.

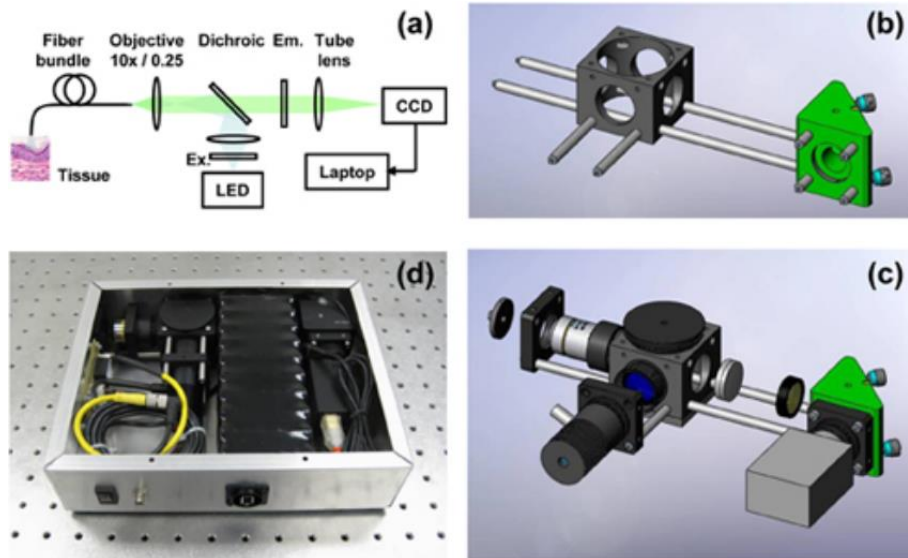


Figure 1.3 Schematic of HRME device used for fluorescence measurement of the cervical epithelium. [Reproduced from Pierce et al. 2011³]

1.3.2.2. Clinical testing

The HRME has been deployed in clinical settings such as Botswana, Brazil, the United States (Texas) and El Salvador^{6,55,56,57,58,59}. A human study in Botswana was performed by first conducting a routine colposcopic examination. Then, a solution of proflavine hemisulfate was applied and the HRME was inserted through a speculum to meet the cervix. Images were gathered for 26 patients from 52 sites, low quality images were discarded. Calculating the average nuclear to cytoplasmic area ratio, a receiver operator characteristic (ROC) determined a specificity of 86% and a sensitivity of 87% high grade neoplastic lesions (CIN2+)⁶. Another study in Brazil deployed the device in a colposcopy clinic in Barretos Cancer Hospital and a mobile diagnostic van that traveled to different communities. The portable device was then used after routine colposcopy examination and application with proflavine solution. The study determined an average specificity and

sensitivity of 48% and 92%, respectively, for identification of CIN2+ as compared with histopathology⁵⁶. The HRME system has also been used in oral and esophageal cancer diagnosis^{60,61,62,63}.

1.3.3. Snapshot Mueller matrix polarimeter

1.3.3.1. Device

The snapshot Mueller matrix polarimeter is a portable optical imager introduced in 2020. The device is based on Mueller matrix polarimetric imaging and uses a ring illuminator to generate four different polarization states at 633 nm for the polarization state generator (PSG). The snapshot approach is achieved by two Savart plates to generate four different rays with unique polarization information that are analyzed by a 45 degrees polarizer—forming the polarization state analyzer (PSA)—and are detected on a CMOS camera. The polarimetric approach can provide quantitative information on the cervix using Mueller matrix decomposition, since healthy (normal) and unhealthy cervixes behave differently to incident polarized light (especially the parameters of depolarization and retardance). The field of view of the device is 30 mm, allowing a full view of the cervix with a single snapshot. The device is noninvasive although a speculum is needed to visualize the cervix. The cost of the device is approximately \$2000⁴. A picture of the device can be seen in Figure 1.4.

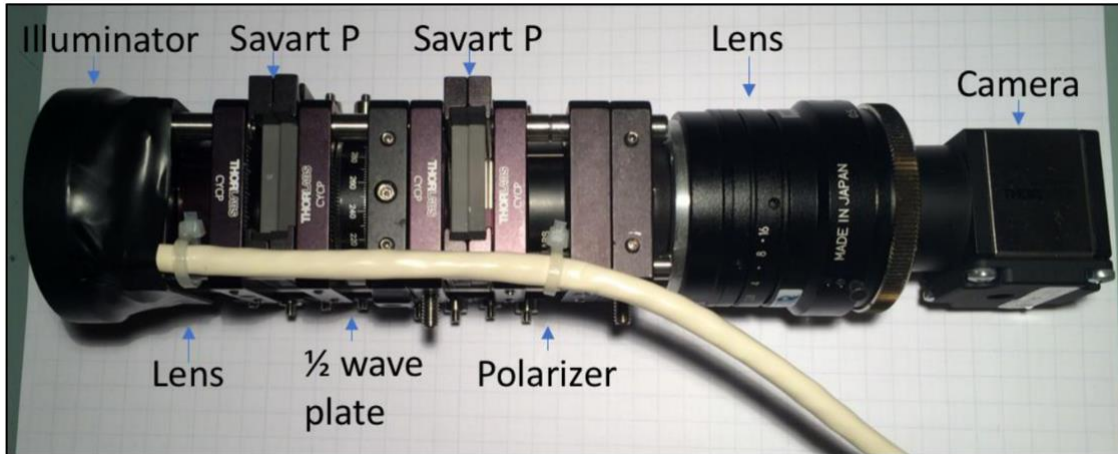


Figure 1.4 The snapshot Mueller matrix polarimeter used for polarization imaging of the uterine cervix is shown. [Reproduced from Gonzalez et al. 2020⁴]

1.3.3.2. Clinical testing

The device was clinically deployed in the Public Health Research Institute of India (PHRII) in Mysore, India. Twenty-two patients were recruited although due to image quality six patients were excluded for the reported results. The patients underwent cervical inspection as routine examination and then the snapshot polarimeter was used to image the cervix. The results agreed with polarimetric imaging of healthy cervixes, where there are high depolarization values for all patients. There was an exception for one patient that was diagnosed with a polyp, which showed lower depolarization values (as expected)^{4,64}.

1.3.4. Enhanced Visual Assessment (EVA) System

1.3.4.1. Device

The Enhanced Visual Assessment (EVA) System developed by MobileODT (Tel Aviv, Israel) is a portable colposcope for enhanced analysis using VIA. The system utilizes a speculum to image the cervix and can be used to augment the results from VIA by

supplying the lighting and magnification needed as well as aiding the logging of images and information. The EVA system is portable, weighing 605 grams, with a light source consisting of a white 3 W (3.6 V) LED. The battery powered system can last up to ten hours of constant use. The system is equipped with a cellphone, with an optical zoom capability of 4x and a digital zoom capability of 16x. The on-board software provides real time analysis capability and tracking for patient follow-up⁶⁵. The EVA system utilizes an application to control the smartphone and a cloud-based image portal to store and view images⁷. The cost of the device is approximately \$8200, including the provided annual service and technical support. The device can be seen in Figure 1.5.



Figure 1.5 The EVA system, as well as the visualization of the uterine cervix through the speculum is shown. [Reproduced from Marta et al. 2016⁵]

1.3.4.2. Clinical testing

Clinical testing of the EVA system was conducted at different sites. The device was used as primary screening co-testing along with cytology by Fronteras Unidas Pro-Salud outreach program, which provided an early guide of suspicious areas in patients⁵. Another clinical study conducted in a hospital-based setting and an urban screening camp in Mumbai, India showed an agreement of EVA and cytology in 157 cases out of the 471 patients. Most disagreement in prognosis were due to misclassification of cervicitis in patients. It must be noted that EVA compared well against naked eye visualization in the screening camp, as well as collected information (such as age and socioeconomic status) that is often difficult to gather⁶⁶. The device has also been included in protocols to screen HIV-infected women for cervical cancer in Rwanda.

Image quality was tested for images taken using the EVA system. Using a random subset of images found in the MobileODT portal, it was found that 73% of the images were of poor quality and could not be used further. To address this issue, an ongoing effort in determining the image quality in real time is underway using machine learning methods⁷.

1.3.5. Gynocular

1.3.5.1. Device

The Gynocular is a small monocular colposcope developed by Gynius Plus AB, a company based in Stockholm, Sweden. The device functionality is like the colposcope, but has the advantage of being pocket-size and a total weight of 480 g. A self-holding speculum is used in conjunction to the device to access the cervix. The Gynocular offers an optical magnification of 5x, 8x and 12x with a field of view ranging from 20 to 40 mm (depending

on the magnification). The light source employs a 3 W/3.6V warm white LED, a green filter (530 nm) can be added to the imaging protocol. The battery on board is able to withstand at least two hours of use. The device is portable and can be used as a handheld device, as well as, mounted on a tripod for increased stability. A cellphone can also be coupled with the portable device to take images. The cost of the portable device is approximately \$3000. A picture of the Gynocular can be seen in Figure 1.6.



Figure 1.6 The portable colposcope, Gynocular, from Gynius Plus AB. [Reproduced from Gynius Plus AB website]

1.3.5.2. Clinical testing

The Gynocular has been compared to a standard colposcope in multiple clinical studies in Uganda, India, Bangladesh, and Sweden.^{8,67,68,69,70,71,72} One study tested VIA positive women in a clinical study in a hospital setting in Uganda. Sixty-seven women were included in this study and visual scores given to the state of the cervix were 70.1% in agreement for both modalities, where 47 out of 67 measurements were in agreement⁶⁹. Another clinical study performed in a colposcopy clinic in Bangladesh determined Moreover, in this study the Gynocular had a sensitivity of 83.3% and a specificity of 23.6%

with a positive predictive value of 88.6% and a negative predictive value of 16.6%⁶⁸. There was no significant difference between the Gynocular and the colposcope for identifying CIN2+ lesions in all clinical trials performed^{8,68,69,70,72}.

A summary table of the modalities and their specifications can be seen in Table 1.2.

Table 1.2 Summary of the portable devices introduced for cervical imaging.

Device	Company	FOV	Weight	Power	Cost	Portable?	Magnification	Illumination	Can it be mounted?	Need speculum?	Software included?
<i>Callascope</i>	Duke University	30 mm	-	PC		Yes	4x	White ring LED	No	No	Yes
<i>HRME</i>	Rice University	720 microns	2.3 kg	PC	2450	Yes	10x	455 nm LED	No	Yes	Yes
<i>snapshot Mueller matrix polarimeter</i>	FIU	30 mm	-	PC	2000	Yes	none	(4) 633 nm LEDs	Yes	Yes	Yes
<i>EVA</i>	Mobile ODT		605 g	Battery	8200	Yes	4x,16x	3 W (3.6 V) LED	Yes	Yes	Yes
<i>Gynocular</i>	Gynius	20-40 mm	480 g	Battery	3000	Yes	5x,8x,12x	3 W (3.6 V) LED	Yes	Yes	Yes

1.3.6. Images taken by the devices

Sample images taken from each device discussed are shown below. Images captured by the participants (self-imaging) of the cervix using the Callascope are shown in Figure 1.7. These images represent a subset of cervix data taken from 22 healthy volunteers to test the self-imaging abilities of the device.

Figure 1.8 shows images from Quinn et al. during a clinical study in Princess Marina Hospital in Botswana. The images on the left (A and D) are taken with a colposcope, where the white arrow signifies the area imaged with the HRME (B and E). The third row (C and F) is the histologic confirmation of the area probed. The top row pertains to a clinically normal region of the cervix and the bottom row from an abnormal region in the cervix⁶.

Images from the snapshot Mueller matrix polarimeter can be observed in Figure 1.9. Three healthy human cervix are shown along with depolarization and retardance information, providing quantitative polarimetric information on the status of the tissue. These images were taken in a clinical pilot study in Mysore, India⁴.

Mayoore et al. presents a subset of images (as seen in Figure 1.10) taken by the EVA system showcasing different examples of image quality encountered in the MobileODT database. The figure shows representative images of levels of sharpness, going from low (very poor) to high (excellent)⁷.

Figure 1.11, from Kallner et al. shows sample images taken with the Gynocular through a speculum imaging a normal HPV positive cervix and a HPV positive cervix with high grade lesions⁸.



Figure 1.7 Sample images taken with the Callascope while self-imaging. [Reproduced from Asiedu et al. 2020²]

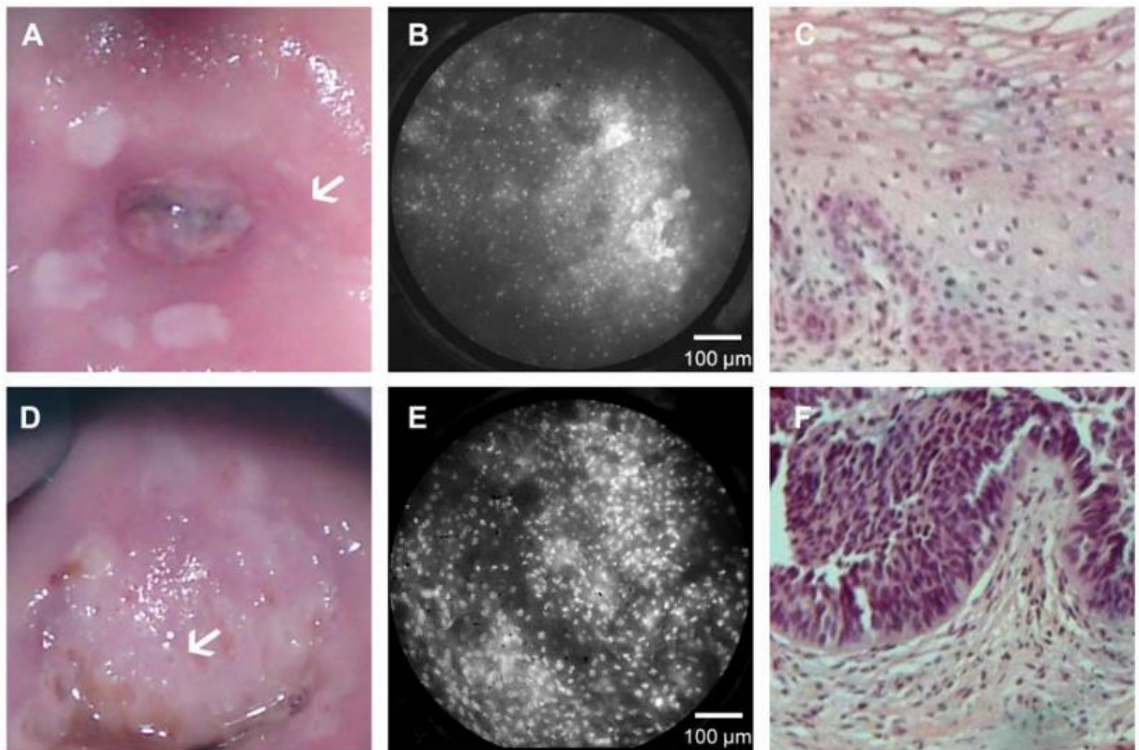


Figure 1.8 Representative cervix images of (A,D) the whole cervix, (B,E) the nuclei as seen by the HRME and the (C,F) histopathology. [Reproduced from Quinn et al. 2012⁶]

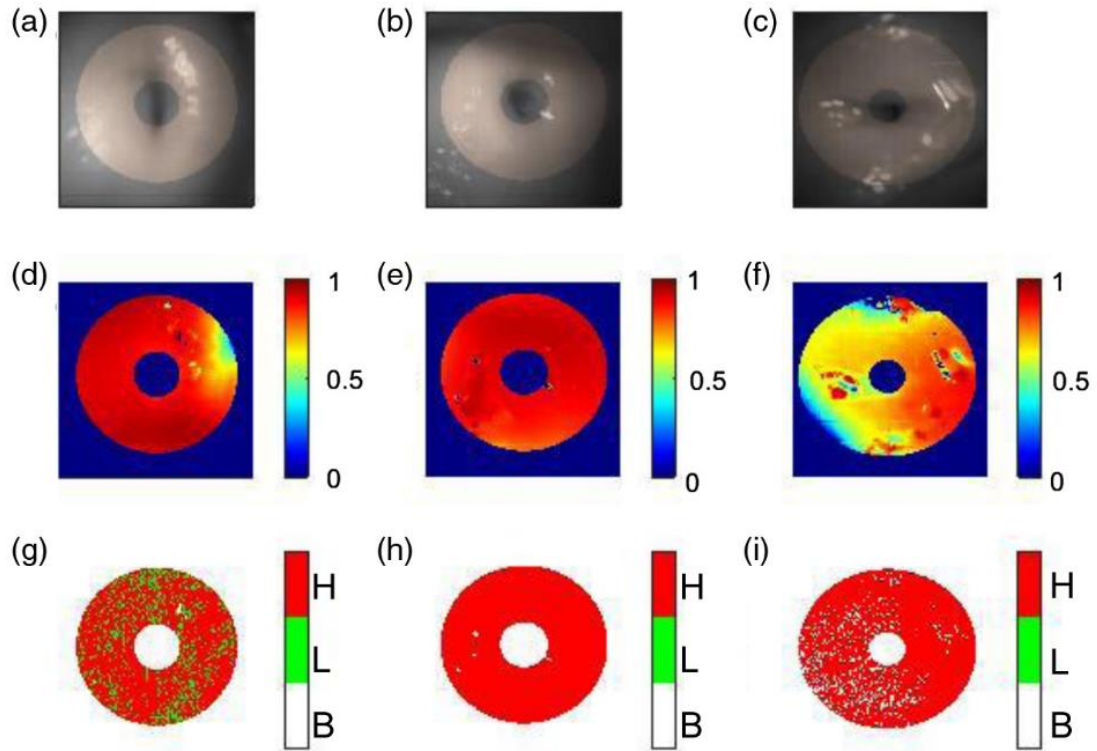


Figure 1.9 Cervical images taken by the snapshot Mueller matrix polarimeter, showing the (a-c) raw images and polarization information of (d-f) depolarization and (g-i) retardance. [Reproduced from Gonzalez et al. 2020⁴]



Figure 1.10 Example of images taken with the EVA system showing different quality of images, ranging from very poor to excellent. [Reproduced from Mayoore et al. 2018⁷]



Figure 1.11 Images taken with the Gynocular, showing a normal cervix (left) and a cervix with high grade lesions (right). [Reproduced from Kallner et al. 2015⁸]

1.4. Conclusions

We have described a set of tools for cervical imaging currently used in low-resource settings. The Callascope, the EVA and the Gynocular work similarly to a colposcope, providing images of the cervix to be examined by a physician, where the HRME and the snapshot Mueller matrix polarimeter provide more quantitative information via fluorescence and polarimetry, respectively. Excepting the Callascope, the other four devices need the aid of a speculum to capture the cervical images. The cost of these devices ranges from a \$2000-\$8200 and the weight from 480 g-2300 g, allowing portability and field use. All devices have been clinically deployed in low-resource settings, where images have been collected for physician interpretation and/or quantitative assessment.

The limitations of cervical cancer testing in low-resource settings can range from cultural and social reasons to lack of screening programs, laboratory facilities and electrical power availability. The introduction of cervical screening devices offering portability, low energy consumption, lower costs than traditional colposcopes and ability for widespread use

enable developing and developed countries with remote and low-resource populations to receive cervical screening as preventive care. These devices are also being enhanced with machine learning algorithms to improve the image quality and processing, as well as aiding in interpretation. The combination of the current available technologies for cervical imaging as a screening tool with the addition of artificial intelligence will improve the testing outcome and reduce the effect of current limitations such as interpretation errors, test result timelines and lack of manpower.

1.5 Dissertation outline

This dissertation aims to pursue the polarimetric imaging of the healthy uterine cervix in order to provide a quantification that characterizes the tissue. Moreover, the work aims at establishing a modality that can quantify cervical tissue health and can be potentially clinically deployed to be used by physicians along with established methods of cervical screening. The dissertation introduces results of the studies, which are summarized in the subsequent chapters.

The Chapter 1 introduced a literature review on cervical imaging in low resource settings, which relays information on current optical devices used for cervical cancer screening in low-resource settings and their clinical deployment. Chapter 2 explores the basic concepts of polarization, Mueller matrix decomposition and the polarimetric sensitivity of cervical collagen.

Chapter 3 focuses on the design, validation and testing of a Savart-based portable colposcope Mueller matrix polarimeter clinically deployed in the low-resource setting.

Due to the availability of new technology, such as polarized cameras, a simplified setup for Mueller matrix polarimetry became possible. In order to use the simplified setup, which reduced the number of optical elements, a new Mueller matrix decomposition method for analysis was needed. Chapter 4 focuses on the development of a reduced 3 x 4 decomposition method and its theoretical and experimental validation using various samples. Moreover, Chapter 5 further explores this newly introduced decomposition method and its deployment in biological *ex vivo* and *in vivo* samples.

CHAPTER 2 : Polarization concepts and cervical anatomy

2.1. Polarization

Polarization is a fundamental property describing the vectorial nature of light. Light has no longitudinal component and can therefore be described by two transverse components (found in the x - and y -direction). These two transverse components are orthogonal to each other and propagate longitudinally in the z -direction (orthogonal to the x - and y -direction), and therefore can be defined as:

$$[2.1] \quad E_x(z, t) = E_{0x} \cos(\tau + \delta_x)$$

$$[2.2] \quad E_y(z, t) = E_{0y} \cos(\tau + \delta_y)$$

Where x and y are the components in the x and y direction, $\tau = \omega t - kz$ is the propagator, E_{0x} and E_{0y} are the maximum amplitudes and δ_x and δ_y are the phases.

The above equations can be rewritten and upon some mathematical manipulation can be described as the following:

$$[2.3] \quad \frac{E_x^2}{E_{0x}^2} + \frac{E_y^2}{E_{0y}^2} - 2 \frac{E_x}{E_{0x}} \frac{E_y}{E_{0y}} \cos \delta = \sin^2 \delta$$

Where $\delta = \delta_y - \delta_x$

Equation 2.3 shows the optical field can be described as an ellipse and is referred to as the polarization ellipse.

Completely polarized light is elliptically polarized, although degenerate forms of the polarization ellipse exist when certain values of E_{0x} , E_{0y} and δ are encountered. For

example, linearly horizontally polarized light in the x direction is present when $E_{0y} = 0$ and linearly vertically polarized light in the y direction when $E_{0x} = 0$. Similar examples can be shown for linear +45 polarized light, linear -45 polarized light and left and right circularly polarized light.

2.1.1 Stokes vector

The polarization ellipse can describe fully polarized light, therefore cannot describe partially polarized or unpolarized light. Therefore, a new metric to describe light polarization was introduced⁷³. The Stokes polarization parameters consist of four values that can describe any polarization behavior of light in the form of a vector (ergo called a Stokes vector). From the polarization ellipse, the Stokes parameters can be written as,

$$[2.4] \quad S_0 = E_{0x}^2 + S_{0y}^2$$

$$[2.5] \quad S_1 = E_{0x}^2 - S_{0y}^2$$

$$[2.6] \quad S_2 = 2E_{0x}S_{0y}\cos\delta$$

$$[2.7] \quad S_3 = 2E_{0x}S_{0y}\sin\delta$$

The first parameter describes the total intensity of light (S_0), the second describes the linearly horizontally and vertically polarization state (S_1), the third the linearly +45 and -45 polarization state (S_2) and the fourth the right and left circulars polarization state (S_3).

The relationship between the four Stokes parameters can be described as the following,

$$[2.8] \quad S_0^2 \geq S_1^2 + S_2^2 + S_3^2$$

where the equality is true for completely polarized light and the inequality for partially polarized and unpolarized light. The Stokes vector can describe the state of polarized light through the degree of polarization (*DOP*), where

$$[2.9] \quad DOP = \frac{\sqrt{S_1^2 + S_2^2 + S_3^2}}{S_0}$$

and *DOP* is between 0 and 1, where 1 is a completely polarized light and 0 unpolarized light.

Examples of the degenerate cases of polarization, as previously mentioned in section 2.1, can be appreciated in the Stokes vectors outlined in table 2.1.

Table 2.1 Stokes vector for degenerate cases of the polarization ellipse.

Linearly horizontally polarized light	Linearly vertically polarized light
$S = \begin{bmatrix} E_{0x}^2 \\ E_{0x}^2 \\ 0 \\ 0 \end{bmatrix} = \begin{bmatrix} 1 \\ 1 \\ 0 \\ 0 \end{bmatrix}$	$S = \begin{bmatrix} E_{0y}^2 \\ -E_{0y}^2 \\ 0 \\ 0 \end{bmatrix} = \begin{bmatrix} 1 \\ -1 \\ 0 \\ 0 \end{bmatrix}$
Occurs when: $E_{0y} = 0$.	Occurs when: $E_{0x} = 0$.
Linearly +45° polarized light	Linearly -45° polarized light
$S = \begin{bmatrix} 2E_0^2 \\ 0 \\ 2E_0^2 \\ 0 \end{bmatrix} = \begin{bmatrix} 1 \\ 0 \\ 1 \\ 0 \end{bmatrix}$	$S = \begin{bmatrix} 2E_0^2 \\ 0 \\ -2E_0^2 \\ 0 \end{bmatrix} = \begin{bmatrix} 1 \\ 0 \\ -1 \\ 0 \end{bmatrix}$
Occurs when: $E_{0x} = E_{0y} = E_0$ and $\delta = 0^\circ$.	Occurs when: $E_{0x} = E_{0y} = E_0$ and $\delta = 180^\circ$.
Right circularly polarized light	Left circularly polarized light
$S = \begin{bmatrix} 2E_0^2 \\ 0 \\ 0 \\ 2E_0^2 \end{bmatrix} = \begin{bmatrix} 1 \\ 0 \\ 0 \\ 1 \end{bmatrix}$	$S = \begin{bmatrix} 2E_0^2 \\ 0 \\ 0 \\ -2E_0^2 \end{bmatrix} = \begin{bmatrix} 1 \\ 0 \\ 0 \\ -1 \end{bmatrix}$
Occurs when: $E_{0x} = E_{0y} = E_0$ and $\delta = 90^\circ$.	Occurs when: $E_{0x} = E_{0y} = E_0$ and $\delta = -90^\circ$.

2.1.2 Mueller matrix polarimetry

The Stokes vector describes the nature of polarized light (S_i where $i=0,1,2,3$) and upon interaction with a medium, this vector will change (S'_i). The modified vector S'_i can then be expressed as a linear combination of the four Stokes parameters arising from the incident beam and written in matrix form can be expressed as:

$$[2.10] \quad \begin{bmatrix} S'_0 \\ S'_1 \\ S'_2 \\ S'_3 \end{bmatrix} = \begin{bmatrix} m_{00} & m_{01} & m_{02} & m_{03} \\ m_{10} & m_{11} & m_{12} & m_{13} \\ m_{20} & m_{21} & m_{22} & m_{23} \\ m_{30} & m_{31} & m_{32} & m_{33} \end{bmatrix} \begin{bmatrix} S_0 \\ S_1 \\ S_2 \\ S_3 \end{bmatrix}$$

Which can also be written as,

$$[2.11] \quad S' = M \cdot S$$

Where S' and S are Stokes vectors and M is a 4 x 4 Mueller matrix.

A Mueller matrix is calculated by illuminating with four incident polarization states, known as the polarization state generator (PSG), and analyzing by the same four incident polarization states using a polarization state analyzer (PSA). A Mueller matrix describes the transfer function of a medium and its interaction with polarized light. It is capable of doing this by the three fundamental properties of a polarization element: depolarization, retardance and diattenuation⁷⁴. Depolarization occurs primarily due to multiple scattering. Biological tissues tend to be highly depolarizing due to structures such as collagen fibrils and organelles, among others. Retardance arises from a phase shift between two orthogonal polarization states and is exhibited commonly in fibrous structures (e.g. tendon, cornea, sclera). Diattenuation refers to the polarization dependent absorption some molecules exhibit, such as amino acids and glucose, but does not commonly affect bulk tissues⁷⁵.

2.2 Mueller matrix decomposition

The 4 x 4 Mueller matrix (M), as shown in eq. 2.11, is quantitatively interpreted through decomposition. There are various decomposition methods for the 4 x 4 matrix. The most common method used is the polar decomposition or Lu-Chipman decomposition⁷⁶ where the matrix can be decomposed into three matrices: a depolarizer with polarizance (M_{Δ}), a retarder (M_R) and a diattenuation (M_D) matrix:

$$[2.12] \quad M = M_{\Delta} M_R M_D.$$

There has also been introduced a reverse decomposition⁷⁷, that describes a depolarizer with diattenuation ($M_{\Delta r}$):

$$[2.13] \quad M = M_D M_R M_{\Delta r}.$$

The previous two decompositions differ due to the order of decomposition (Lu-Chipman produces a diattenuation matrix first and the reverse decomposition the depolarization matrix) as well as the definition of the depolarization term.

Ossikovski proposed another decomposition method, the symmetric decomposition, that introduces the idea that the depolarizing matrix could be found “in the middle” of retarder and diattenuation matrices,

$$[2.14] \quad M = M_{D2} M_{R2} M_{\Delta d} M_{R1} M_{D1},$$

where M_{D1} and M_{D2} are two diattenuator matrices, M_{R1} and M_{R2} are two retarder matrices and $M_{\Delta d}$ is the pure depolarizer matrix⁷⁸.

Moreover, there is also a differential decomposition^{79,80} where all properties are considered to be occurring simultaneously and therefore can all be represented in one single matrix.

$$[2.15] \quad m = (dM_z/dz)M_z^{-1}$$

Partial decomposition methods have also been introduced, such as the 3 x 3 decomposition, although quantitative differences have resulted when compared to the 4 x 4 decompositions^{81,82}.

2.2.1 Diattenuation

Diattenuation refers to the unequal change in orthogonal amplitudes of an optical element. The most common example of a diattenuator is a polarizer, since it has the preferentiality of one axis of polarization. This phenomenon is common in single scattering structures as well as in some biological structures with intrinsic dichroism like amino acids and glucose. The diattenuation can be described in terms of the amplitude attenuation coefficient P , where $P=1$ has no attenuation, $0 < P < 1$ has partial attenuation and $P=0$ has complete attenuation. Figure 2.1 shows how polarized light traveling along orthogonal transmission axes, E_x and E_y , can encounter a diattenuating element with amplitude attenuation coefficients P_x and P_y to emerge as components E_x' and E_y' , which are parallel to the original axes⁷³.

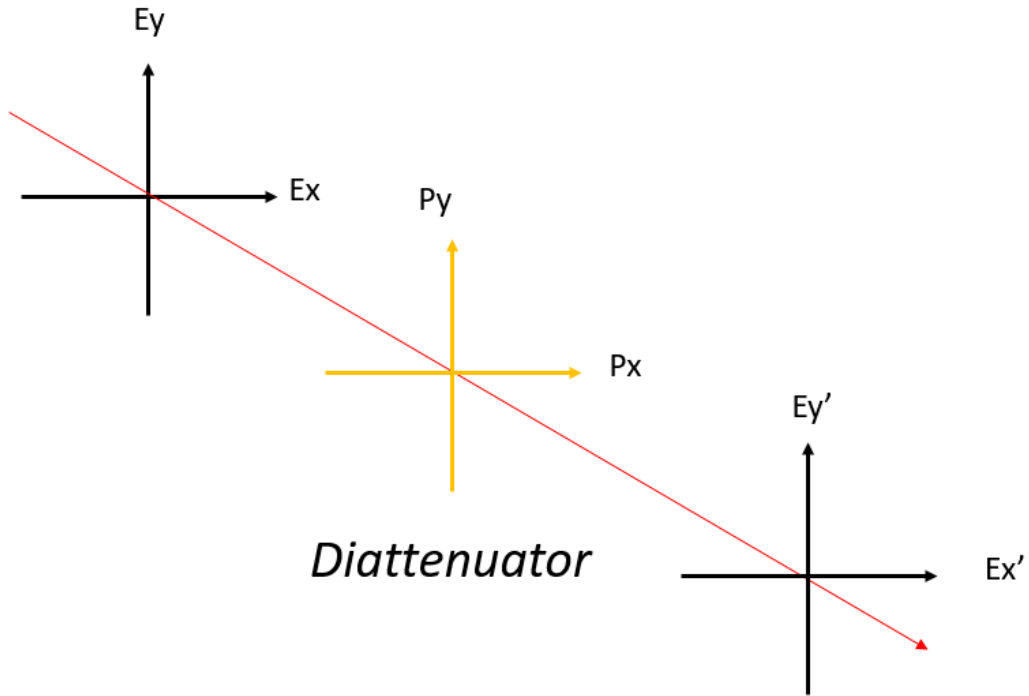


Figure 2.1 Light propagation through a diattenuator, where P_y and P_x are the attenuation coefficients. [Reproduced from Goldstein⁷³].

The diattenuation is described as 4 x 4 Mueller matrix, M_D , in the form of:

$$[2.16a] \quad M_D = \begin{bmatrix} 1 & D^T \\ D & m_D \end{bmatrix}$$

Where D is the diattenuation vector and m_D is,

$$[2.16b] \quad m_D = \sqrt{1 - D^2} \mathbf{I} + (1 - \sqrt{1 - D^2}) \hat{D} \hat{D}^T$$

Where \mathbf{I} is the identity matrix and \hat{D} is the unit vector along D .

2.2.2 Depolarization

Depolarization denotes the loss polarization, i.e. the polarized states energy becomes unpolarized energy. This occurs due to the multiple scattering of photons by a medium.

Furthermore, it is commonly seen in biological tissues and birefringence in turbid media^{75,83}. Figure 2.2 explains the event in cartoon form, where polarized light is incident on a medium with scattering properties (spheres in this case), creating a depolarizing effect.

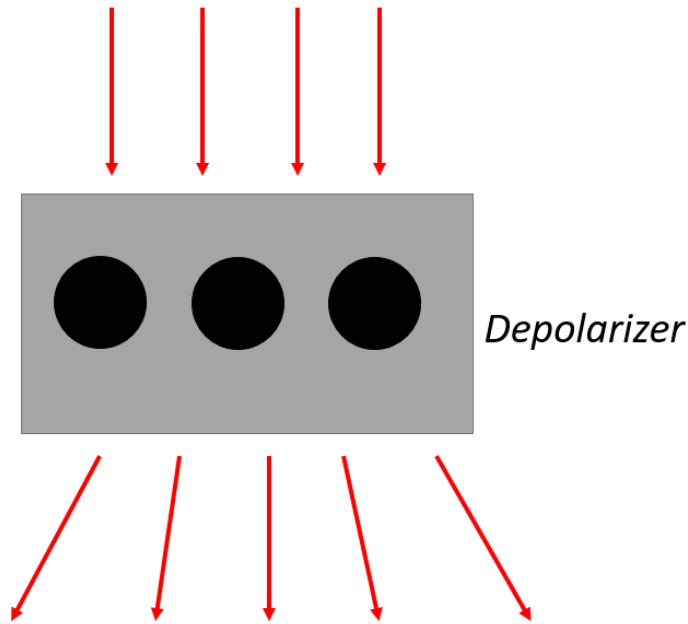


Figure 2.2 Cartoon representing a depolarizing material due to multiple scattering.

The depolarization is portrayed as a 4 x 4 matrix, M_{Δ} , (equation 2.17), where a, b are linear depolarization factors and c is a circular depolarization factor:

$$[2.17] \quad M_{\Delta} = \begin{bmatrix} 1 & 0 & 0 & 0 \\ 0 & d_1 & 0 & 0 \\ 0 & 0 & d_2 & 0 \\ 0 & 0 & 0 & d_3 \end{bmatrix}$$

with a depolarization power Δ of,

$$[2.18] \quad \Delta = 1 - \frac{|d_1| + |d_2| + |d_3|}{3},$$

2.2.3 Retardance

Retardance occurs when a phase shift is introduced between orthogonal components by an optical device. Linear retardance (δ) occurs due to phase differences between linear states, such as horizontal and vertical or 45 and -45 degrees. Circular retardance (ψ), or optical rotation, occurs due to phase differences between right and left circularly polarized states⁸⁴. In general, retardance is caused by birefringence, anisotropic structures and optical rotation in chiral molecules. A common example of a retarder is a wave-plate. Biological examples include fibers such as elastin and collagen. Figure 2.3 shows polarized light propagating through orthogonal transmission axes, E_x and E_y , and encountering a retarder with a phase shift of $-\phi/2$ along the y axis and phase shift $+\phi/2$ along the x axis, creating an emerging beam $E_{x'}$ and $E_{y'}$.

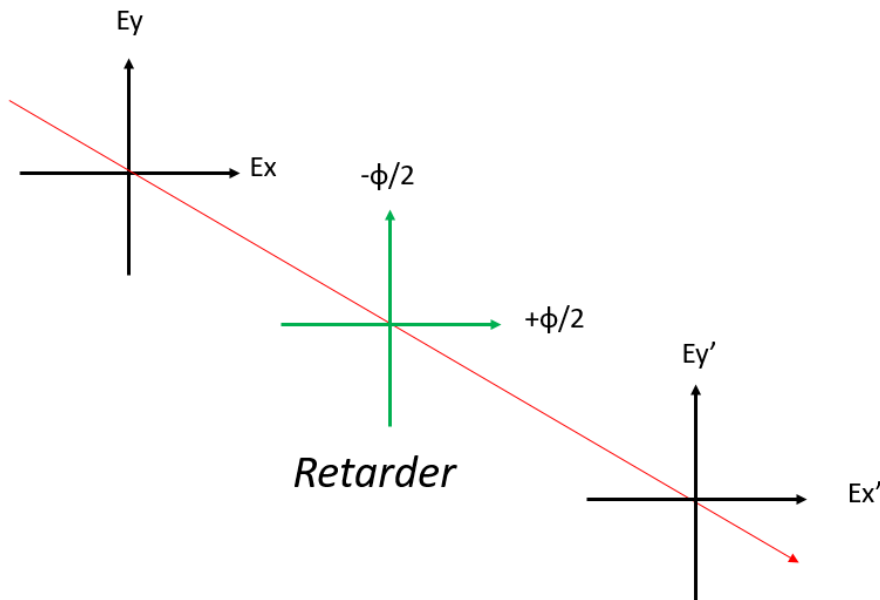


Figure 2.3 Illustration of light propagating through a retarder, where phase shifts $-\phi/2$ and $\phi/2$ can be seen in the y and x axis, respectively. [Reproduced from Goldstein⁷³].

A 4 x 4 Mueller matrix describing the retardance, M_R , can be seen below:

$$[2.19a] \quad M_R = \begin{bmatrix} 1 & 0^T \\ 0 & m_R \end{bmatrix}$$

Where,

$$[2.19b] \quad m_R = \begin{bmatrix} m_{11} & m_{12} & m_{13} \\ m_{12} & m_{22} & m_{23} \\ -m_{13} & -m_{23} & m_{33} \end{bmatrix}$$

2.2.4 Mueller matrix and cervical tissue

Cervical cancer is associated with microstructural alterations in collagen content and cellular organization^{85,86,87}. Due to collagen's birefringence, Mueller matrix polarimetry (MMP) can be used to observe these changes. MMP is a mathematical approach used to distinguish collagen fibers from images taken to contrast and highlight areas where collagen behavior has changed from normal in the cervix⁸⁸. Healthy cervixes show a pattern of circumferential alignment of fibers around the os. MMP uses noninvasive widefield optical imaging (which can capture the full cervix) and the Mueller matrix polarimetry to differentiate between cancerous and normal tissues based on the polarization signature of the tissue, such as retardation and depolarization. For healthy, highly aligned tissue, retardation and depolarization are expected to be high⁸⁹. When a cervix becomes diseased, its polarization properties change—the retardance and depolarization become lower⁸⁸. The change in depolarization of linear and circular polarized light occurs due to the structural alteration in the stroma during the precancerous changes. The changes in polarimetric response from the cervix comes from the degradation of linearly arranged collagen fibers, as well as the collagen cross-links breaking in the stromal region. Moreover, a change in

the scattering density of the cervical cancer sites has been reported⁹⁰. The progression of pre-cancerous lesions can be noted by a reduction in collagen crosslinks concentration and collagen fiber breakdown⁹¹. Collagen density in the cervical stroma is an important marker for precancerous developments. It has been noted that alterations in stroma precede and promote neoplastic progression and therefore monitoring it is useful for early detection of precancerous changes²⁸.

CHAPTER 3 : Design and implementation of a portable colposcope Mueller matrix polarimeter

3.1. Introduction

Cervical cancer is the fourth most common cancer in women worldwide, with an estimated half a million new cases and 311,000 deaths each year¹⁰. Developing countries suffer about 84% of the global burden of disease and 80% of the mortality due to a lack of effective screening programs. The hardest-hit regions are among the world's poorest with incidence rates over 35 per 100,000 women compared with 3 per 100,000 women or lower in North America and Europe⁹². Because the disease progresses over many years, an estimated 1.4 million women worldwide are living with cervical cancer, and two to five times more—up to 7 million—may have precancerous conditions that should be identified and treated¹¹. While several prophylactic HPV vaccines are now available in more than 100 countries for primary prevention⁹³, they do not target all 15 high risk HPV types, ergo there is still a need for screening⁴⁶. Moreover, due to cost-effectiveness issues of vaccination in low and middle income countries (LMICs), it is often seen that the only available prevention method is regular screening and treatment of precancerous lesions⁹⁴.

In India, cervical cancer is the second most common cancer among women aged 15–44 years^{95,96}. There are about 122,844 new cases and 67,477 deaths annually among the approximately 432.2 million women at risk^{96,97}. As with other low-income countries, traditional cytology-based diagnostics are largely impractical for population-based screening because of cost, inadequate infrastructure, lack of skilled health care workers and laboratories⁹⁸. While guidelines for population-based screening have been established for more than a decade, it has been estimated that less than 4% of at-risk women have currently

been screened for cervical cancer⁹⁵. Several states in India have initiated pilot programs examining the effectiveness of visual inspection with acetic acid (VIA) for diagnosis of cervical neoplasia^{99,100}. In India, VIA would be considered the current best alternative, although it has several important limitations with 71.8% sensitivity, 79.4% specificity, positive predictive value of 16.7% and negative predictive value of 99.0%³⁷. The high potential for false positives in VIA is a great concern^{101,102,103} since it can lead to excessive testing and overtreatment including unnecessary colposcopies, biopsies, cryosurgery, and hysterectomies as evinced by programs in Nepal and India^{104,105}.

Low-cost optical technologies such as the High Resolution Microendoscope (HRME)^{106,107,108}, the Point of Care Tampon based digital colposcope (POCKeT Colposcope)¹⁰⁹, or the cellphone based MobileODT system¹¹⁰ are being proposed but have limitations. HRME is a point measurement (~ 500 μ m in sampling size) that is still guided by physician expertise while POCKeT and MobileODT focus only on acquiring digital image and still require expert review of the data^{109,110} although machine learning approaches are being tested at present.

The cervix is composed of structural tissue exhibiting birefringence^{111,112} arising by its molecular structure, as well as its very ordered arrangement within the stroma. It consists of ~ 70% collagen fibers, elastic fibers^{113,114} and a ground mixture of biomolecules (e.g. proteins and nucleic acids). The circumferentially aligned cervical collagen structure^{115,116,117,118} found around the os can be monitored with polarimetric techniques, such as Mueller matrix polarimetry (MMP) and deviation from the standard ordered structure can be used to pinpoint pathological areas¹³. A Mueller matrix completely characterizes the polarimetric properties of a sample^{119,120}. Using Mueller matrix

decomposition (MMD) (as proposed by Lu-Chipman¹²¹), we can obtain three canonical matrices $M = M_{\Delta}M_R M_D$: a diattenuator matrix M_D , M_{Δ} accounting for the depolarizing effects of the material and a retarder matrix M_R . Furthermore, the resulting matrices can be analyzed to yield quantitative medium properties¹²² that have a demonstrated useful diagnostic power⁸⁸. Of particular relevance to this study is the angle α , which is directly related to the orientation of the long axis of the collagen bundles in the tissue and the optical retardation R which is related to collagen density.

Mueller Matrix Imaging (MMI)^{64,123,124,125} has been proposed as an alternative to standard screening by several groups, and focuses on subtle changes in cervical collagen structure typical of cervical precancerous lesions to provide a quantifiable map of cervical alteration in the ectocervix. For example, differences in retardance and depolarization have been shown in normal versus pathologic states^{13,88,126}. A recent ex-vivo study utilizing MMI has showed a sensitivity and specificity of 83% of normal versus high grade lesion tissues¹²⁴, higher than the previously mentioned VIA testing. Our group has used MMI to target the fibrous ultrastructure (i.e. collagen) organization of the cervix¹²⁷. We have developed a clinical Mueller matrix system^{128,129} based on a standard colposcope with high sensitivity to the cervix ultrastructure. We have tested the system on healthy volunteers, as well as have measured collagen arrangement and distribution non-invasively, and have positively compared our findings to other microscopic techniques such as Optical Coherence Tomography¹³⁰.

This paper describes the extension of the aforementioned study with the realization of a portable snapshot system based on Savart plates that can be deployed in low resource settings. We hypothesize that the use of this MMI system can provide fast-acquired

quantitative images of the cervix that can be used during the cervical screening process to provide feedback by identifying probable pathologic areas. A pilot study introducing the potential clinical use of the device is presented. This work can translate to improving cervical cancer screening by providing a quantitative platform, which could in the future increase the diagnostic power of VIA and other screening modalities, that is low cost and portable.

3.2. Methods

The snapshot Mueller Matrix polarimeter consists of two different elements: a Polarization State Generator (PSG) and a Polarization State Analyzer (PSA). The PSA is designed to have a field of view of 30 mm, operating wavelength 633nm, and a magnification of 0.5. In the PSA, Savart plates divide the light into four separate paths, each with intensities proportional to the polarization information of the object, Figure 3.1. The four separate channels are recombined by an imaging lens onto the camera creating a spatial interference pattern.

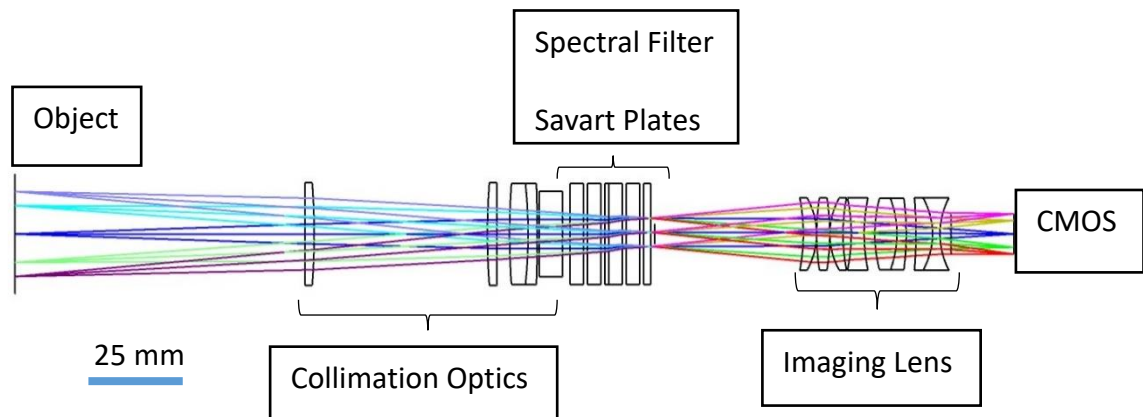


Figure 3.1. Optical layout of the PSA portion of the system.

The contrast of these fringe patterns is a function of the Modulated Transfer Function of the optics and the polarization properties of the object, Figure 3.2. To recover the polarization properties of the object different reconstruction methods can be utilized.

131,132,133

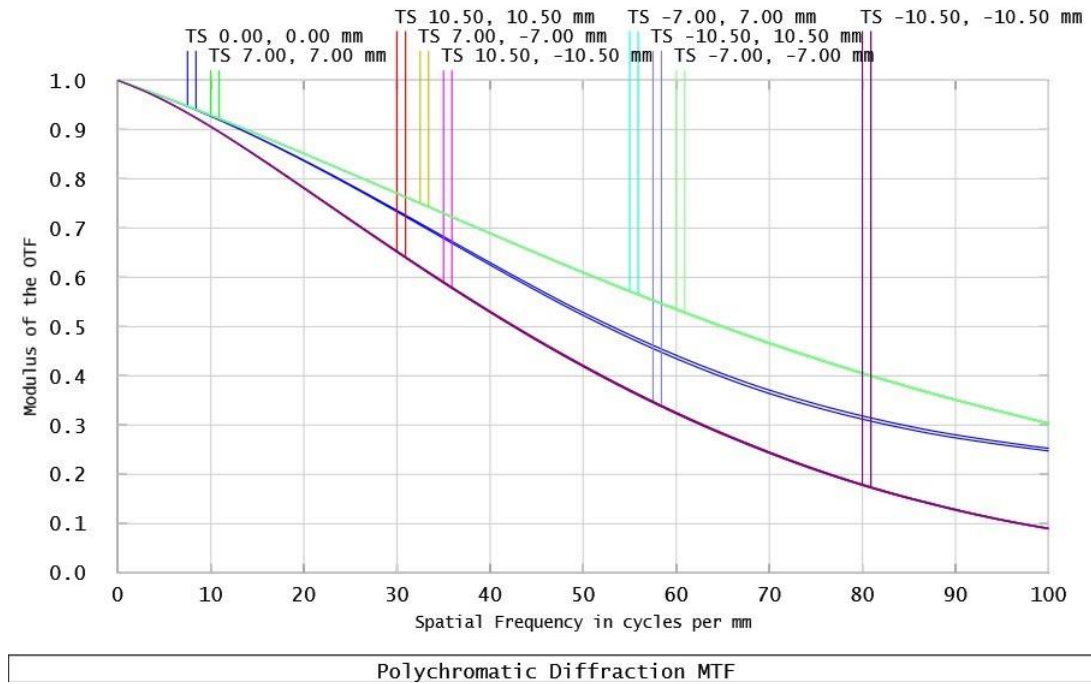


Figure 3.2. MTF of the Savart Polarimeter.

In one method, a Fourier transform is performed on the image. Applying spatial filters and an inverse Fourier transform results in an image of the polarization information of the object. The process is described in detail elsewhere^{131,132}. A second method, the sliding reconstruction approach¹³³, is also used. Both methods require the acquisition of calibration images: 0 and 45 degrees linearly polarized beam for the Fourier method and 0 degrees linearly polarized, 45 degrees linearly polarized and right circularly polarized for the Sliding Reconstruction method.

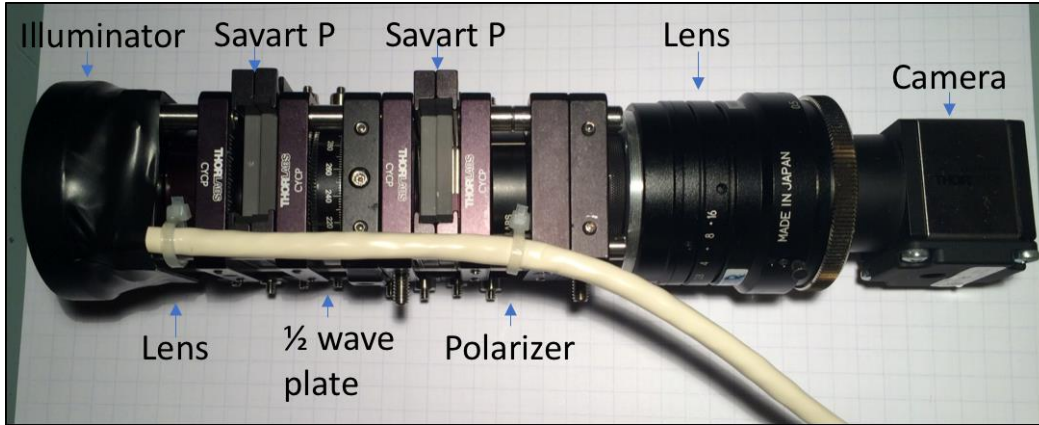


Figure 3.3. The snapshot Mueller matrix polarimeter

Our system consists of 4 Calcite Savart plates 25 mm x 25 mm x 3.72 mm (United Crystals LLC) with 20/10 surface quality; parallelism less than 3 arc-minutes and AR coating (Angle of Incidence 0 – 30 deg. $R_{avg} < 0.5\%$ for wavelengths 500 – 800nm). A $\frac{1}{2}$ achromatic wave plate (Thorlabs Inc.), a 50 mm EFL imaging lens (MLV 50M1, Thorlabs Inc.) and a High-Sensitivity USB 3.0 complementary metal oxide semiconductor (CMOS) Cameras with Global Shutter (DCC3240C, Thorlabs Inc.) capable of 60 frames per second at full resolution 1280 pixels x 1024 pixels.

An image of the full system is shown in Figure 3.3. Theoretically, this system can resolve spatial frequencies between 70 to 100 lp/mm on the detector, Figure 3.2. These frequencies correspond to features ranging from 20 to 30 μm on the object, which is well within the range needed to resolve the features of interest.

The Snapshot system can acquire one full Stokes vector within one snapshot. Since we are interested in obtaining a full Mueller matrix, four different states of input polarizations are necessary. In previous work, three linear states (0, 45° and 90° to the reference plane and right circularly polarized) have been utilized and shown to be optimal⁸⁴.

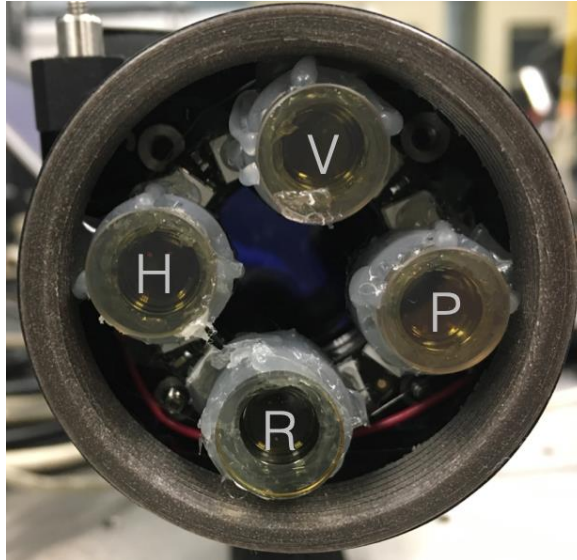


Figure 3.4. Polarization state generator. H is a horizontally aligned polarizer (with respect to the reference frame, optical bench), V is a vertically aligned polarizer, P is a 45 degrees aligned polarizer, and R is a circular polarizer

The requirement of our system to be portable, computer controllable and easy to use by non-experts has led to the choice of a preassembled set of light emitting diode (LED) for our PSG, Figure 3.4.

A NeoPixel Ring (Adafruit, New York, NY) with 16 Red Green and Blue LED with Integrated Drivers was used in this system. Four LEDs were chosen on the ring and were paired with a small diffuser and cellphone lenses. Overlapping spot size of 3 cm were then achieved at a distance of about 10 cm for each LED. The LEDs spectral bandwidth at

the operating wavelength of 633 nm was 10 nm Full Width Half Max (FWHM). The LEDs were connected to an Arduino Mini and a custom driver was developed to control the board through MATLAB (MathWorks, Natick, MA). Given the small dimension of the Mini it could be integrated into a cable.

A graphical user interface (GUI) was designed in MATLAB to control acquisition and illumination. The program operates in two different modes. In focusing mode, all four LEDs are activated at half of their power setting and the camera acquires at 60 frames per second. Once appropriate focus onto the cervix is achieved, the acquisition mode begins by switching off all LEDs. Then, each LED is activated in sequence and after each activation, an image is acquired. Finally, the four images are combined into a stack and saved without any filtering or manipulation. Total acquisition time is about 1 second.

Data acquired with the system is analyzed in post-processing. Mueller matrix images are decomposed with a process illustrated by Lu-Chipman¹²¹. Retardation, depolarization, attenuation, and orientation images are created.

3.2.1. Image processing

Data analysis was performed primarily using the Fourier reconstruction method. A second methodology known sliding reconstruction method was also explored. Both methods are illustrated below.

3.2.1.1. Fourier reconstruction:

In this reconstruction method, the fringe coded image is Fourier transformed¹³⁴ and the extracted amplitudes and phases are used to determine the Stokes parameters.

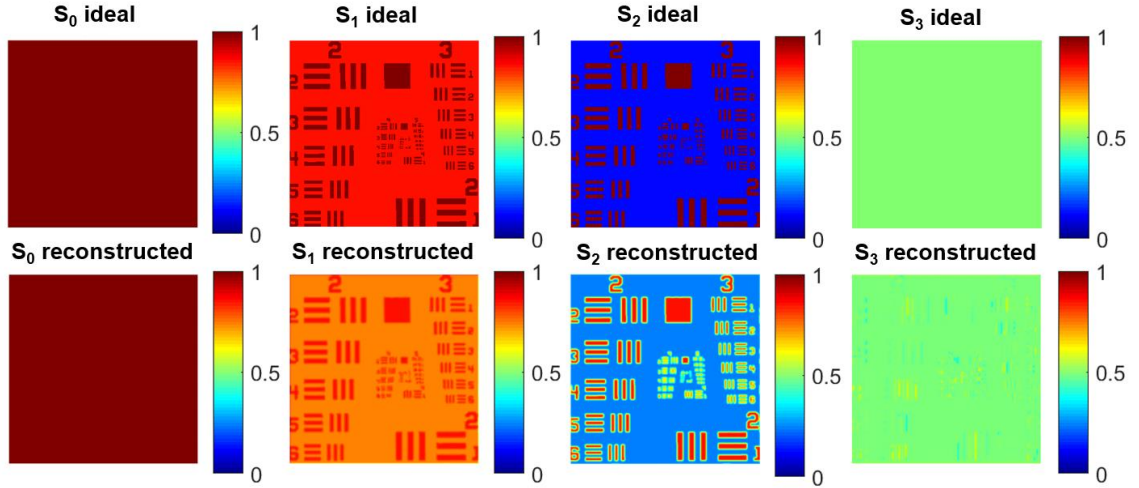


Figure 3.5. An input Stokes vector was created with a USAF target (top figure). The status of polarization corresponds to a linear orientation of 22.5 degrees for the background and 0 degrees for the lines. The bottom figure shows the Stokes vector after reconstruction. There are still visible artifacts (traces from the target) where the Fourier reconstruction failed.

Solving for the FFT of the output signal (equation 3.1), a set of spatially independent values each carrying polarization information is observed. Many examples of this approach with ideal input Stokes vectors can be found in the literature^{135,136,137,138}. Here we focus on a United States Air Force 1951 (USAF) target. Some of the artifacts associated with the methodology, such as errors in reconstruction in the presence of edges, can be noted in Figure 3.5, e.g. S_3 reconstructed shows traces of the target meanwhile S_3 ideal does not.

The intensity I of the interference pattern relates to the incident Stokes vectors according to the following equation¹³⁹:

$$\begin{aligned}
 [3.1] \quad I(x, y) = & \frac{1}{2}S_0 + \frac{1}{2}S_1 \cos(2\Omega(x + y)) \\
 & + \frac{1}{4}|S_{23}| \left| \cos[2\pi(2\Omega)x - \arg(S_{23})] - \frac{1}{4}|S_{23}| \left| i \cos[2\pi(2\Omega)y + \arg(S_{23})] \right. \right.
 \end{aligned}$$

$$S_{23} = S_2 + iS_3 \quad \text{and} \quad \Omega = \frac{\Delta}{\lambda f}$$

Ω is the frequency of the spatial modulation, λ is the wavelength, Δ is the sheer distance of the Savart plates and f is the focal length of the lens closer to the camera.

This image I is shown in Figure 3.6(a) together with its two-dimensional Fourier transform Figure 3.6(b).

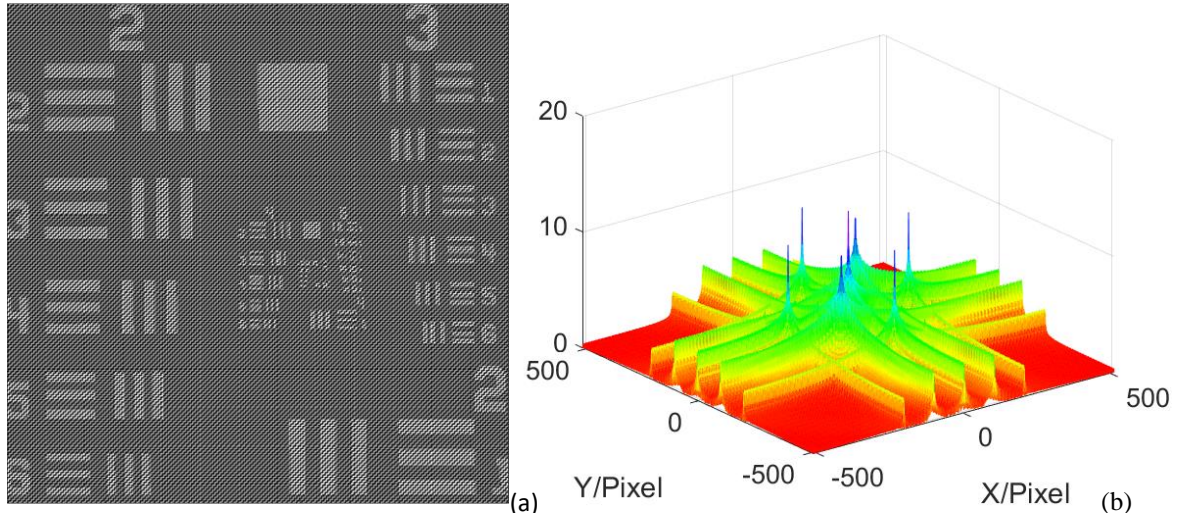


Figure 3.6. (a) Interferogram associated with the USAF test target as seen by a camera sensor, (b) Fourier transform of the interferogram of the USAF target, featuring the peaks (along with the full frequency profile) where the Stokes vectors are spatially encoded within the interferogram.

The spatial position of the four Stokes element vector is known and depends on the source wavelength, the thickness of the Savart plates, and the focal length of the imaging lens. A filter can be designed to extract the Stokes parameters in the Fourier domain for each state of polarization. This application utilizes three Gaussian filters to extract Stokes vectors S_0 , S_1 and S_2 , which is applied to the interferogram in Figure 3.6(b). The Gaussian filters and effect of the filter bandwidth in relation to the Stokes vector output

can be seen in Video 1. The filtered image is then inverse Fourier transformed and normalized.

The normalization utilizes two reference images: 0 (S_{ref0}) and 45 degrees (S_{ref45}) linear polarizations. The reference images must undergo the same reconstruction process as previously mentioned. The final Stokes vectors, after reconstruction and normalization, will be as shown in equations 3.2a-d.

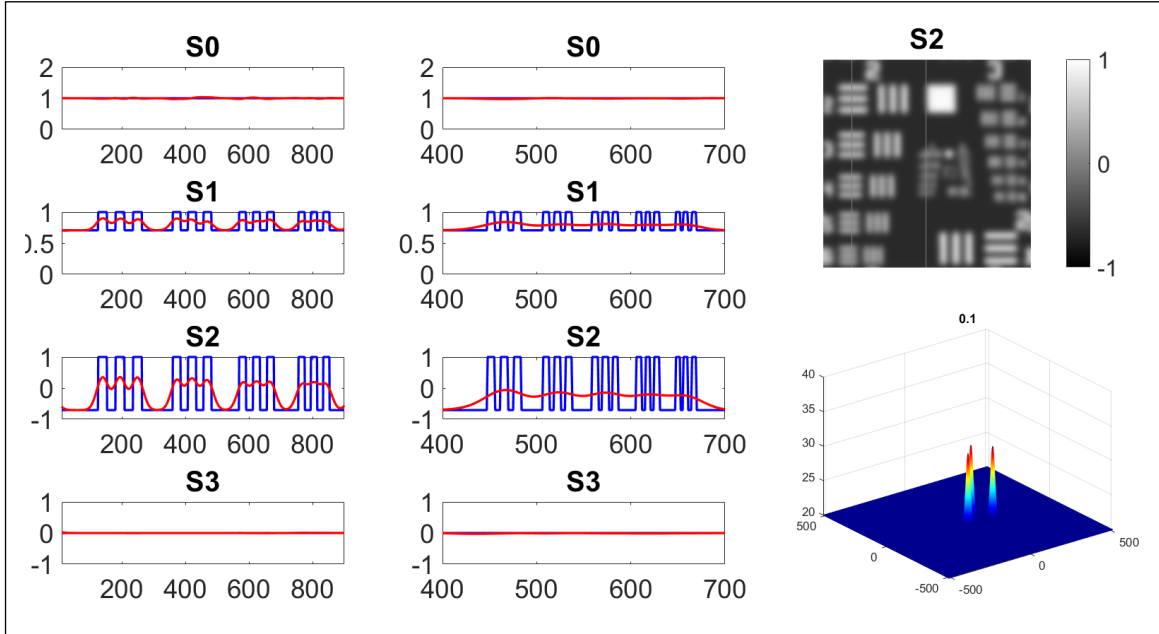
$$[3.2a] \quad S_0 = \Re \left(\frac{S_0^*}{S_{ref0}} \right)$$

$$[3.2b] \quad S_1 = \Re \left(\frac{S_1^*}{S_{ref0}} \right)$$

$$[3.2c] \quad S_2 = \Re \left(\frac{S_{23}^*}{S_{ref45}} \right)$$

$$[3.2d] \quad S_3 = \Im \left(\frac{S_{23}^*}{S_{ref45}} \right)$$

The effect of the filter on the image is shown in the video below.



Video 1. Filter design changes both the quality of the reconstructed Stokes vector and image resolution. Two traces (red and blue) are shown on the figure displaying differences in the original Stokes vector and the reconstruction (*lines are shown in S2 image*). Two examples are shown, one for the largest (first column) and smallest (second column) block of resolution dashes in the USAF target using the same filter. The filter appearance is shown in the bottom right of the figure as the bandwidth changes. (MP4, 2.55 MB)

3.2.1.2. Sliding reconstruction

A second approach to reconstruction, the sliding reconstruction method, was introduced by Murali¹³³ and does not rely on Fourier analysis but on direct matching of the interference pattern.

The light intensity exiting the Savart plates can be written as,

$$[3.3] \quad O(x, y) = S'(x, y) = \left(\frac{1}{2}\right) \left[\begin{array}{l} S0(x, y)F0(x, y) + S1(x, y)F1(x, y) + S2(x, y)F2(x, y) \\ + S3(x, y)F3(x, y) \end{array} \right]$$

where $O(x,y)$ is the intensity of the light , $S_0(x,y)$, $S_1(x,y)$, $S_2(x,y)$, $S_3(x,y)$ are the Stokes components of the light entering the crystals and $F_0(x,y)$, $F_1(x,y)$, $F_2(x,y)$, $F_3(x,y)$ form the first row of the Mueller matrix elements.

The Stokes components are estimated over the entire image. A unit cell, a 3×3 kernel in this case, is moved by one pixel either along the column or row. In order to compensate for multiple pixel calculations, the average value of the multiple reconstructions of the Stokes component is taken. Three reference images are needed for this reconstruction method: 0 (S_{ref0}), 45 degrees (S_{ref45}) and right hand circular (S_{refRHC}). The reconstruction using the sliding reconstruction method can be observed in Figure 3.7.

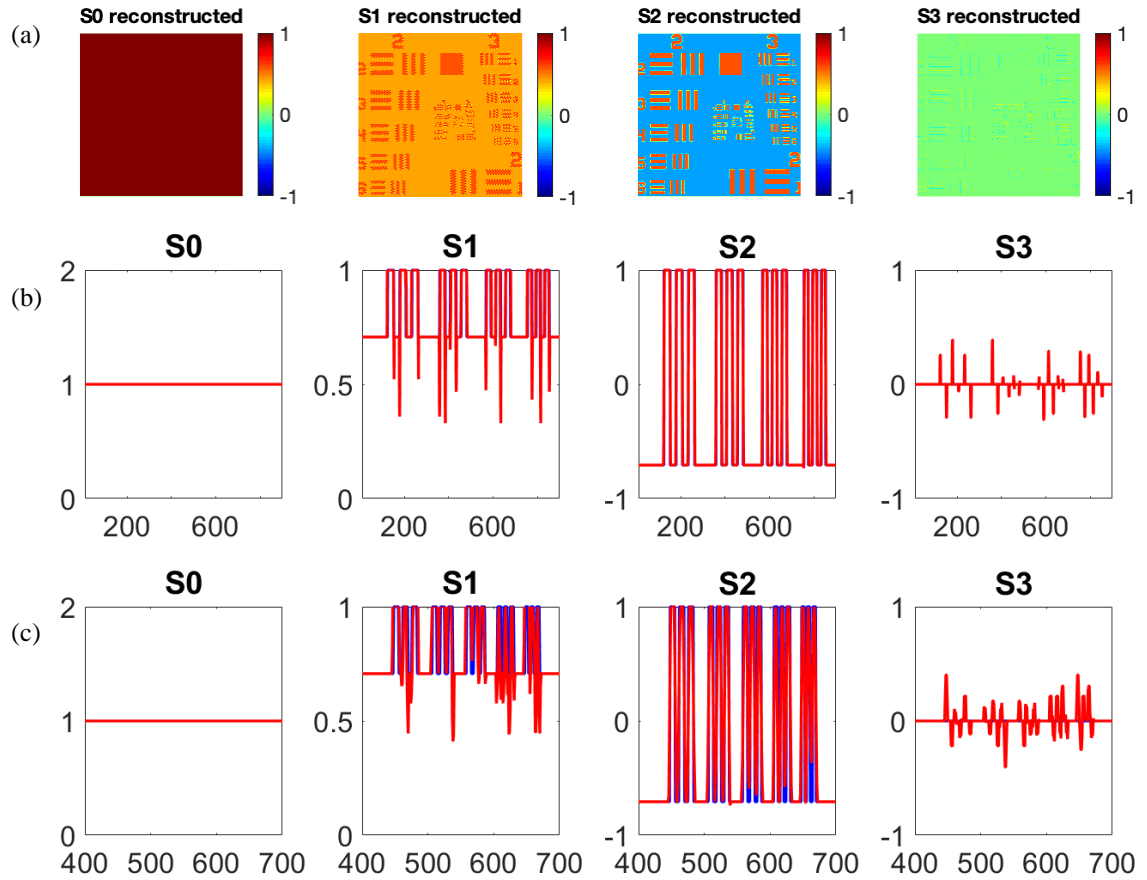


Figure 3.7. Stokes vector of a USAF target reconstructed with the sliding reconstruction method (a) showing traces of the (b) largest and (c) smallest blocks of resolution dashes. As can be observed from the changes from the raw signal to the reconstructed signal, strong discontinuities create artifacts in the Stokes images.

The Stokes vectors produced using the reconstructions were used to populate the Mueller matrix in order to perform the MMD. This process has been extensively explained elsewhere^{76,84,127}.

3.2.2. Anisotropic and ex vivo biological samples

The portable colposcope was first tested with optical elements of known Mueller matrices (air, linear polarizers) as well as an extruded silicone phantom and an *ex vivo* porcine cervix before being used in a pilot study in Mysore, India. The extruded silicone phantom

consisted of a silicone strip with visible striations along the same direction. This sample has known polarimetric properties and is often used for device validation⁷⁴. The material's transparency allows for minimal polarization information loss, due to its low absorption and scattering. The polarimetric system was also tested with an *ex vivo* paraffin embedded porcine cervix—the embedding process can be found in detail elsewhere¹²⁷. The porcine cervix has a circumferentially aligned collagen structure around the os, similar to the human cervix, and therefore exhibits similar polarimetric properties¹³⁰. A Mueller matrix system utilized in a previous study was also used to validate our newly developed apparatus¹²⁷.

3.2.3. Clinical deployment

The evaluation of our system on healthy patients study was added to an ongoing screening protocol in a mobile clinic in Mysore, India. Patients were recruited among the ones coming for gynecological evaluation and Papanicolaou (Pap smear) testing. An IRB protocol (IRB-17-0181) was approved by Florida International University Institutional Review Board as well as the Public Health Research Institute of India's Institution Ethics Review Board (2016-20-08-34) and informed consent was obtained from all subjects. A total of 22 study participants were recruited. Eligibility criteria included: 1) age ≥ 18 years, 2) willing to undergo imaging, and 3) having the capacity to undergo informed consent process. Participants were screened for eligibility via chart review at the time of appointment. All eligible women were provided information about cervical cancer, study risks and benefits. A brief data collection instrument was used to collect sociodemographic and medical information about each participant.

After recruitment, the patients underwent a standard gynecological exam that included a cervical inspection. For this purpose, a speculum was utilized to dilate the vaginal canal and access the cervix. Two strategies were devised for cervical visualization and positioning of the system for imaging. First, the system was mounted on a portable tripod that could be easily moved in front of the patient once the speculum was inserted. Second, the acquisition program was projected onto the screen of an iPhone 6 connected to the tripod. This was done with a commercially available app called Duet. This strategy is similar to having an eyepiece on a colposcope and allowed the system user to see and position the Savart system more efficiently rather than diverting his/her attention to a computer screen. The system was self-powered and required short acquisition time (~1 second). The overall imaging portion of the study took about 10 minutes per patient. Little training was required in order to implement device deployment (less than 15 minutes). Finally, post imaging, patients were administered the Pap smear.

3.3. Results

The error of the portable device was measured by taking the Mueller matrix of air. Figure 3.8 shows the Mueller matrix image of air obtained in transmission (light source positioned facing the PSA) displaying a typical unit matrix behavior. The total error in these images was well below 5%, but some structural error is perceivable in the images.

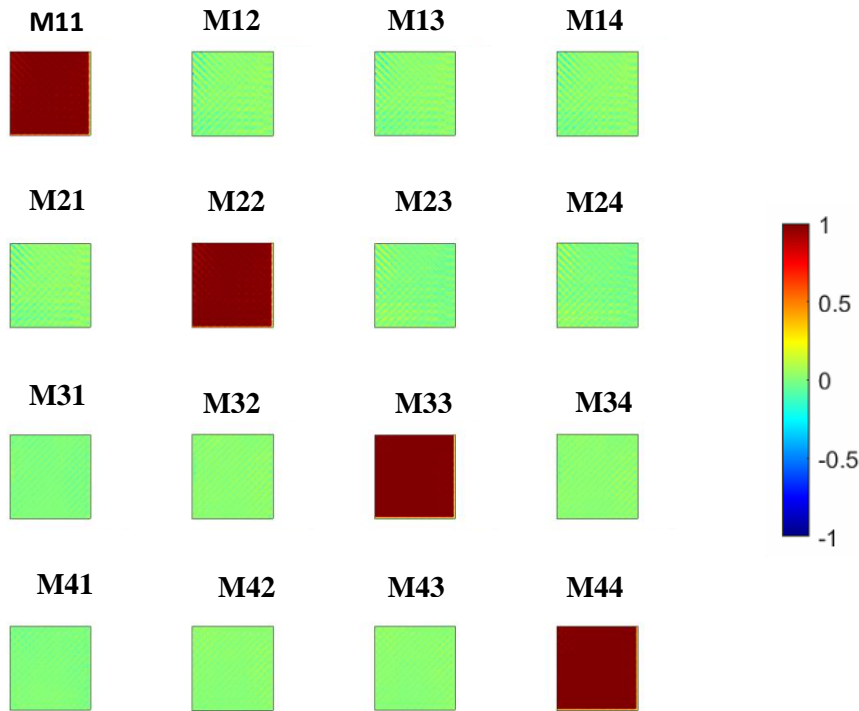


Figure 3.8. Mueller Matrix of air. The portable device was tested in transmission to understand the error of the polarimetric response. Although some structural artifacts are present (small white lines in the matrix), the expected values of ones in main diagonal elements are present.

The system was then tested with a silicone phantom. The phantom's uniformity makes it a reliable target to validate the MMI system. The phantom was positioned at different orientations with respect to the system's reference frame. Figure 3.9 displays the extruded silicone phantom shifted 22 degrees from the reference frame. On the left (Figure 3.9a), the raw image with the interferometric pattern can be seen in gray with the colored region of interest highlighted. The image on the right (Figure 3.9b) show the calculated angles (α), which were in agreement with the positioning of the phantom.

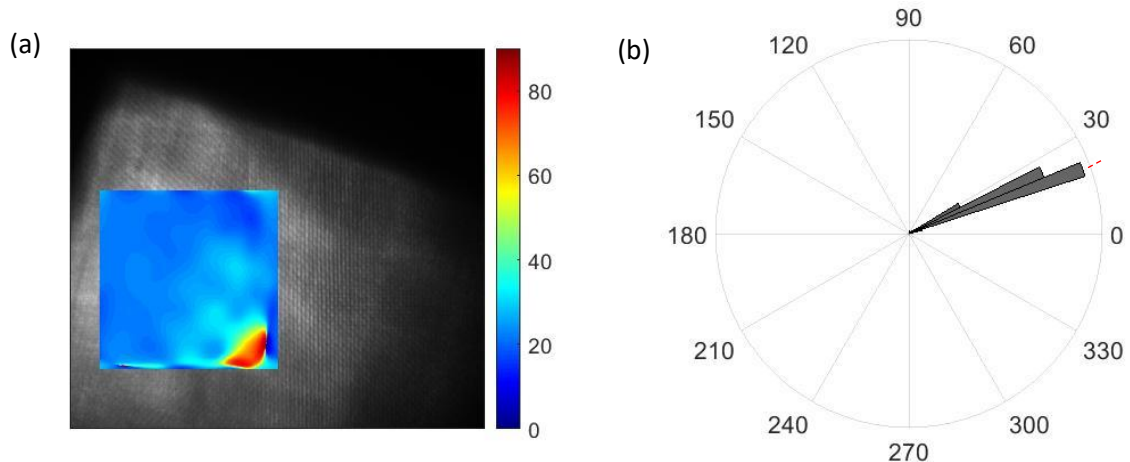


Figure 3.9. Extruded silicone sample recovered orientation. The silicone sample was placed at a 22 degrees shift (marked in the red line) from the frame of reference. (a) Raw image (gray scale) with the recovered mean angle of a region of interest (colormap), (b) circular histogram of the recovered angles.

In order to understand the portable colposcope's response to biological samples, the *ex vivo* paraffin embedded porcine cervix was imaged. The zone of interest, which is the area between the os and the outer layer of the cervix, was determined by choosing a region of interest in the mid-section of the cervix. The os and the outer cervix have longitudinally aligned collagen and therefore are excluded from the polarimetric evaluation.

Biological samples are strongly depolarizing due to their high scattering and absorbing nature. The polarized light interaction with collagen crosslinks also cause high retardance. Highlighting the zone of interest, we can observe a high level of depolarization ($MD_{ave}=0.96$) and retardance ($MR_{ave}=26^\circ$) exhibited by the porcine cervix (Figure 3.10a-c), as we had expected. The depolarization is quantified from 0 to 1, going from low to high, respectively. The retardance is measured from 0 to 90 degrees. Figure 3.10(d-e) portrays the distribution of depolarization and retardance, respectively, which shows a

similar outcome to what has been reported by Chue-Sang *et al.*¹²⁷ for the paraffin embedded porcine cervix.

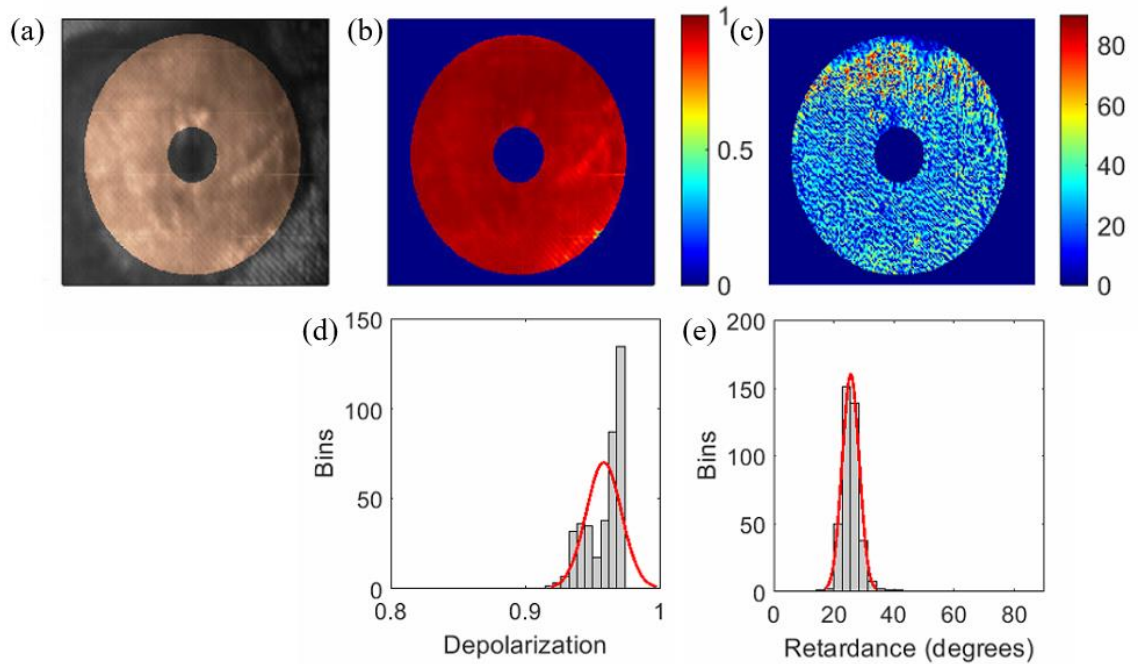


Figure 3.10. Ex vivo paraffin embedded porcine cervix. (a) Raw image highlighting region of interest, (b) Mueller matrix decomposed depolarization, (c) Mueller matrix decomposed retardance (d) distribution of depolarization and (e) distribution of retardance angles.

The portable colposcope was further tested in a clinical pilot where *in vivo* human imaging took place. The average age of women imaged was 35 ± 8 years old. Of the 22 patients imaged, six were deemed unsatisfactory due to image quality and therefore have been excluded from the resulting analysis. The remaining 16 patients received clinical assessments summarized in Table 3.1. Three patient images and corresponding Mueller matrix decompositions are reported in Figure 3.11. The zone of interest is highlighted superimposed over the raw images (a-c). The three cervixes show a high level of depolarization (d-f) and retardance (g-i), as expected of healthy tissue.

Table 3.1 Patient age and clinical evaluation performed by a physician.

Patient #	Age	Clinical evaluation/Pap smear
1	50	Polyp (green)
2	30	Negative (gray)
3	45	Negative (gray)
4	36	Negative (gray)
5	33	Negative (gray)
6	37	Neutrophils (cyan)
7	30	Negative (gray)
8	23	Negative (gray)
9	29	Inflammatory (red)
10	29	Inflammatory (red)
11	34	Negative (gray)
12	50	Atrophic with inflammation (purple)
13	40	Inflammatory (red)
14	40	Inflammatory (red)
15	28	Negative (gray)
16	30	Negative (gray)

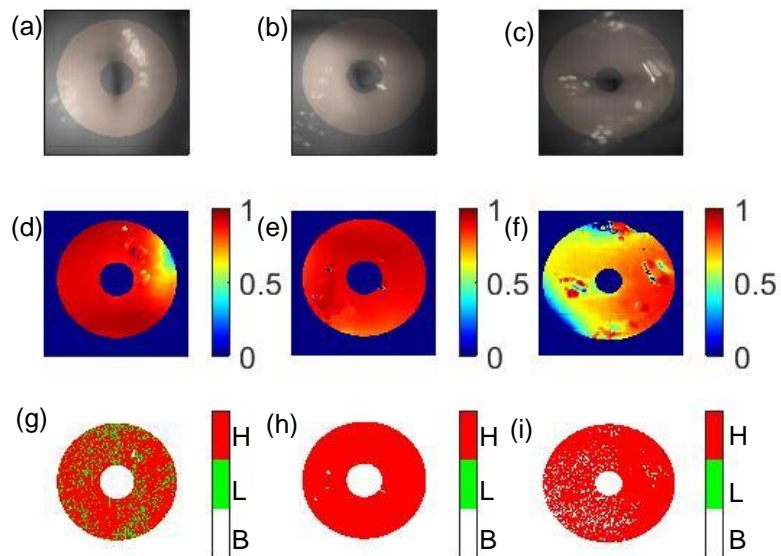


Figure 3.11. In vivo healthy human cervixes with negative clinical evaluations (a-c) raw images with the highlighted region of interest, (d-f) the depolarization and (g-i) the

retardance portrayed as a binary high (H, red)/low (L, green) with zero background (B, white) using a threshold of 25 degrees.

In Figure 3.11 the region of interest along the circumferential zone can be seen superimposed in the raw images. The devices exhibit high depolarization and retardance values, as have been reported for healthy cervix tissue.

A summary of all the 16 patients imaged is displayed in Figure 3.12. A region of interest has been selected to derive the depolarization and retardance information. The data has been color-coded in reference with Table 3.1 to aid in understanding of the polarimetric behavior compared to the clinical evaluation.

The 16 cervixes showed a trend of high (median >0.78) depolarization with the exception of patient 1, which had a polyp. The collagen structure in polyps differ from normal stroma, which was perceived by a lower depolarization value, as has been previously described by others¹⁴⁰. The retardance (measured in degrees) is visualized as high (red) and low (green), with a threshold of 25 degrees—approach was first introduced

by Reh binder *et al*¹⁴¹. The retardance values had an overall high trend (median > 29°), with the exception of patient 13 and 14.

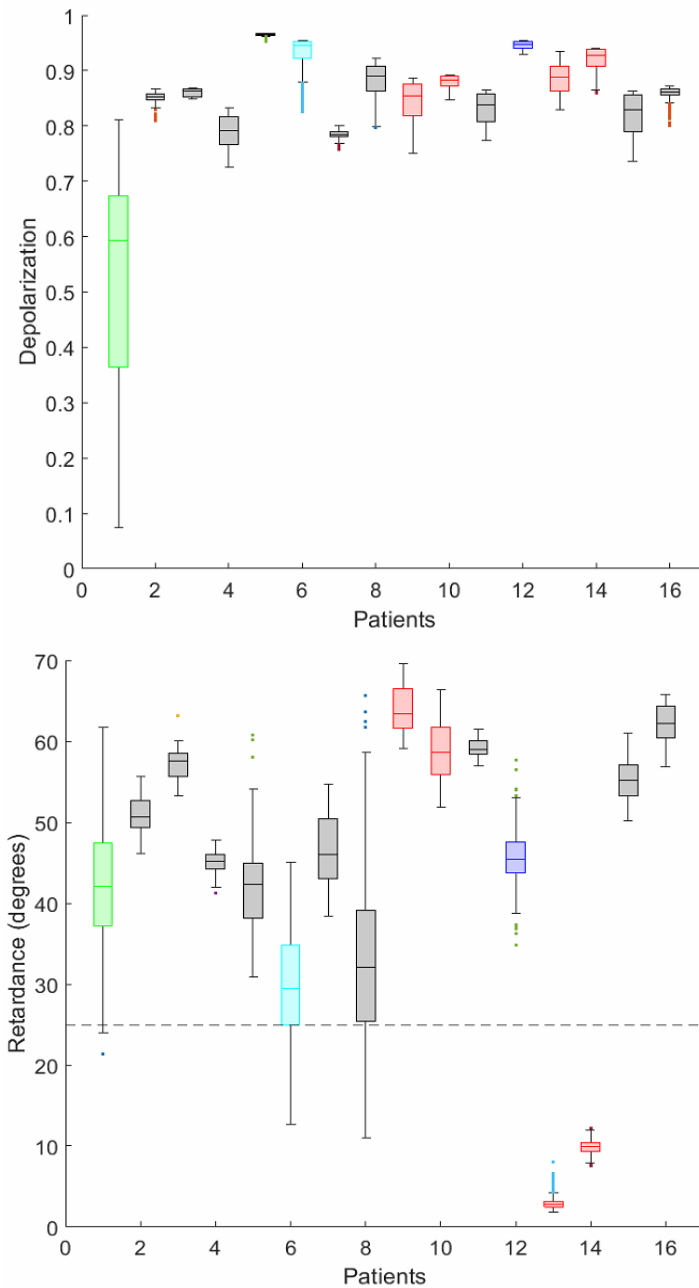


Figure 3.12. The depolarization (top) and retardance (bottom) of the 16 healthy subjects are summarized. The healthy cervixes show a pattern of high depolarization, with the lowest value (patient 1) being the polyp. The retardance shows a trend of high values as well, with only two cervixes having a median value below the 25 degree threshold.

3.4. Discussion

We have introduced a new snapshot Mueller matrix polarimeter capable of the fast acquisition of a full Mueller matrix. The imaging was performed in healthy cervixes, where there were no cases of dysplasia. The results of the Mueller matrix decomposition supports this clinical evaluation by showing a high depolarization trend with an average depolarization value of 0.85, where the lowest value, 0.52, is displayed by region of interest with a polyp. This is in accordance with previously reported work, where a polyp changes the collagenous structure and therefore the polarimetric response⁸⁸. The retardance shows an average of 44 degrees, which is within the range found in literature for healthy cervixes. Some non-uniformity of the retardance data can be due to the heterogeneity of the cervix as well as presence of artifacts such as specular reflection.

The ability of MMI to identify differences in the collagen's polarimetric response by detecting the distinct depolarization response between the polyp and other healthy cervixes shows how our portable system has the potential to be deployed for use in conjunction with routine cervical screening. The system is fully powered by a laptop computer and can be deployed in conditions where electrical outlets are not readily available. The cost of the system is also relatively low compared to current colposcopes (~\$2000), with a limiting factor being the cost of the Savart plates (~\$200). It is to be noted, however, that should the modality prove to be useful in sensing dysplastic lesions, higher production levels could be considered, lowering the overall production cost.

Further studies are necessary to truly determine the diagnostic power of this approach. One noted issue with the current system is the size of the illuminator and the ability of all illumination sources to reach the cervix without cut-off from the uterine walls. Six sets of

patient images, out of the 22 patients imaged, were discarded due to absence of data on account of poor illumination from one or more polarization states. In older patients and women that have experienced multiple pregnancies, this effect could be more severe limiting the use of our apparatus. To minimize this effect, we are currently redesigning the illuminator to allow for more direct access to the cervix. A second issue noted is the development of artifacts in the Fourier based analysis due to strong discontinuities in the inverse Fourier transform. When the regions of interest laid around those problematic regions, the second analysis (sliding reconstruction method) was utilized. Finally, another limiting factor was the loss of fringe contrast suffered in regions with high curvature. This, at times, limited the area that could be analyzed, and future work will focus on optimizing the imaging optics so that the entire cervix can be processed. Future studies will also be targeted toward testing the device's ability to detect malignancies in cervical tissues.

3.5. Conclusion

A feasibility study was conducted among healthy volunteers in Mysore, India. The results showed accordance with current literature about the depolarization and retardance behavior of healthy cervixes^{13,88,129,141}. Due to the dependence spatial interference pattern of the current methodology, there are limitations on the deployment and data analysis, as well as the limitation of non-real-time feedback. Recent advancement in polarization technology may lead to new direction of this research. Particularly, new cameras with integrated polarization capability (4-Directional Wire Grid Polarizer Array such as the Sony's IMX250MZR CMOS chip) may allow for fast acquisition of four linear states (Horizontal, Vertical, 45 degrees polarization and -45 degrees polarization). This technology would allow at maximum the creation of a reduced Mueller matrix (i.e. not 4x4), requiring other

data analysis techniques. In that regard, the proposed Savart method is still seen as superior as it offers the capability of capturing a full Mueller matrix.

In conclusion, we have developed a portable Mueller matrix imaging system that can be deployed in the low resource setting for cervical imaging. We believe that this type of imagery could improve the cervical screening assessment in the low resource setting beyond the current procedures.

CHAPTER 4 : Introduction of a 3 x 4 Mueller matrix decomposition method

4.1. Introduction

A 4 x 4 Mueller matrix describes the polarization transfer function^{1,73} of any medium using 16 parameters where the medium's polarization properties are encoded^{13,142}. Several methods have been proposed to experimentally measure a Mueller matrix⁸³ of different media. Recently, polarization sensitive cameras that integrate 4-Directional wire-grid polarizers within the sensitive area have been introduced^{143,144}. These snapshot systems can speed the acquisition process of reduced 3 x 4 Mueller matrix polarimetry by acquiring four different linear states of polarization (0°, 45°, 90°, 135° with respect to a reference plane) simultaneously. Studies aimed at understanding the accuracy and limitations of these cameras have been published^{143,145,146,147,148}. The polarization sensitive cameras have been used in applications ranging from navigation^{149,150} to biological media analysis. For example, the camera has been successfully used to observe and analyze polarimetric changes of dehydrated bovine tissues¹⁴⁴ and they have been integrated into rigid endoscopes¹⁵¹.

Mueller Matrix decomposition is used to obtain a better understanding of a material properties. There are various established 4 × 4 Mueller matrix decomposition methods to extract the parameters of depolarization, retardation and diattenuation from a full Mueller matrix.

The polar decomposition or Lu-Chipman (LC) decomposition⁷⁶ defines the Mueller matrix as a product of three matrices: a depolarizer (M_{Δ}), a retarder (M_R) and a diattenuation (M_D) matrix.

$$[4.1] \quad M = M_{\Delta} M_R M_D$$

The order of decomposition affects the result due to the non-commuting properties of matrix multiplication¹⁵², therefore other sequential matrix decompositions have been suggested. There has been introduced a reverse decomposition⁷⁷

$$[4.2] \quad M = M_D M_R M_{\Delta r}$$

Where $M_{\Delta r}$ describes a depolarizer with diattenuation (in contrast with the M_{Δ} parameter in the LC decomposition being a depolarizer with polarizance).

Ossikovski proposed the symmetric decomposition⁷⁸, that introduces the idea that the depolarizer matrix could be placed “in the middle” of retarder and diattenuation matrices

$$[4.3] \quad M = M_{D2} M_{R2} M_{\Delta d} M_{R1} M_{D1},$$

where M_{D1} and M_{D2} are two diattenuator matrices, M_{R1} and M_{R2} are two retarder matrices and $M_{\Delta d}$ is the pure depolarizer matrix.

This decomposition is particularly relevant for a backscattering configuration where the polarimetric effects (diattenuation and retardance) will occur in the forward direction of light propagation as well as in the backward path¹⁵³.

Moreover, there is also a differential (D) decomposition^{79,80} where the three polarimetric properties are considered to be occurring simultaneously and therefore can all be represented in one single differential matrix.

$$[4.4] \quad m = (dM_z/dz)M_z^{-1}$$

In response to the advent of polarization sensitive camera a reduced 3 x 3 Mueller matrix decomposition has been introduced^{81,154}. When the measurement configuration allows for only linear states to be generated and analyzed, only 9 coefficients of the upper left 3 x 3 submatrix of a full Mueller matrix can be acquired. This 3 x 3 Mueller submatrix decomposition follows a similar procedure as the LC decomposition of a full 4 x 4 Mueller matrix making the assumption that the depolarization of the linearly polarized light is isotropic, i.e. it does not depend on the incident linear polarization vector orientation⁸¹. This decomposition has been used in the polarimetric studies of samples, such as aqueous suspension of polystyrene microspheres and *ex vivo* rat abdomen, although the quantitative disparities between the 3 x 3 and 4 x 4 decompositions have been reported⁸².

In this paper we introduce the use of a polarization camera as a (standalone) polarization state analyzer (PSA) along with a four-state polarization state generator (PSG), for the measurements of a reduced 3 x 4 Mueller matrix and a new decomposition algorithm of this reduced 3 x 4 matrix with the aim of improving accuracy of the latter decomposition and its validation by the 4 x 4 decomposition results.

4.2. Methods

In the symmetric decomposition of a Mueller matrix (Equation 4.3) M_{D1} and M_{D2} are the Mueller matrices of the entrance and exit diattenuators, M_{R1} and M_{R2} are the Mueller matrices entrance and exit retarders, respectively, and M_{Δ} is the diagonal matrix of a canonical depolarizer.

M_{Δ} is defined as

$$[4.5] \quad M_{\Delta} = \begin{bmatrix} 1 & 0 & 0 & 0 \\ 0 & d_1 & 0 & 0 \\ 0 & 0 & d_2 & 0 \\ 0 & 0 & 0 & d_3 \end{bmatrix}$$

with a depolarization power Δ that is defined as,

$$[4.6] \quad \Delta = 1 - \frac{|d_1| + |d_2| + |d_3|}{3},$$

where d_1 and d_2 are the depolarization coefficients for the linear states (horizontal/vertical and 45/135, respectively) and d_3 is the depolarization coefficient for the circular states.

The Δ parameter ranges from 0 to 1, where $\Delta = 0$ is for a nondepolarizing sample.

In close to normal reflection, the following assumptions hold: $M_{D1} \approx M_{D2} \approx I$, where I is the identity matrix.

This assumption is legitimate whenever the surface contribution to diattenuation dominates compared to the volume contribution (these are the first surface in reflection or both surfaces in transmission), since Fresnel reflection and transmission coefficients coincide for both s and p polarizations at normal incidence ($r_p \approx r_s$; $t_p \approx t_s$). Its validity has been demonstrated by Vizet and Ossikovski¹⁵³, in reflection at normal incidence, utilizing optical components such as waveplates as well as biological specimens. Furthermore, the assumption $d_1 \approx d_2$ follows from rotational invariance at normal incidence, whereas $M_{R1} \approx M_{R2} = M_R$ results from the (approximate) equivalence of forward/backward propagation (in reflection; M_{R2} being replaced by its transpose) or from the invariance with respect to light reversal (in transmission) still at normal incidence.

Furthermore, $d_1 \approx d_2$ and $M_{R1} \approx M_{R2} = M_R$ ¹⁵³,

where M_R is the Mueller matrix of a linear retarder with retardance δ and azimuth of the optical axis of linear birefringent medium θ , Equation 4.7a. Unlike the LC and differential decompositions, in the 3X4 decomposition the retarder M_R is explicitly assumed to be linear ($M_R = M_{RL}$). This assumption is justified for an essentially homogeneous medium (effectively behaving either as an optically thick single layer or a semi-infinite substrate) lacking (or, more generally, having negligible) optical activity. Conversely, the actual 3X4 decomposition cannot be applied to multilayer structures since those generally behave as elliptical retarders.

$$[4.7a] \quad M_R = \begin{bmatrix} 1 & 0^T \\ 0 & m_R \end{bmatrix}$$

$$[4.7b] \quad m_R = \begin{bmatrix} m_{11} & m_{12} & m_{13} \\ m_{12} & m_{22} & m_{23} \\ -m_{13} & -m_{23} & m_{33} \end{bmatrix}$$

Therefore, a diattenuation-free Mueller matrix M can describe the experimental configuration:

$$[4.8] \quad M \approx M_R M_{\Delta d} M_R,$$

that is dependent on four parameters: two depolarization coefficients, d_1 and d_3 , retardance δ , and azimuth θ .

Taking into account five of the twelve effectively measured Mueller matrix elements from the first three rows, the following set of equations can be written:

$$[4.9a] \quad M_{22} = d_1 m_{11}^2 + d_2 m_{12}^2 - d_3 m_{13}^2$$

$$[4.9b] \quad M_{23} = (d_1 m_{11} + d_2 m_{22}) m_{12} - d_3 m_{13} m_{23}$$

$$[4.9c] \quad M_{24} = d_1 m_{11} m_{13} + d_2 m_{12} m_{23} + d_3 m_{13} m_{33}$$

$$[4.9d] \quad M_{33} = d_1 m_{12}^2 + d_2 m_{22}^2 - d_3 m_{23}^2$$

$$[4.9e] \quad M_{34} = d_1 m_{12} m_{13} + d_2 m_{22} m_{23} + d_3 m_{23} m_{33}$$

where m_{ij} ($i, j = 1, 2, 3$) are the elements of matrix m_R from Equation 4.8.

Equations (4.9) represent an overdetermined set of five equations to solve for four unknown parameters: d_1, d_3, δ and θ .

These four parameters are obtained by solving equations 4.9(a-e) with a Nelder-Mead Simplex minimization method implemented in MATLAB (MathWorks, Natick, MA).

4.2.1. Validation

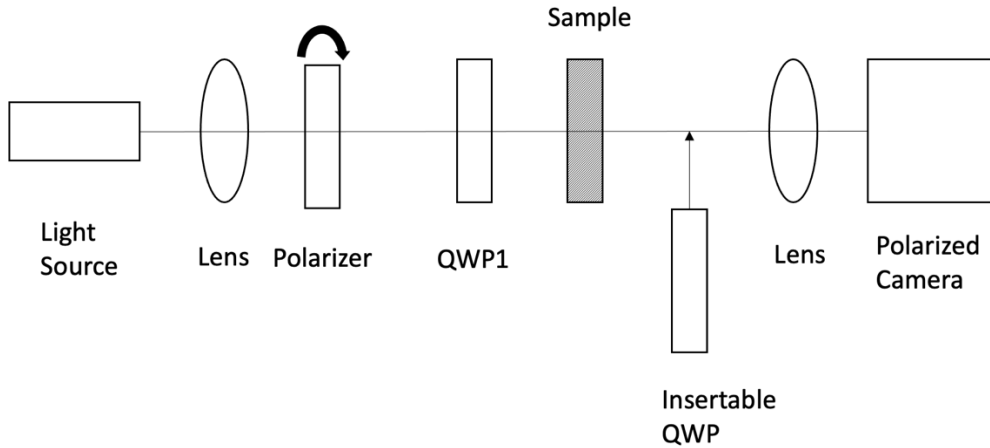


Figure 4.1. Experimental setup consisting of a light source with collimating lens, a PSG consisting of a polarizer on a rotational stage, a quarter-wave plate (QWP1), and PSA utilizing the polarized camera with lens and a quarter wave plate (QWP) that is inserted only when measuring the 4 x 4 Mueller Matrix.

This approach was validated experimentally with the setup shown in Figure 4.1. The reduced 3 x 4 Mueller matrix polarimeter consists of a 625 nm LED (M625L3, Thorlabs Inc., Newton, NJ) source coupled with a linear polarizer (LPVISC100, Thorlabs Inc.,

Newton, NJ) housed in a rotational stage with a PSG of horizontal, vertical, 45 degrees and the addition of a quarter wave plate (QWP) (AQWP05M-580, Thorlabs Inc., Newton, NJ) to create right circularly polarized light. The PSA consists of a polarized camera (CS505MUP, Thorlabs Inc., Newton, NJ). A QWP (AQWP05M-580, Thorlabs Inc., Newton, NJ) could be inserted into the detection arm in order to analyze circularly polarized light component and create a full 4 x 4 Mueller matrix. This setup was used to image a number of samples, such as polarizers, QWPs and silicone phantoms at various orientations. Moreover, a 5 micrometer thick section of human skin model mounted on a glass slide with parallel collagen fiber alignment along the dermis¹⁵⁵ was also imaged by adding a 2X objective lens (Mitutoyo Plan Apo, Mitutoyo America Crop, IL) to the PSA. The system was calibrated as previously reported by Saytashev *et al.*¹⁵⁶, yielding an error of less than 3% in the calculation of an identity Mueller matrix of air. The condition number for our system was equal to 4.5.

4.3. Results and Discussion

Error analysis

The values of the elements of Mueller matrix are dependent on the input variables: d_1 , δ , θ and d_3 , (as seen in Equation 4.9a-e). Understanding the intrinsic error of the minimization algorithm used for the decomposition of 3 x 4 reduced Mueller matrix (as it pertains to these variables) is useful to determine the limitations of using such approach. In order to conduct an error analysis, three input variables, d_1 , δ and, θ (d_3 was kept constant), were used to calculate a Mueller matrix MM_{pre} (Equation 4.8) within a range of values for each variable (i.e. δ and θ varied from 0 to 180 degrees and d_1 varied from 0 to 1). The five

elements of calculated Mueller matrix were then used for the solution of Equations (4.9) by minimization. The same three variables were obtained and used to calculate a new Mueller matrix MM_{post} (Equation 4.8). The error of the minimization algorithm was estimated by calculating the normalized root mean square error (nRMSE) of the difference between the two Mueller matrices (MM_{pre} and MM_{post}). The nRMSE values vary between 0 and 1, where 0 yields no difference between the values of two Mueller matrices MM_{pre} and MM_{post} . Figure 4.2 shows a sample slice of the error encountered upon minimization for all θ and δ with d_1 fixed at 0.7 (left panel) and a closer look at selected cross-sections from the overall volume of values (right panel) for better visualization of the error. There is a peak error value of 18% for high values of θ (>100 degrees) and d_1 (>0.7) and arbitrary δ values, although the mean error value for the entire volume was 2.5%.

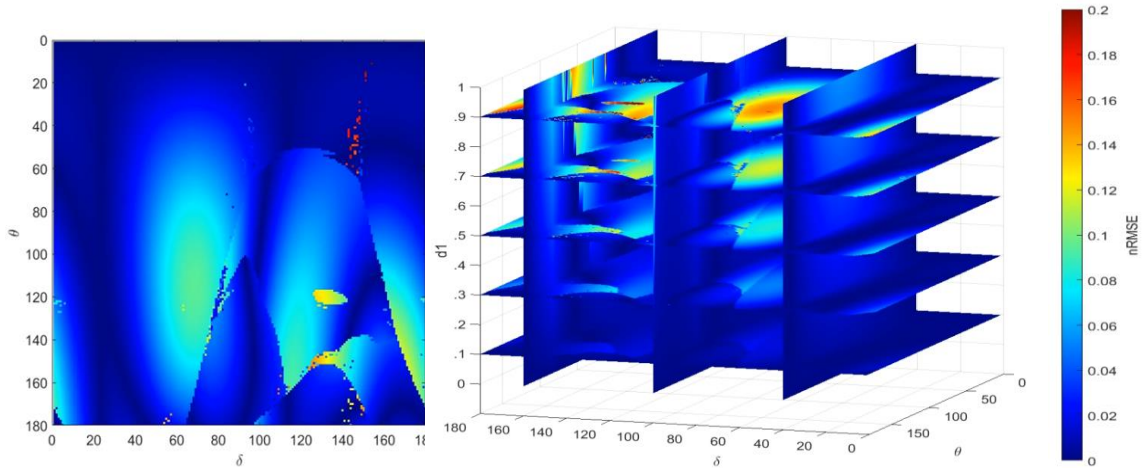


Figure 4.2. Error analysis of the minimization algorithm used for the decomposition of a reduced 3×4 Mueller matrix. The left figure shows a slice of error values for all θ and δ with d_1 fixed at 0.7. The right figure shows the error contour plots in selected volume sections.

Decomposition implementation

We first aimed to compare the different decompositions using an experimentally recorded Mueller matrix M (Equation 4.10a-d) introduced by Ghosh *et al.*¹ with a known depolarization, retardance, diattenuation and θ values. The polar LC decomposition was applied first to the 4 x 4 matrix M (which takes into account all three polarization parameters), then the decomposition of the reduced 3 x 4 matrix was applied using the depolarization and retardance matrix (since our assumption is that M_D is unity), as seen in Equation 4.8. For the comparison, the D decomposition of the complete 4 x 4 matrix M was also tested.

The values of the depolarization, the retardance and the azimuth of the optical axis calculated using matrix M and the above-mentioned decompositions are listed in the Tab.1.

$$[4.10a] \quad M = \begin{bmatrix} 1 & -0.0229 & 0.0027 & 0.0058 \\ -0.0186 & 0.9956 & -0.0361 & 0.0318 \\ -0.0129 & 0.0392 & 0.2207 & -0.9656 \\ 0.0014 & 0.0280 & 0.9706 & 0.2231 \end{bmatrix}$$

$$[4.10b] \quad M_{\Delta} = \begin{bmatrix} 1 & 0 & 0 & 0 \\ 0.0041 & 0.9969 & 0 & 0 \\ -0.0070 & 0 & 0.9915 & 0 \\ -0.0019 & 0 & 0 & 0.9966 \end{bmatrix}$$

$$[4.10c] \quad M_R = \begin{bmatrix} 1 & 0 & 0 & 0 \\ 0 & 0.9988 & -0.0362 & 0.0281 \\ 0 & 0.0393 & 0.2207 & -0.9741 \\ 0 & 0.0320 & 0.9742 & 0.2239 \end{bmatrix}$$

$$[4.10d] \quad M_D = \begin{bmatrix} 1 & -0.0229 & 0.0027 & 0.0058 \\ -0.0229 & 1.000 & -0.000 & -0.0001 \\ 0.0027 & 0.000 & 0.9997 & 0.000 \\ 0.0058 & -0.0001 & 0.0000 & 0.9997 \end{bmatrix}$$

Table 4.1 The decomposition parameters (Δ , δ , θ) for the matrix M (Equation 4.10a). (First column) values from Ghosh *et al.*¹, (second column) values from the LC decomposition,

(third column) D decomposition and (fourth column) decomposition of the reduced 3 x 4 matrix.

<i>Parameters</i>	Ghosh <i>et al.</i> 4 x 4 LC		4 x 4 D 3 x 4	
	<i>Estimated values</i>			
Δ	0.005	0.005	0.005	0.005
$\delta(\text{rad})$	1.346	1.345	1.346	1.346
$\theta(\text{deg})$	89.05	89.94	89.98	89.98

The results of the different decompositions of a complete 4 x 4 matrix M and its reduced 3 x 4 version yielded a similar answer to what has been previously reported^{1,157}. The decomposition of a reduced 3 x 4 Mueller matrix matches its 4 x 4 counterparts for this low-depolarizing medium, noting the only difference in the 4x4 D is the orientation being equal to $(|\theta - 90|)$.

To further investigate the proposed decomposition of a reduced 3 x 4 Mueller matrix, a QWP with its axis oriented at three different angles: -20, -30 and -60 degrees—assuming the frame of reference to be the benchtop plane—was imaged. The QWP is a retarding element with theoretically neither depolarization nor diattenuation present, therefore we can focus on the new decomposition method’s response to retardance and azimuth of orientation.

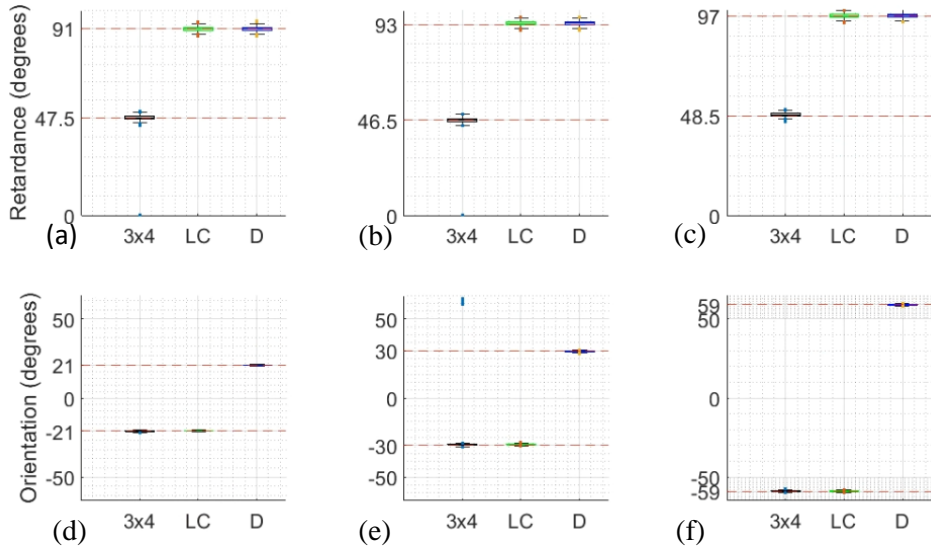


Figure 4.3. Comparison between the decomposition of a reduced 3 x 4 Mueller matrix (3 x 4), LC and D decompositions of 4 x 4 Mueller matrix of the QWPs oriented at (a,d) -20 degrees, (b,e) -30 degrees and (c,f) -60 degrees with respect to the polarization axis of the incident beam. The red lines delineate the median value of the data set.

The parameters calculated with all decompositions of the Mueller matrix of the QWP measured at different azimuth angles can be observed in Figure 4.3, where the complete 4 x 4 experimentally recorded Mueller matrix was used to calculate the LC and D decompositions and the first three rows of this Mueller matrix were used to calculate the 3 x 4 decomposition. There is a wide agreement within the three decomposition methods on the orientation angle values for all measurements, showing the QWP positioned at -20 degrees (#a,d), -30 degrees (#b,e) and -60 degrees (#c,f). The retardance of QWP calculated with the reduced 3 x 4 Mueller matrix decomposition appears as half of the value compared to the values calculated with its 4 x 4 counterparts at different QWP orientations. This discrepancy is likely due to the absence of depolarization, modifying our definition of the 3 x 4 matrix decomposition (Equation 4.8) to equal $M \approx M_R^2$. Moreover, the lack of the

fourth row in the reduced 3 x 4 Mueller matrix leads to a negative retardance value in some cases, which causes the angle to be shifted by 90 degrees. A correction for this is necessary, entailing of modifying the orientation angle by 90° each time a negative retardance is obtained (correction for this was already applied in Figure 4.3). The QWP orientation angle agreed well for all positions, matching the 3 x 4 decomposition with the 4 x 4 LC decomposition in every measurement, as well as the orientation angle value calculated with the D decomposition but with a differing sign.

Looking further into comparing the decompositions experimentally, an extruded silicone phantom consisting of a silicone strip with visible striations along the direction of extrusion, oriented at three different positions was imaged with our setup. A low depolarization and uniform retardance is expected due to its natural semitransparent characteristics. The reduced 3 x 4 Mueller matrix of the silicone phantom oriented at -70 degrees can be observed in Figure 4.4, demonstrating the structured striations and weakly depolarizing nature of the sample.

The results of the decomposition of the Mueller matrix of the aforementioned phantom with different algorithms can be seen in Figure 4.5, where we can qualitatively see the similar values of depolarization, the values of the retardance calculated with 3 x 4 decomposition close to half of the retardance values calculated with the decompositions of the complete 4 x 4 Mueller matrix and the agreement on the orientation angle for all decompositions. The white box in the Figure 4.5 indicates a 30x30 pixel region of interest (ROI) where the sample is assumed to be homogeneous to fairly compare the three decomposition methods.

To more quantitatively ascertain the decomposition methods, the calculated depolarization, retardance and orientation angle values for the silicone phantom (within the selected ROI) oriented at -70, -60 and 80 degrees are shown in Figure 4.6.

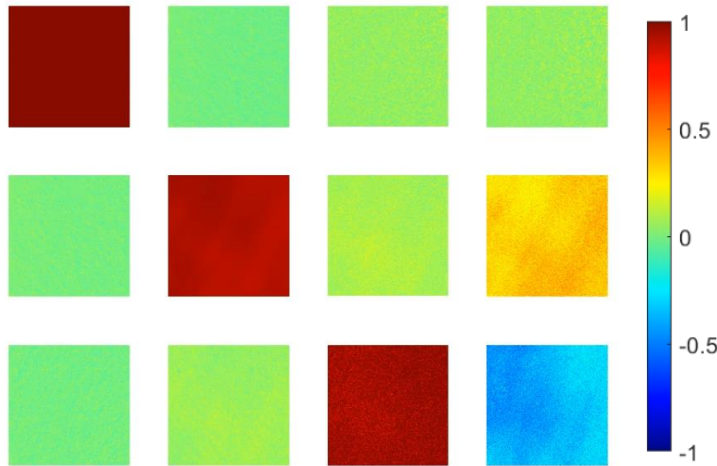


Figure 4.4. Reduced 3 x 4 Mueller matrix of a silicone sample oriented at -70 degrees, showing the striation direction. The weakly depolarizing nature of the sample is confirmed by the dominance of the diagonal values that are close to one.

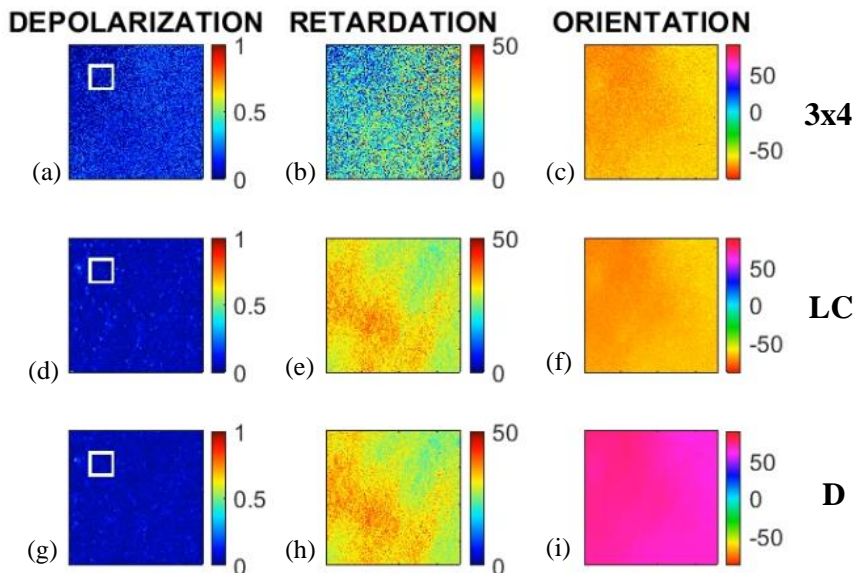


Figure 4.5. The images of (a,d,g) the depolarization, (b,e,h) the retardance and (c,f,i) the angle of orientation calculated from Mueller matrix of a silicone phantom oriented at -70

degrees using the three decomposition methods: (first row) 3 x 4 decomposition, (second row) LC decomposition, and (third row) D decomposition. The white box indicates a region of interest at which the sample is assumed to be homogeneous (for comparison purposes).

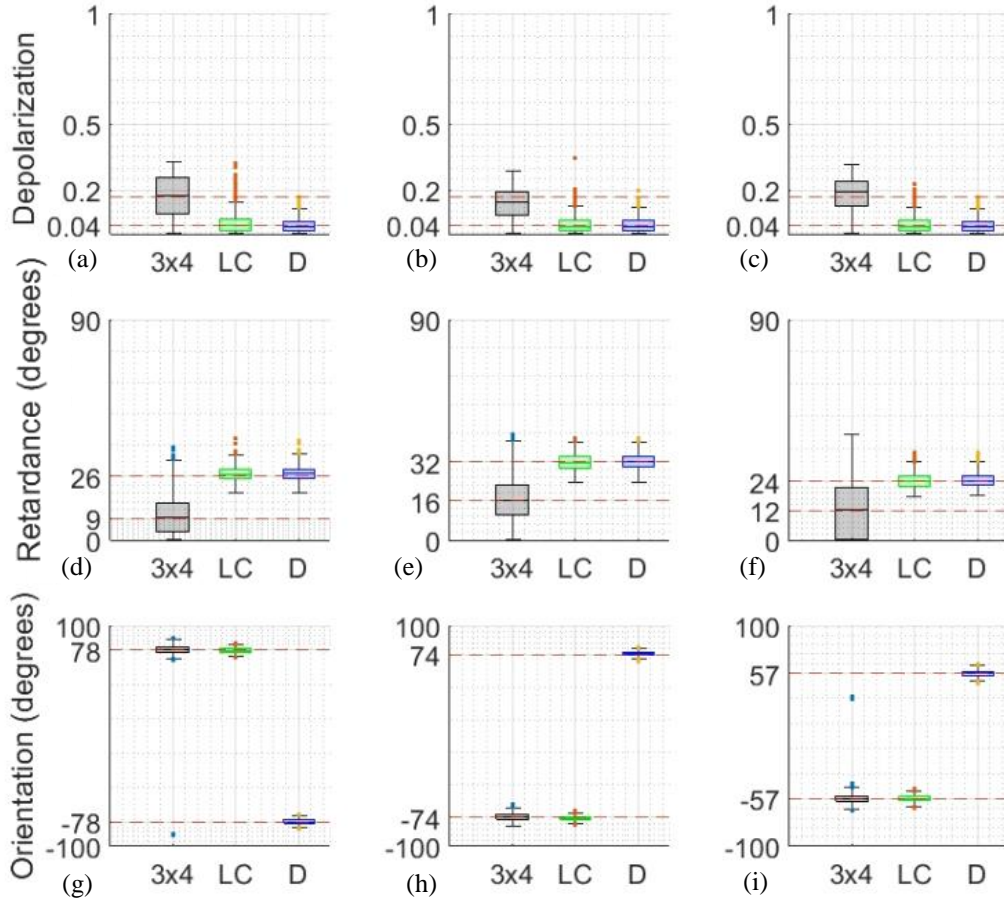


Figure 4.6. Comparison between the reduced 3 x 4 Mueller matrix decomposition, LC and D decompositions of the complete 4 x 4 Muller matrix of silicone phantom oriented at (a,d,g) 80 degrees, (b,e,h) 70 degrees and (c,f,i) 60 degrees with respect to the reference plan of the incident beam. The red lines delineate the median values within the ROI.

At all measurement configurations the silicone phantom shows a similar distribution of depolarization values within the selected ROI, ranging from 0 to 0.35, with a median value around 0.2 calculated with the 3 x 4 decomposition (Figure 4.6 a-c), although notably different from the distributions of depolarization values calculated with both LC and D

decompositions of the complete 4 x 4 Mueller matrix (median value is 0.04). This could be due to the difference in the depolarization definitions for the different calculations. The distribution of the retardance values calculated with the reduced 3 x 4 Mueller matrix decomposition (Figure 4.6d) offers a wider set of data points than the 4 x 4 methods (Figure 4.6e-f), with the median value falling close to the half-retardance mark of the calculated retardance value for the latter. This phenomenon is due to the low depolarization of the silicon phantom, similarly to that of the quarter-wave plate in the previous experiment. As for the orientation angle (Figure 4.6g-i), we notice a similitude between the distributions of the angle values (and range of angles perceived) for the reduced 3 x 4 Mueller matrix decomposition and the LC decomposition. The D decomposition shows an opposite sign of angle in all cases. This difference in sign for the D decomposition is due its definition and the use of different matrix elements (compared to the LC) used to calculate the orientation.

Lastly, the results of different decompositions of the Mueller matrix of the section of human skin model mounted on the glass slide can be seen in Figure 4.7 and summarized in the boxplots in Figure 4.8. This sample is also weakly depolarizing (due to its small thickness of 5 μm) and shows a similar pattern as the previous samples for the retardance values, where the reduced 3 x 4 Mueller matrix decomposition values are found to be about half of the values calculated with LC and D decompositions of the complete 4 x 4 Mueller matrix. The orientation angle of the sample is in agreement for the 3 x 4 and the LC decompositions, although it appears to be the complement angle ($|\theta - 90|$) for the D decomposition.

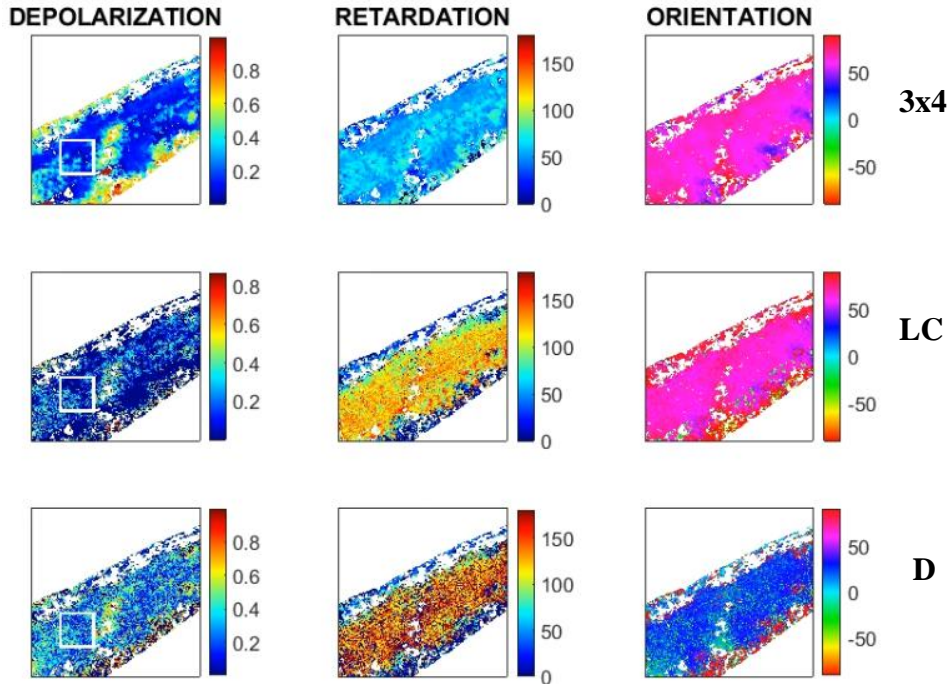


Figure 4.7. The images of the depolarization, the retardance and the orientation angle of human skin model section mounted on the glass slide with focus on the dermis. The parameters calculated with three different decompositions: 3 x 4, LC and D are shown from top to bottom, respectively. The saturated and background pixels have been rendered in white. The white box indicates a region of interest in the dermis at which the sample is assumed to be homogeneous.

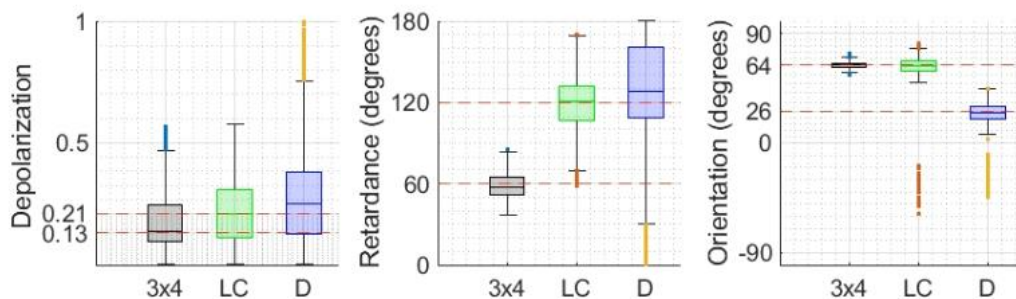


Figure 4.8. Comparison of the results of three decompositions of the Mueller matrix of human skin model section, where we can observe the similitude of the 3 x 4 decomposition with the 4 x 4 LC decomposition as well as the D. Red lines indicate median value of the data set.

Similar distributions of the depolarization values within the selected ROI are calculated with all three decompositions. The values of retardance calculated with the reduced 3 x 4

Mueller matrix decomposition are found to be about half of the values calculated with LC and D decompositions of the complete 4 x 4 Mueller matrix as for the silicon phantom. The same trends are observed for the distributions of the orientation angle calculated with three different decompositions as in case of the silicon phantom.

4.4. Conclusion

This paper introduces a new method of decomposition for a reduced 3 x 4 Mueller matrix. This decomposition has shown to be capable of calculating the correct polarimetric parameters (depolarization, retardance and orientation angle) when compared to the established decomposition methods of the complete 4 x 4 Mueller matrix. The decomposition of the previously reported Mueller matrix (Equation 4.10a) for the 4x4 decompositions and the diattenuation free matrix (only using Equation 4.10b-c) yielded similar values to what were reported by the authors for all polarimetric parameters. For the experimental cases shown, the depolarization values did not yield similar values, likely due to the difference in depolarization factor definition for all three decompositions methods. The retardance values calculated with the new decomposition were approximately equal to half the retardance values calculated with the LC and D decompositions of the complete 4 x 4 Mueller matrix for all the cases, which is due to the definition of the 3x4 decomposition (Equation 4.8). The orientation angle, values calculated with the new decomposition were aligned well with the values calculated with the decompositions of the complete 4 x 4 Muller matrix (especially with the LC decomposition) in all samples. Discrepancies in the orientation angle values shown for the D decomposition are due to the matrix elements used to calculate the orientation angle value. Taking into account inherent errors due to the minimization algorithm used, further testing with a wider array of samples with differing

polarization properties needs to be conducted to understand what limitations these errors could pose. Moreover, we plan to explore the behavior of the new decomposition of the reduced 3 x 4 Mueller matrix for more depolarizing samples, since this is a property exhibited by biological tissues.

This new decomposition method of the reduces 3 x 4 Mueller matrix has a particular value due to the technological advances giving rise to polarization cameras, as it will help to omit the need for circular polarization analysis components in the PSA and therefore to simplify the experimental setup needed for the full characterization of sample using Mueller matrix polarimetry. This simplification could provide a fast and robust solution to current uses of polarimetry, especially in a clinical setting where time and simplicity poses an issue.

CHAPTER 5 : TESTING THE 3 X 4 MUELLER MATRIX DECOMPOSITION IN BIOLOGICAL TISSUE

5.1. Introduction

Cervical cancer is the fourth most common cancer in women worldwide, with an estimated half a million new cases and 260,000 deaths each year.¹⁵⁸ It is estimated 1.4 million women worldwide are living with cervical cancer, and two to five times more - up to 7 million - may have precancerous conditions that should be identified and treated¹¹. Due to the slow disease progression of invasive cervical cancer, it is a perfect candidate for early screening and treatment. Existing vaccinations against human papilloma virus (HPV) are expensive and do not target all 15 high risk HPV types, ergo the imperative need for screening⁴⁶. The current recommended proceeding for cervical testing by the World Health Organization (WHO) includes cytology (Pap test) every 3 years for women 21-65 years old and HPV test every 5 years for women 30-65 years old. If the aforementioned Pap test is abnormal or the HPV test positive, then a colposcopy is performed, followed by biopsy and histological confirmation. Watson *et al.* reported a decline in Pap testing among women of the age group 21-65 between 2010 and 2015, leaving 14 million women without screening¹⁵⁹. Moreover, MacLaughlin *et al.* showed a continuing decline in testing since 2015 among women between the ages of 21-29, with a population screening rate of 62.6% in 2005 to 47.3% in 2016¹⁶⁰. The gynecological proceedings requires women to lay flat on their backs while placing their legs on stirrups to create a 45° angle. This is often accompanied by anxiety, pain, discomfort and vulnerability, which makes the women less likely to follow testing guidelines.^{161,162,163} Seehusen *et al.* reported the use of stirrups induced higher vulnerability and pain, compared to women that were only required to lay

flat.¹⁶² Moreover, gynecological screening is seen as taboo in some cultures, increasing the health disparity and cervical cancer screening for many ethnic groups^{161,164,165,166,167}. Previous studies have shown that self-insertion of a speculum for examination is acceptable to most women with the outcome of preferring self-insertion in future testing.^{51,168,169} It has been mentioned previously the ideal technique for diagnosis of cervical dysplasia would cause minor discomfort, rapidly measure regions of interest and provide real time results¹⁷⁰. There are existing technologies that involve an insertable to probe cervical tissue such as the high resolution microendoscope (HRME) and the POCkeT colposcope^{6,171}. However, the HRME has a field of view (FOV) of 720 μm (being unable to visualize the whole cervix) and involves the application of a solution in order to reveal changes. Also, the POCkeT colposcope is dependent on a physician's feedback^{172,173}, which is highly user dependent¹⁷⁴. In a meta-analysis, it was found that the sensitivity and specificity for colposcopy-based punch biopsies to detect CIN1 lesions were of 91% and 24% and 80% and 63% for CIN2 lesions, respectively¹⁷⁴. Colposcopy alone is strongly operator-dependent, therefore there is a need for a more quantitative solution. Further analysis of existing low-cost screening devices can be found in Chapter 2.

Understanding the current limitations of available techniques and devices, an optical device that can provide quantitative information about the health of the cervix (increasing the sensitivity and specificity for pre-cancerous lesion detection) and could eventually be self-administered (increasing comfort and reducing anxiety) would be beneficial to use as part of the cervical cancer screening process. Our group has developed a Portable Preterm Imaging system (PPRIM) to assess cervical remodeling.

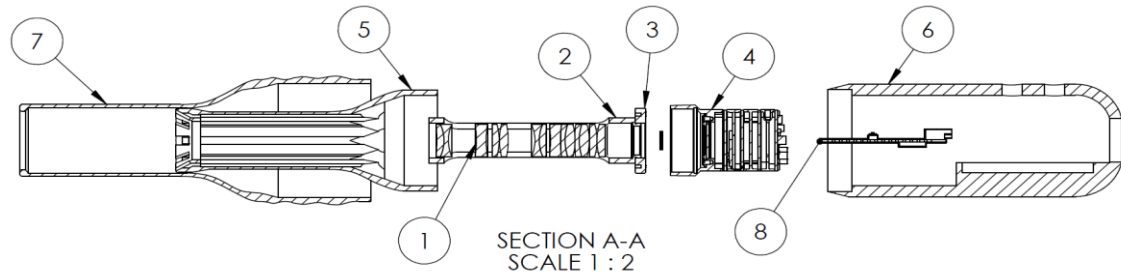
We tested our 3 x 4 Mueller matrix decomposition method, previously introduced (Chapter 4), with the PPRIM system. Previous testing of the 3 x 4 decomposition included imaging samples such as uniformly striated silicone and a human skin model. This chapter focuses on the use of this decomposition method on highly depolarizing media, such as *ex vivo* and *in vivo* tissues.

5.2. Methods

In order to test 3 x 4 decomposition in biological tissue, a device capable of *in vivo* imaging of the cervix is used.

5.2.1. Specifications

The device is composed of a polarization state generator (PSG) and a polarization state analyzer (PSA). The PSG consists of eight light emitting diodes (LEDs) housing a combination of polarizers and quarter waveplates (QWPs) with four different states of polarization: linear horizontally polarized light, linear vertically polarized light, linear 45 degree polarized light and right circularly polarized light. The PSA consists of a polarized camera (with four linear polarizers mounted on the microsensor) and telephoto lens. Further specifics can be found elsewhere⁹. The resolution of the device is 6.35 lp/mm, taken with a United States Air Force (USAF) target. The field of view is 25 mm. The PPRIM system can be seen in Figure 5.1 from Boonya-ananta et al. ⁹.



ITEM NO.	PART NUMBER	DESCRIPTION	QUANTITY
1	-	Optical arrangement assembly (Figure 1/Table 1)	1
2	SM05L30C	Thorlabs Lens Tube	1
3	SM05A2	Thorlabs Flange adaptor SM05 to C-Mount	1
4	PHX050S-P/Q	Lucid Phoenix Polarized Camera	1
5	-	Front-end housing case	1
6	-	Back-end housing case	1
7	-	Sheath	1
8	A000005	Arduino Nano3	1

Figure 5.1 (Top left) Design assembly and (top right) exploded view. (Bottom) Exploded section in 2D along with description of full assembly itemized 1-8. [Reproduced from Boonya-ananta et al.⁹].

The device was designed to effectively obtain images of the cervix using a self-inserter, although the self-imaging aspect is outside the scope of the presented work. The self-inserter consists of a sheath, meant to have a similar function as a speculum, and the imager, where the lenses and camera are housed.

The image quality of the insertable imaged is first assessed using a cervical model created as a silicone gynecological training system for physicians to evaluate cervical cancer (ZOE Gynecologic light skin tone skills trainer, Gaumard Scientific, Miami, FL), as seen in Figure 5.2.

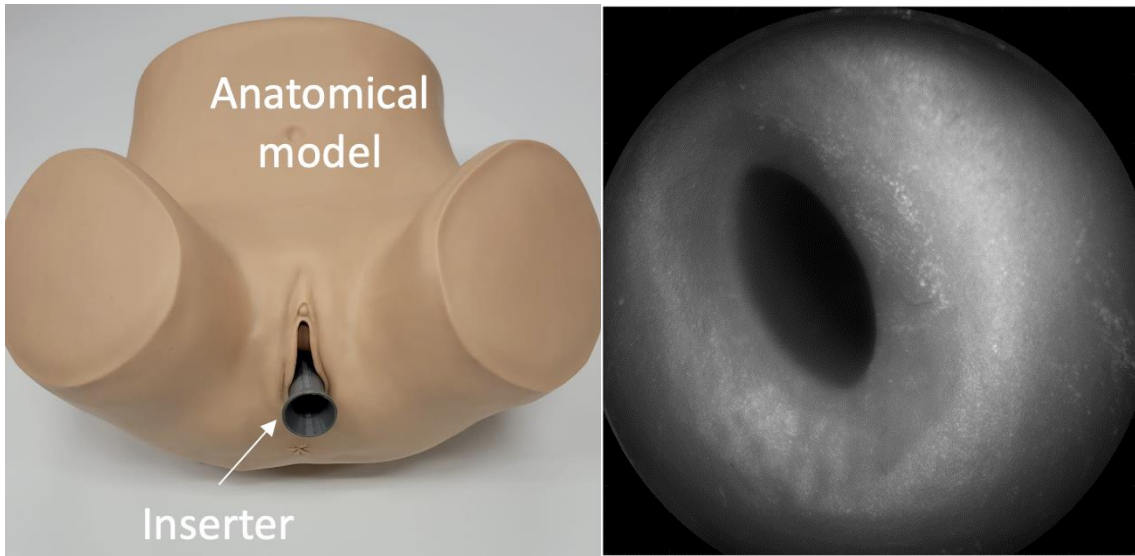


Figure 5.2 Gynecological training system used to evaluate image quality of the PPRIM.

5.2.2. Image analysis

The four generated polarization states and the three analyzed polarization states form a 3 x 4 Mueller matrix that can be decomposed using the 3 x 4 decomposition. This reduced decomposition assumes a negligible diattenuation and focuses on obtaining the depolarization, retardance and azimuth of the sample. The decomposition is defined as follows:

$$[5.1] \quad M \approx M_R M_{\Delta d} M_R,$$

Where Mueller matrix M is equal to the matrix multiplication of a pure depolarizer matrix, $M_{\Delta d}$, and two retarder matrices, M_R . The decomposition of the Mueller matrix solves for

four unknown values: the linear depolarization coefficient (d_1), the circular depolarization coefficient (d_2), the retardance (δ) and the azimuth (θ), which leads to the polarization parameters of depolarization, retardance and orientation that characterize the sample.

The decomposition has been previously shown to work using retarders, such as quarter wave plates, uniformly organized samples (such as silicone with parallel striations) and depolarizing samples (5 μm section of a human skin model).

5.2.3. *Ex vivo* testing

The device and decomposition are first tested on *ex vivo* chicken tendon, which due to the high collagen fiber alignment exhibits strong birefringence. Moreover, due to the biological nature of the tissue, there is a high level of scattering and therefore high depolarization. Due to these properties, this sample is often used for polarization system characterization and testing^{74,175}.

A second sample of *ex vivo* porcine cervix embedded in paraffin is also tested. The porcine cervix has circumferentially aligned collagen structure around the os, similar to a human cervix, therefore exhibiting similar polarization properties¹⁷⁵. The embedding process can be found elsewhere¹⁷⁵.

5.2.4. *In vivo* testing

The device was clinically tested under IRB protocol IRB-21-0173-AM01 approved by Florida International University. Eligibility criteria for imaging included: (1) age ≥ 18 years, (2) willing to undergo imaging, and (3) having the capacity to undergo informed consent process. The imaging process consisted of the participant lying flat on their back while bending their legs to create a 45 degrees angle, similar to the position during a

gynecological exam. The sheath is lubricated (using a water-based lubricant) and then inserted by the participant. Then, when the sheath is placed in position, the imager is inserted to fit the depth of the sheath, and 12 images are taken. These 12 images will be used to make the Mueller matrix.

5.3. Results

5.3.1. *Ex vivo* chicken tendon

Chicken tendon is often used for polarimetric imaging due to its highly ordered fibers. The fiber orientation can be seen in figure 5.3a, where the intensity image (M11) is shown. The decomposition can be appreciated in figure 5.3, where the depolarization and orientation of the *ex vivo* tissue are presented. The depolarization (Figure 5.3b) shows a median value of 0.89, as expected. Biological tissues are highly scattering and therefore exhibit high depolarization (close to one). The orientation of the tendon can be observed in Figure 5.3c by the azimuth angle. Chicken tendon (oriented at 55 degrees for this experiment) has a high fiber alignment, as the black bars defining the angle for a 10 pixel ratio display. The imaging outcome of the chicken tendon sample agrees with previously reported work¹⁷⁶. Chue-Sang *et al.*, showed similar outcomes in their polarimetric studies, where they showed the highly depolarizing nature of the tendon and the uniformity of fiber alignment upon decomposition^{89,127}. Moreover, chicken tendon sample being used as a common polarimetric validation metric has been previously reported⁷⁴.

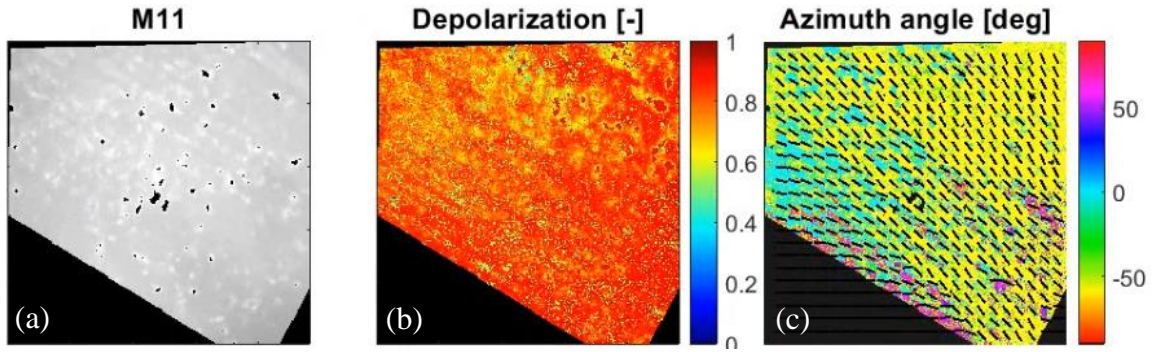


Figure 5.3 Chicken tendon sample showing (a) the intensity image, M11, (b) the depolarization and (c) the orientation, as shown by the azimuth angle. The black bars indicate the preferred alignment of the tissue within a 10 pixel range.

5.3.2. Paraffin porcine cervix

Another sample often used to validate and test polarimetric devices is the porcine cervix. The porcine cervix is similar to the human cervix and therefore has a high fiber alignment surrounding the os. Two porcine cervixes embedded in paraffin samples were imaged. This alignment can be visible using Mueller matrix polarimetry in both samples, as is shown Figures 5.4 and 5.5. Figure 5.4c and figure 5.5c show the cyclical nature of the fibers in the cervix, where the black bars represent the angle preference within a 10 pixel range. Moreover, the depolarization of the first porcine cervix sample (Figure 5.4b) has a median value of 0.77 and of the second sample a median of 0.85 (Figure 5.5b), as expected from a healthy biological sample, as seen in literature^{175,177}.

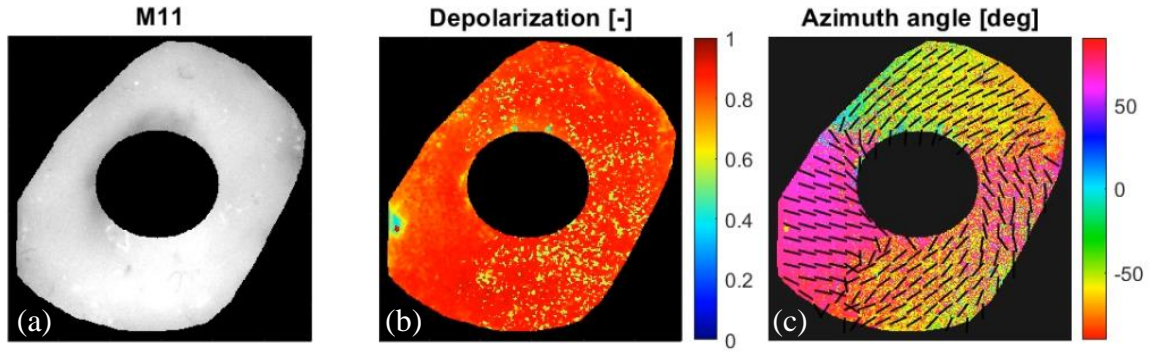


Figure 5.4 Porcine tendon embedded in paraffin sample one showing (a) the intensity image, M11, (b) the depolarization and (c) the orientation, as shown by the azimuth angle. The black bars indicate the preferred alignment of the tissue within a 10 pixel range.

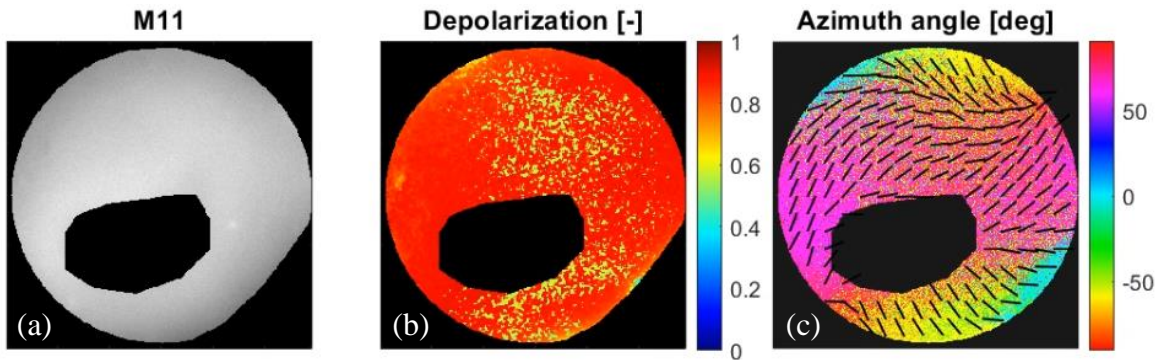


Figure 5.5 Porcine tendon embedded in paraffin sample two showing (a) the intensity image, M11, (b) the depolarization and (c) the orientation, as shown by the azimuth angle. The black bars indicate the preferred alignment of the tissue within a 10 pixel range.

5.3.3. *In vivo* human cervix

5.3.3.1 Insertion: patient feedback

Two subjects were recruited to test the PRIM in the clinical setting on *in vivo* human cervixes. A non-lubricated condom along with water-based lubricant was added to the inserter to aid in positioning the imager to collect the cervical images (Figure 5.6). The tip of the condom was cut in order to not interfere with the image quality (dashed line in Figure 5.6). The subjects lay flat with the knees making a 45 degrees angle during the imaging,

same position taken at annual cervical screening exams. The inserter was slid in the vaginal canal while being held by the handle, then the imager was inserted to the position where the cervix could be seen in focus. The live video provides feedback to the clinician to find the distance where the imager focuses.

Cervical images of the two subjects were successfully acquired. The two subjects found the PPRIM to be comfortable to use. The inserter with the condom and lubricant made it easy to slide into position and the imaging was overall an acceptable experience that could be performed recurrently.



Figure 5.6 PPRIM device showing inserter and imager. The left image shows the inserter with a condom used to aid slide it into position. The dashed line shows where the condom is cut to not interfere with the image quality. The right image shows the device fully assembled including the inserter and imager.

5.3.4. Clinical deployment

The device was ultimately tested in healthy volunteers. The polarimetric behavior of human cervix has been previously reported^{88,89}. The intensity image (M11) can be observed in Figures 5.7 and 5.8. The healthy cervixes are highly depolarizing with a median value of 0.80 for the first *in vivo* cervix sample (Figure 5.7b) and a median value of 0.78 for the *in vivo* second cervix sample (Figure 5.8b), as expected. Moreover, for the cervix sample one the orientation as shown by the azimuth angle shows a cyclical rotation around the os (Figure 5.7c), where the black bars show the preferred angle within a 10 pixel range. The second sample (Figure 5.8c) shows the profile of a tilted cervix, where the lines show a semi-circular path of rotation with respect to the os (right top corner of the image). The saturated pixels are omitted from both sets of sample images. Healthy cervical tissue has been previously shown to be highly depolarizing and circumferentially aligned around the os, whereas pathologic tissues change in polarimetric response, showcasing a lower depolarization and alignment. These *in vivo* cervical samples reflect the results from previously reported polarimetric studies performed on healthy human cervix^{88,89,141}.

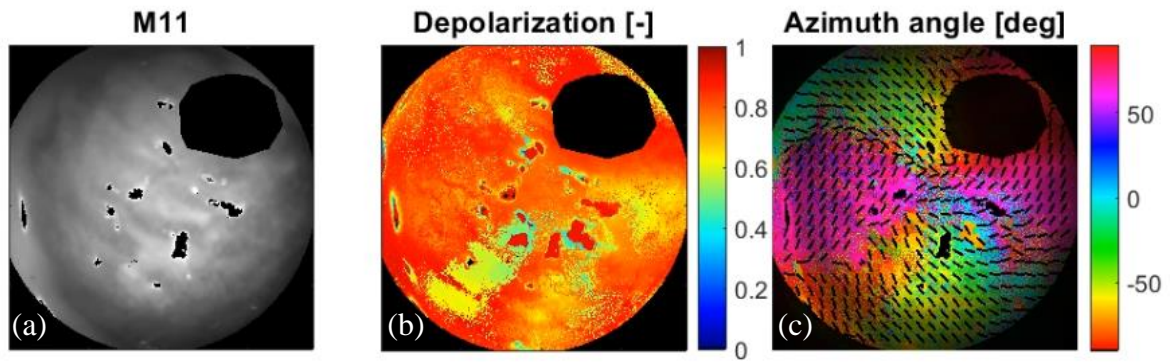


Figure 5.7 *In vivo* human cervix sample showing (a) the intensity image, M11, (b) the depolarization and (c) the orientation, as shown by the azimuth angle. The black bars indicate the preferred alignment of the tissue within a 10 pixel range.

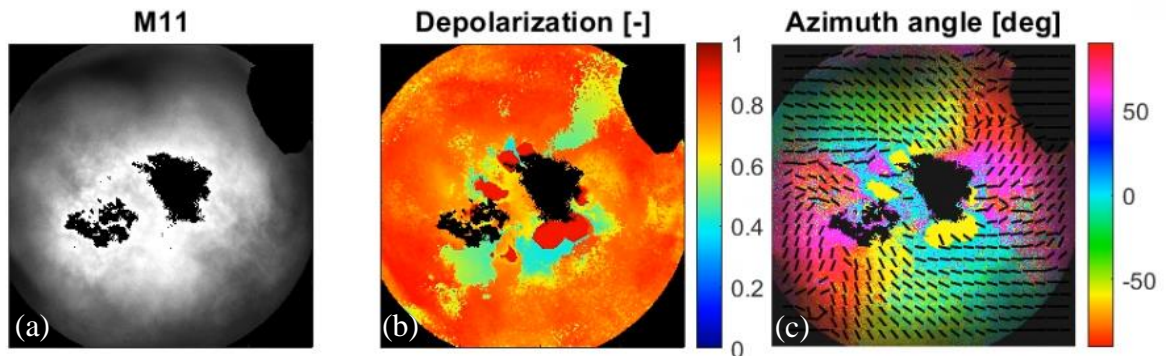


Figure 5.8 *In vivo* human cervix sample two showing (a) the intensity image, M11, (b) the depolarization and (c) the orientation, as shown by the azimuth angle. The black bars indicate the preferred alignment of the tissue within a 10 pixel range. The os can be seen as the black semi-circle in the top right corner.

As all samples show, the four cervixes exhibit an angular rotation around the os, where the tendon has a preferred angular orientation. The PPRIM is able to reproduce expected polarimetric results of biological samples using the 3 x 4 Mueller matrix decomposition.

5.4. Conclusions and future work

Polarimetric measurements provide quantitative information about sample. The device presented in this chapter uses Mueller matrix polarimetry to image and extract information of the cervix that could potentially be used in a cervical screening. The device was built to

be used with a reduced decomposition method, 3 x 4 Mueller matrix decomposition, making the compact and handheld nature possible. The low energy usage and portability could prove to be useful, especially for remote, low resource settings. Moreover, the self-imaging capabilities introduce the possibility of increased comfort during testing.

The implementation of the 3 x 4 decomposition for biological *ex vivo* and *in vivo* testing proved to be successful with the chicken tendon, porcine cervix and human cervix. The depolarization measurements were all in agreement with the reported values (all healthy tissues therefore displaying high depolarization values). Moreover, the orientation, as described by the azimuth angle, was able to display the high alignment of the chicken tendon tissue and the cyclical nature of all cervix samples. These results are in agreement with previously published studies from Chue-Sang *et al.*, Pierangelo *et al.*, Rehbinder *et al.*, and other similar work^{88,89,123,130,141}.

Testing the 3 x 4 decomposition with different types of biological tissue samples confirm the applicability of a simplified polarimetric device that can be potentially translated to clinical settings. The significance of using a quantitative measurement during cervical cancer screenings could lead to more uniform screenings worldwide, regardless of socioeconomic status. In order for this to be applied in clinical settings, the presented 3 x 4 imager needs to be tested in a larger population, as well as include subjects with pathologies to better understand the polarimetric behavior of unhealthy cervixes.

CHAPTER 6 : Conclusions

The slow progression of cervical cancer makes it a highly preventable disease with proper treatment. The high incidence worldwide—with the highest mortality rate found in developing countries due to lack of human resources to conduct screening and inadequate preventive medicine services and systems—could benefit from quantitative screening tools that aid in the interpretation of the cervical tissue's health. Mueller matrix Imaging (MMI)—also referred to as Mueller matrix polarimetry (MMP)—is an approach used to distinguish collagen fibers from images that can provide contrast of areas with irregular collagen arrangement. Precancerous tissues have shown to have lower depolarization, retardance and a decreased organization in fiber alignment as opposed to healthy tissue. This dissertation focuses on the polarimetric imaging of the uterine cervix in order to provide useful quantitative information of the function and structure of the cervical extracellular matrix (ECM).

Focusing on the limitations of low-resource settings (where cervical cancer incidence is highest), Chapter 1 delves into existing low-cost imaging methods that have been clinically deployed in the field. The devices are explored for their optical and practical specifications, such as their field of view (FOV), magnification, light source, power consumption, among other capabilities. Moreover, clinical translation of the devices is introduced and pilot study data relating to comfort, ease of use and handling are recounted.

The quantitative nature of MMP and its sensitivity to collagen (due to collagen's birefringence) makes this modality ideal for cervical imaging (principles of Mueller matrix polarimetry are presented in Chapter 2). It has been previously shown that healthy and

diseased cervical tissue behave differently with incident polarized light. Healthy cervixes show a pattern of circumferential alignment of fibers around the os. For healthy, highly aligned tissue, retardation and depolarization are expected to be high. When a cervix becomes diseased, its polarization properties change—the retardance and depolarization become lower. The wide-field capability of MMP also allows the full cervix to be captured. Chapter 3 explores of the clinical deployment in the low resource setting of a portable colposcope Mueller matrix polarimeter. The device is designed to be a snapshot Mueller matrix polarimeter, using a ring illuminator with four different states of polarization as the polarization state generator (PSG) and a combination of Savart plates along with a CMOS camera as the polarization state analyzer (PSA). The snapshot system obtains the full Mueller matrix in four images, where different Stokes vector information is spatially separated and filtered from each image. The handheld device is characterized with various *ex vivo* samples such as chicken tendon and porcine cervix and ultimately used *in vivo* in a pilot study in Mysore, India. The study imaged 22 healthy cervixes that showed the polarimetric response expected of healthy cervical tissue with the exception of one patient, which had a cervical polyp. The polarimetric response of the polyp agreed with previous reports.

The availability of new instrumentation such as polarized cameras, which have wire-grid polarizer array of repeating polarizer patterns (i.e. 0° , 45° , 90° , 135°) mounted on four adjacent pixels creating a super-pixel on board, encouraged the development of new methodology for polarimetric imaging. Previously, a full 4×4 Mueller matrix was needed to obtain the polarimetric parameters of retardance, depolarization and diattenuation. This required a PSG and PSA capable of generating and analyzing 16 different polarization state

combinations. The polarized camera simplifies the Mueller matrix acquisition by capturing all linear states simultaneously. Generating four different polarization states (i.e. 0° , 45° , 90° , right circular) with the PSG and analyzing three linear states (i.e. 0° , 45° , 90°) with the PSA, a reduced 3×4 Mueller matrix is obtained. This reduced matrix alleviates the equipment necessary to obtain quantitative information from a sample. However, in order to extract this information, a decomposition method for the reduced 3×4 Mueller matrix is needed. Chapter 4 focuses on the development, theoretical and experimental testing of this new decomposition method. The 3×4 Mueller matrix decomposition assumes there is no diattenuation present (which is true for biological tissues) and can be solved to obtain the depolarization power, retardance and azimuthal angle. The decomposition was compared to two other established 4×4 decompositions: Lu-Chipman decomposition and differential decomposition. Multiple samples were tested, including a previously published Mueller matrix, quarter waveplates (QWPs), striated silicone and a skin sample. The results for all three decompositions were in agreement.

To further test the reduced 3×4 decomposition, a handheld device that could potentially be used for self-imaging was designed. More specifically, the device is designed for cervical imaging. The device uses eight LEDs with four different polarization states as the PSG and a polarization camera as the PSA. The field of view is 25 mm, providing the capability of capturing the full cervix. Chapter 5 focuses on using the device, which implements the 3×4 decomposition method. The device was tested on multiple biological media, including *ex vivo* chicken tendon, *ex vivo* porcine cervix and *in vivo* human cervix. Polarization parameters of depolarization, retardance and azimuthal angle were obtained for all samples and compared with current literature. All samples were in accordance with

reported values showing high depolarization (as expected of healthy tissue) and characteristic fiber alignment as anticipated of each individual sample.

Polarimetric imaging of the uterine cervix would be useful to use along cervical screening since it could provide quantitative information about the tissue. The potential low-cost of a polarization based device and the previously reported polarimetric differences between healthy and neoplastic tissue could lead to a wide-reaching technology that can be implemented in low-resource settings. Further studies need to be carried to better understand the polarimetric response of pre-neoplastic tissues in its various stages. Moreover, including polarimetric imaging in cervical screenings could add quantitative information that can be routinely used to monitor cervical changes and disease progression. The work presented in this dissertation aims to further close this gap and provide a stepping-stone to accomplish this task.

References

- [1] N. Ghosh, M. F. G. Wood, and I. A. Vitkin, "Mueller matrix decomposition for extraction of individual polarization parameters from complex turbid media exhibiting multiple scattering, optical activity, and linear birefringence," *Journal of Biomedical Optics*, 13(4), 1-14, 14 (2008).
- [2] M. N. Asiedu, J. S. Agudogo, M. E. Dotson *et al.*, "A novel speculum-free imaging strategy for visualization of the internal female lower reproductive system," *Scientific Reports*, 10(1), 16570 (2020).
- [3] M. Pierce, D. Yu, and R. Richards-Kortum, "High-resolution fiber-optic microendoscopy for in situ cellular imaging," *Journal of visualized experiments : JoVE*(47), 2306 (2011).
- [4] M. Gonzalez, K. A. Montejo, K. Krupp *et al.*, "Design and implementation of a portable colposcope Mueller matrix polarimeter," *Journal of Biomedical Optics*, 25(11), 1-16 (2020).
- [5] M. Marta, C. Sonia, V. Octavio *et al.*, "Mobile colposcopy in urban and underserved suburban areas in Baja California." 9699.
- [6] M. K. Quinn, T. C. Bubi, M. C. Pierce *et al.*, "High-resolution microendoscopy for the detection of cervical neoplasia in low-resource settings," *PloS one*, 7(9), e44924-e44924 (2012).
- [7] J. Mayoore, H. Matt, H. Liming *et al.*, "Characterization of cervigram image sharpness using multiple self-referenced measurements and random forest classifiers." 10485.
- [8] H. K. Kallner, M. Persson, M. Thuresson *et al.*, "DIAGNOSTIC COLPOSCOPIC ACCURACY BY THE GYNOCLAR AND A STATIONARY COLPOSCOPE," *International Journal of Technology Assessment in Health Care*, 31(3), 181-187 (2015).
- [9] M. G. Tananant Boonya-Ananta, Vinh Nguyen Du Le, Edward DeHoog, Michael J. Paidas, Arumugam Jayakumar, Jessica C. Ramella-Roman, "A portable preterm imaging system." 11963, 8.
- [10] F. Bray, J. Ferlay, I. Soerjomataram *et al.*, "Global cancer statistics 2018: GLOBOCAN estimates of incidence and mortality worldwide for 36 cancers in 185 countries," *CA: A Cancer Journal for Clinicians*, 68(6), 394-424 (2018).
- [11] C. Y. Ashford L, [PREVENTING CERVICAL CANCER WORLDWIDE] Population Reference Bureau, (2005).
- [12] E. E. L. Jansen, N. Zielonke, A. Gini *et al.*, "Effect of organised cervical cancer screening on cervical cancer mortality in Europe: a systematic review," *European Journal of Cancer*, 127, 207-223 (2020).

- [13] T. Novikova, "Optical techniques for cervical neoplasia detection," *Beilstein Journal of Nanotechnology*, 8, 1844-1862 (2017).
- [14] B. Hill, S. F. Lam, P. Lane *et al.*, "Established and Emerging Optical Technologies for the Real-Time Detection of Cervical Neoplasia: A Review," *Journal of Cancer Therapy*, Vol.08No.13, 38 (2017).
- [15] J. Olpin, L. Chuang, J. Berek *et al.*, "Imaging and cancer of the cervix in low- and middle-income countries," *Gynecologic Oncology Reports*, 25, 115-121 (2018).
- [16] K. Taghavi, E. Rohner, P. Basu *et al.*, "Screening test accuracy of portable devices that can be used to perform colposcopy for detecting CIN2+ in low- and middle-income countries: a systematic review and meta-analysis," *BMC Women's Health*, 20(1), 253 (2020).
- [17] A. H. Rossman, H. W. Reid, M. M. Pieters *et al.*, "Digital Health Strategies for Cervical Cancer Control in Low- and Middle-Income Countries: Systematic Review of Current Implementations and Gaps in Research," *J Med Internet Res*, 23(5), e23350 (2021).
- [18] S. Sjøfteland, M. H. Sebitloane, M. Taylor *et al.*, "A systematic review of handheld tools in lieu of colposcopy for cervical neoplasia and female genital schistosomiasis," *Int. J. Gynecol. Obstet*, 153(2), 190-199 (2021).
- [19] C. Devine, C. Viswanathan, S. Faria *et al.*, "Imaging and Staging of Cervical Cancer," *Seminars in Ultrasound, CT and MRI*, 40(4), 280-286 (2019).
- [20] O. Fadare, and A. A. Roma, [Normal Anatomy of the Uterine Cervix] Springer International Publishing, Cham(2019).
- [21] R. M. Aspden, "Collagen Organisation in the Cervix and its Relation to Mechanical Function," *Collagen and Related Research*, 8(2), 103-112 (1988).
- [22] C. de Martel, M. Plummer, J. Vignat *et al.*, "Worldwide burden of cancer attributable to HPV by site, country and HPV type," *International Journal of Cancer*, 141(4), 664-670 (2017).
- [23] D. R. Lowy, D. Solomon, A. Hildesheim *et al.*, "Human papillomavirus infection and the primary and secondary prevention of cervical cancer," *Cancer*, 113(S7), 1980-1993 (2008).
- [24] J. Mirkovic, B. E. Howitt, P. Roncarati *et al.*, "Carcinogenic HPV infection in the cervical squamo-columnar junction," *The Journal of pathology*, 236(3), 265-271 (2015).
- [25] S. M. Pupa, S. Ménard, S. Forti *et al.*, "New insights into the role of extracellular matrix during tumor onset and progression," *Journal of Cellular Physiology*, 192(3), 259-267 (2002).
- [26] W. K. Hong, and M. B. Sporn, "Recent Advances in Chemoprevention of Cancer," *Science*, 278(5340), 1073 (1997).

- [27] D. E. Ingber, "Cancer as a disease of epithelial–mesenchymal interactions and extracellular matrix regulation," *Differentiation*, 70(9), 547-560 (2002).
- [28] D. Arifler, I. Pavlova, A. Gillenwater *et al.*, "Light Scattering from Collagen Fiber Networks: Micro-Optical Properties of Normal and Neoplastic Stroma," *Biophysical Journal*, 92(9), 3260-3274 (2007).
- [29] W. H. Organization, [Guidelines for screening and treatment of precancerous lesions for cervical cancer prevention], (2021).
- [30] M. H. Stoler, M. Schiffman, and G. for the Atypical Squamous Cells of Undetermined Significance–Low-grade Squamous Intraepithelial Lesion Triage Study, "Interobserver Reproducibility of Cervical Cytologic and Histologic Interpretations Realistic Estimates From the ASCUS-LSIL Triage Study," *JAMA*, 285(11), 1500-1505 (2001).
- [31] D. Dabeski, S. Duvlis, N. Basheska *et al.*, "Comparison Between HPV DNA Testing and HPV E6/E7 MRNA Testing in Women with Squamous Cell Abnormalities of the Uterine Cervix," *Pril (Makedon Akad Nauk Umet Odd Med Nauki)*, 40(1), 51-58 (2019).
- [32] M. F. Mitchell, D. Schottenfeld, G. Tortolero-Luna *et al.*, "Colposcopy for the diagnosis of squamous intraepithelial lesions: a meta-analysis," *Obstet Gynecol*, 91(4), 626-31 (1998).
- [33] I. M. Orfanoudaki, D. Kappou, and S. Sifakis, "Recent advances in optical imaging for cervical cancer detection," *Archives of Gynecology and Obstetrics*, 284(5), 1197-1208 (2011).
- [34] D. S. Ho, [Development of Optical Technologies for Comprehensive Screening of Cervical Epithelial Health] Duke University, Ann Arbor(2019).
- [35] M. Adamopoulou, E. Kalkani, E. Charvalos *et al.*, "Comparison of Cytology, Colposcopy, HPV Typing and Biomarker Analysis in Cervical Neoplasia," *Anticancer Research*, 29(8), 3401 (2009).
- [36] J. W. Sellors, P. Nieminen, E. Vesterinen *et al.*, "Observer Variability in the Scoring of Colpophotographs," *Obstetrics and gynecology (New York. 1953)*, 76(6), 1006-1008 (1990).
- [37] P. Sritipsukho, and Y. Thaweekul, "Accuracy of visual inspection with acetic acid (VIA) for cervical cancer screening: a systematic review," *J Med Assoc Thai*, 93 Suppl 7, S254-61 (2010).
- [38] M. Arbyn, R. Sankaranarayanan, R. Muwonge *et al.*, "Pooled analysis of the accuracy of five cervical cancer screening tests assessed in eleven studies in Africa and India," *International Journal of Cancer*, 123(1), 153-160 (2008).
- [39] R. Catarino, S. Schäfer, P. Vassilakos *et al.*, "Accuracy of combinations of visual inspection using acetic acid or lugol iodine to detect cervical precancer: a meta-

- analysis,” *BJOG: An International Journal of Obstetrics & Gynaecology*, 125(5), 545-553 (2018).
- [40] R. Sankaranarayanan, A. Nessa, P. O. Esmey *et al.*, “Visual inspection methods for cervical cancer prevention,” *Best Practice & Research Clinical Obstetrics & Gynaecology*, 26(2), 221-232 (2012).
- [41] A. O. Raifu, M. El-Zein, G. Sangwa-Lugoma *et al.*, “Determinants of Cervical Cancer Screening Accuracy for Visual Inspection with Acetic Acid (VIA) and Lugol’s Iodine (VILI) Performed by Nurse and Physician,” *PLOS ONE*, 12(1), e0170631 (2017).
- [42] Y. Xie, X. Tan, H. Shao *et al.*, “VIA/VILI is more suitable for cervical cancer prevention in Chinese poverty-stricken region: a health economic evaluation,” *BMC public health*, 17(1), 118-118 (2017).
- [43] Emiko Petrosky, Joseph A. Bocchini Jr, Susan Hariri *et al.*, [Use of 9-Valent Human Papillomavirus (HPV) Vaccine: Updated HPV Vaccination Recommendations of the Advisory Committee on Immunization Practices] *CDC, Morbidity and Mortality Weekly Report*(2015).
- [44] Hannah G. Rosenblum, Rayleen M. Lewis, Julia W. Gargano *et al.*, [Declines in Prevalence of Human Papillomavirus Vaccine-Type Infection Among Females after Introduction of Vaccine — United States, 2003–2018] *CDC, Morbidity and Mortality Report*(2021).
- [45] W. H. Organization, “Human papillomavirus vaccines: WHO position paper, May 2017-Recommendations,” *Vaccine*, 35(43), 5753-5755 (2017).
- [46] M. Safaean, D. Solomon, and P. E. Castle, “Cervical cancer prevention - Cervical screening: Science in evolution,” *Obstetrics and Gynecology Clinics of North America*, 34(4), 739-+ (2007).
- [47] D. B. Nikumbh, R. D. Nikumbh, and S. N. Kanthikar, “Limitations of cytological cervical cancer screening (Papanicolaou test) regarding technical and cultural aspect in rural India,” *South Asian journal of cancer*, 5(2), 79-79 (2016).
- [48] R. Gupta, S. Gupta, R. Mehrotra *et al.*, “Cervical Cancer Screening in Resource-Constrained Countries: Current Status and Future Directions,” *Asian Pacific journal of cancer prevention : APJCP*, 18(6), 1461-1467 (2017).
- [49] C. o. H. C. f. U. Women, [Cervical Cancer Screening in Low-Resource Settings] *American College of Obstetricians and Gynecologists, Obstet Gynecol* (2015).
- [50] C. Gallay, A. Girardet, M. Viviano *et al.*, “Cervical cancer screening in low-resource settings: a smartphone image application as an alternative to colposcopy,” *International journal of women's health*, 9, 455-461 (2017).

- [51] M. N. Asiedu, J. Agudogo, M. S. Krieger *et al.*, "Design and preliminary analysis of a vaginal inserter for speculum-free cervical cancer screening," *PloS one*, 12(5), e0177782 (2017).
- [52] M. N. Asiedu, A. Simhal, C. T. Lam *et al.*, "Image processing and machine learning techniques to automate diagnosis of Lugol's iodine cervigrams for a low-cost point-of-care digital colposcope." 10485, 1048508.
- [53] M. N. Asiedu, A. Simhal, U. Chaudhary *et al.*, "Development of algorithms for automated detection of cervical pre-cancers with a low-cost, point-of-care, pocket colposcope," *IEEE Transactions on Biomedical Engineering*, 66(8), 2306-2318 (2018).
- [54] T. Quang, R. A. Schwarz, S. M. Dawsey *et al.*, "A tablet-interfaced high-resolution microendoscope with automated image interpretation for real-time evaluation of esophageal squamous cell neoplasia," *Gastrointestinal endoscopy*, 84(5), 834-841 (2016).
- [55] S. Parra, E. Carranza, J. Coole *et al.*, "Development of Low-Cost Point-of-Care Technologies for Cervical Cancer Prevention Based on a Single-Board Computer," *IEEE journal of translational engineering in health and medicine*, 8, 4300210-4300210 (2020).
- [56] B. Hunt, J. H. T. G. Fregnani, R. A. Schwarz *et al.*, "Diagnosing Cervical Neoplasia in Rural Brazil Using a Mobile Van Equipped with In Vivo Microscopy: A Cluster-Randomized Community Trial," *Cancer Prevention Research*, 11(6), 359 (2018).
- [57] S. G. Parra, A. M. Rodriguez, K. D. Cherry *et al.*, "Low-cost, high-resolution imaging for detecting cervical precancer in medically-underserved areas of Texas," *Gynecol Oncol*, 154(3), 558-564 (2019).
- [58] B. D. Grant, J. H. Fregnani, J. C. Possati Resende *et al.*, "High-resolution microendoscopy: a point-of-care diagnostic for cervical dysplasia in low-resource settings," *Eur J Cancer Prev*, 26(1), 63-70 (2017).
- [59] B. Hunt, J. H. T. G. Fregnani, D. Brenes *et al.*, "Cervical lesion assessment using real-time microendoscopy image analysis in Brazil: The CLARA study," *Int. J. Cancer*, 149(2), 431-441 (2021).
- [60] P. M. Vila, C. W. Park, M. C. Pierce *et al.*, "Discrimination of Benign and Neoplastic Mucosa with a High-Resolution Microendoscope (HRME) in Head and Neck Cancer," *Annals of Surgical Oncology*, 19(11), 3534-3539 (2012).
- [61] T. J. Muldoon, D. Roblyer, M. D. Williams *et al.*, "Noninvasive imaging of oral neoplasia with a high-resolution fiber-optic microendoscope," *Head Neck*, 34(3), 305-12 (2012).

- [62] P. M. Vila, N. Thekkek, R. Richards-Kortum *et al.*, "Use of in vivo real-time optical imaging for esophageal neoplasia," *Mt Sinai J Med*, 78(6), 894-904 (2011).
- [63] M. C. Pierce, R. A. Schwarz, V. S. Bhattar *et al.*, "Accuracy of in vivo multimodal optical imaging for detection of oral neoplasia," *Cancer Prev Res (Phila)*, 5(6), 801-9 (2012).
- [64] J. C. Ramella-Roman, M. Gonzalez, J. Chue-Sang *et al.*, "Development and characterization of a snapshot Mueller matrix polarimeter for the determination of cervical cancer risk in the low resource setting." 10485, 12.
- [65] C. W. Peterson, D. Rose, J. Mink *et al.*, "Real-Time Monitoring and Evaluation of a Visual-Based Cervical Cancer Screening Program Using a Decision Support Job Aid," *Diagnostics (Basel, Switzerland)*, 6(2), 20 (2016).
- [66] G. V. Matti R, DK D'Sa, Sebag C, Peterson CW, Levitz D., "Introduction of Mobile Colposcopy as a Primary Screening Tool for Different Socioeconomic Populations in Urban India," *Pan Asian J Obs Gyn*, 2(1), 4-11 (2019).
- [67] A. Nessa, J. S. Roy, M. A. Chowdhury *et al.*, "Evaluation of the accuracy in detecting cervical lesions by nurses versus doctors using a stationary colposcope and Gynocular in a low-resource setting," *BMJ Open*, 4(11), e005313 (2014).
- [68] A. Nessa, C. Wistrand, S. A. Begum *et al.*, "Evaluation of stationary colposcope and the Gynocular, by the Swede score systematic colposcopic system in VIA positive women: a crossover randomized trial," *International journal of gynecological cancer : official journal of the International Gynecological Cancer Society*, 24(2), 339-345 (2014).
- [69] J. Ngonzi, F. Bajunirwe, C. Wistrand *et al.*, "Agreement of Colposcope and Gynocular in Assessment of Cervical Lesions by Swede Score: A Randomized, Crossover Pilot Trial," *Journal of lower genital tract disease*, 17, (2013).
- [70] P. Basu, D. Banerjee, S. Mittal *et al.*, "Evaluation of a compact, rechargeable, magnifying device to triage VIA and HPV positive women in a cervical cancer screening program in rural India," *Cancer Causes & Control*, 27(10), 1253-1259 (2016).
- [71] V. Srinivas, H. M. Nishimura, P. Jayakrishna *et al.*, "Evaluating the feasibility of utilizing Gynocular-triage-to-diagnose application with VIA (Visual inspection with Acetic acid) in community cervical cancer screening programs in rural Mysore, India," *Indian J Cancer*, (2021).
- [72] N. Singh, N. Negi, S. Sharma *et al.*, "Diagnostic Role of Portable Colposcope (Gynocular) for Diagnosis of Pre-Invasive Lesions of Cervix," *Indian Journal of Gynecologic Oncology*, 18(3), 69 (2020).
- [73] D. H. Goldstein, [Polarized Light] CRC Press, Boca Raton, 808 (2011).

- [74] J. Chue-Sang, M. Gonzalez, A. Pierre *et al.*, [Optical phantoms for biomedical polarimetry: a review] SPIE, (2019).
- [75] J. Qi, and D. S. Elson, “Mueller polarimetric imaging for surgical and diagnostic applications: a review,” J Biophotonics, 10(8), 950-982 (2017).
- [76] S.-Y. Lu, and R. A. Chipman, “Interpretation of Mueller matrices based on polar decomposition,” Journal of the Optical Society of America A, 13(5), 1106-1113 (1996).
- [77] R. Ossikovski, A. De Martino, and S. Guyot, “Forward and reverse product decompositions of depolarizing Mueller matrices,” Opt Lett, 32(6), 689-91 (2007).
- [78] R. Ossikovski, “Analysis of depolarizing Mueller matrices through a symmetric decomposition,” Journal of the Optical Society of America A, 26(5), 1109-1118 (2009).
- [79] N. Ortega-Quijano, and J. L. Arce-Diego, “Mueller matrix differential decomposition,” Optics Letters, 36(10), 1942-1944 (2011).
- [80] R. Ossikovski, “Differential matrix formalism for depolarizing anisotropic media,” Optics Letters, 36(12), 2330-2332 (2011).
- [81] M. K. Swami, S. Manhas, P. Buddhiwant *et al.*, “Polar decomposition of 3×3 Mueller matrix: a tool for quantitative tissue polarimetry,” Optics Express, 14(20), 9324-9337 (2006).
- [82] Y. Wang, Y. Guo, N. Zeng *et al.*, “Study on the validity of 3×3 Mueller matrix decomposition,” Journal of Biomedical Optics, 20(6), 1-7, 7 (2015).
- [83] J. C. Ramella-Roman, I. Saytashev, and M. Piccini, “A review of polarization-based imaging technologies for clinical and preclinical applications,” Journal of Optics, 22(12), 123001 (2020).
- [84] N. Ghosh, and I. A. Vitkin, “Tissue polarimetry: concepts, challenges, applications, and outlook,” J Biomed Opt, 16(11), 110801 (2011).
- [85] W. Kang, X. Qi, N. J. Tresser *et al.*, “Diagnostic efficacy of computer extracted image features in optical coherence tomography of the precancerous cervix,” Med Phys, 38(1), 107-13 (2011).
- [86] I. M. Orfanoudaki, D. Kappou, and S. Sifakis, “Recent advances in optical imaging for cervical cancer detection,” Arch Gynecol Obstet, 284(5), 1197-208 (2011).
- [87] S. W. Lee, J. Y. Yoo, J. H. Kang *et al.*, “Optical diagnosis of cervical intraepithelial neoplasm (CIN) using polarization-sensitive optical coherence tomography,” Opt Express, 16(4), 2709-19 (2008).

- [88] J. Vizet, J. Rehbinder, S. Deby *et al.*, “In vivo imaging of uterine cervix with a Mueller polarimetric colposcope,” *Scientific Reports*, 7(1), 2471 (2017).
- [89] J. Chue-Sang, N. Holness, M. Gonzalez *et al.*, "Use of Mueller matrix colposcopy in the characterization of cervical collagen anisotropy." 23, 9.
- [90] M. Zaffar, and A. Pradhan, “Assessment of anisotropy of collagen structures through spatial frequencies of Mueller matrix images for cervical pre-cancer detection,” *Applied Optics*, 59(4), 1237-1248 (2020).
- [91] I. Pavlova, K. Sokolov, R. Drezek *et al.*, “Microanatomical and Biochemical Origins of Normal and Precancerous Cervical Autofluorescence Using Laser-scanning Fluorescence Confocal Microscopy ¶,” *Photochemistry and Photobiology*, 77(5), 550-555 (2003).
- [92] Centers for Disease Control and Prevention, “Fighting Cervical Cancer Worldwide,” Found at: https://www.cdc.gov/cancer/gynecologic/what_cdc_is_doing/cc_worldwide.htm Accessed on February 15, 2017, (2014).
- [93] ICO HPV Information Centre, [Human Pappaloma Virus and Related Disease Report: Figure 2. Population pyramids by World, developing and developed regions, estimates for 2015] Found at: <http://www.hpvcentre.net/statistics/reports/XWX.pdf>, (2016).
- [94] World Health Organization, “Human papillomavirus vaccines: WHO position paper, October 2014-Recommendations.,” *Vaccine*, 33(36), 4383-4 (2015).
- [95] B.-R. L. Bruni L, Albero G, Serrano B, Mena M, Gómez D, Muñoz J, Bosch FX, de Sanjosé S, , [Human Papillomavirus and Related Diseases in India. Summary Report 15 December 2016] ICO Information Centre on HPV and Cancer (HPV Information Centre). , (2016).
- [96] A. Sreedevi, R. Javed, and A. Dinesh, “Epidemiology of cervical cancer with special focus on India,” *Int J Womens Health*, 7, 405-14 (2015).
- [97] K. Kaarthigeyan, “Cervical cancer in India and HPV vaccination,” *Indian J Med Paediatr Oncol*, 33(1), 7-12 (2012).
- [98] Barot S, [Preventing Cervical Cancer: New Resources To Advance the Domestic and Global Fight] Gutmacher Institute, (2012).
- [99] Kerala Department of Health and Family Welfare, “Guidelines for Cancer Care,” Found at: <http://dhs.kerala.gov.in/docs/orders/go346.pdf> Accessed on February 13, 2017, (2013).
- [100] B. P. Poli UR, Gowrishankar S., “Visual Inspection with Acetic Acid (VIA) Screening Program: 7 Years Experience in Early Detection of Cervical Cancer and Pre-Cancers in Rural South India. ,” *Indian Journal of Community Medicine* 40(3), 203-207 (2015).

- [101] N. Bhatla, A. Mukhopadhyay, S. Joshi *et al.*, “Visual inspection for cervical cancer screening: evaluation by doctor versus paramedical worker,” *Indian J Cancer*, 41(1), 32-6 (2004).
- [102] M. Arbyn, R. Sankaranarayanan, R. Muwonge *et al.*, “Pooled analysis of the accuracy of five cervical cancer screening tests assessed in eleven studies in Africa and India,” *Int J Cancer*, 123(1), 153-60 (2008).
- [103] R. Sankaranarayanan, A. Nessa, P. O. Esmay *et al.*, “Visual inspection methods for cervical cancer prevention,” *Best Pract Res Clin Obstet Gynaecol*, 26(2), 221-32 (2012).
- [104] PHASE Worldwide, “**Reducing The Worldwide Burden Of Cervical Cancer: The Nepal Experience**,” Found at: <http://dhs.kerala.gov.in/docs/orders/go346.pdf> Accessed on February 13, 2017.
- [105] S. Singla, S. Mathur, A. Kriplani *et al.*, “Single visit approach for management of cervical intraepithelial neoplasia by visual inspection & loop electrosurgical excision procedure,” *Indian J Med Res*, 135(5), 614-20 (2012).
- [106] B. D. Grant, R. A. Schwarz, T. Quang *et al.*, “High-resolution microendoscope for the detection of cervical neoplasia,” *Methods Mol Biol*, 1256, 421-34 (2015).
- [107] M. K. Quinn, T. C. Bubi, M. C. Pierce *et al.*, “High-resolution microendoscopy for the detection of cervical neoplasia in low-resource settings,” *PLoS One*, 7(9), e44924 (2012).
- [108] N. Ramanujam, M. F. Mitchell, A. Mahadevan *et al.*, “Fluorescence spectroscopy: a diagnostic tool for cervical intraepithelial neoplasia (CIN),” *Gynecol Oncol*, 52(1), 31-8 (1994).
- [109] C. T. Lam, M. S. Krieger, J. E. Gallagher *et al.*, “Design of a Novel Low Cost Point of Care Tampon (POCKeT) Colposcope for Use in Resource Limited Settings,” *PLoS One*, 10(9), e0135869 (2015).
- [110] C. W. Peterson, D. Rose, J. Mink *et al.*, “Real-Time Monitoring and Evaluation of a Visual-Based Cervical Cancer Screening Program Using a Decision Support Job Aid,” *Diagnostics*, 6(2), (2016).
- [111] E. Hecht, [Optics] Addison-Wesley, Reading, Mass.(2002).
- [112] Z. M. Wang, X. Y. Jiao, and X. Xing, “[Tissue engineering of skin],” *Zhongguo Xiu Fu Chong Jian Wai Ke Za Zhi*, 14(4), 241-4 (2000).
- [113] A. Blaustein, and K. J. Kurman, [Blaustein's pathology of the female genital tract], New York, NY(2011).
- [114] M. House, D. L. Kaplan, and S. Socrate, “Relationships between mechanical properties and extracellular matrix constituents of the cervical stroma during pregnancy,” *Semin Perinatol*, 33(5), 300-7 (2009).

- [115] R. M. Aspden, "Collagen organisation in the cervix and its relation to mechanical function," *Coll Relat Res*, 8(2), 103-12 (1988).
- [116] K. M. Myers, H. Feltovich, E. Mazza *et al.*, "The mechanical role of the cervix in pregnancy," *J Biomech*, 48(9), 1511-23 (2015).
- [117] M. Fernandez, M. House, S. Jambawalikar *et al.*, "Investigating the mechanical function of the cervix during pregnancy using finite element models derived from high-resolution 3D MRI," *Computer Methods in Biomechanics and Biomedical Engineering*, 19(4), 404-417 (2016).
- [118] K. Yoshida, H. Jiang, M. Kim *et al.*, "Quantitative Evaluation of Collagen Crosslinks and Corresponding Tensile Mechanical Properties in Mouse Cervical Tissue during Normal Pregnancy," *PLoS ONE*, 9(11), e112391 (2014).
- [119] A. Pierangelo, S. Manhas, A. Benali *et al.*, "Multispectral Mueller polarimetric imaging detecting residual cancer and cancer regression after neoadjuvant treatment for colorectal carcinomas," *J Biomed Opt*, 18(4), 046014 (2013).
- [120] J. Dillet, C. Baravian, F. Caton *et al.*, "Size determination by use of two-dimensional Mueller matrices backscattered by optically thick random media," *Applied Optics*, 45(19), 4669-4678 (2006).
- [121] S. Y. Lu, and R. A. Chipman, "Interpretation of Mueller matrices based on polar decomposition," *Journal of the Optical Society of America a-Optics Image Science and Vision*, 13(5), 1106-1113 (1996).
- [122] M. F. Wood, X. Guo, and I. A. Vitkin, "Polarized light propagation in multiply scattering media exhibiting both linear birefringence and optical activity: Monte Carlo model and experimental methodology," *J Biomed Opt*, 12(1), 014029 (2007).
- [123] A. Pierangelo, A. Nazac, A. Benali *et al.*, "Polarimetric imaging of uterine cervix: a case study," *Opt Express*, 21(12), 14120-30 (2013).
- [124] J. Rehbinder, H. Haddad, S. Deby *et al.*, "Ex vivo Mueller polarimetric imaging of the uterine cervix: a first statistical evaluation," *Journal of Biomedical Optics*, 21(7), (2016).
- [125] C. He, H. H. He, J. T. Chang *et al.*, "Characterizing microstructures of cancerous tissues using multispectral transformed Mueller matrix polarization parameters," *Biomedical Optics Express*, 6(8), 2934-2945 (2015).
- [126] A. Pierangelo, A. Nazac, A. Benali *et al.*, "Polarimetric imaging of uterine cervix: a case study," *Optics Express*, 21(12), 14120-14130 (2013).
- [127] J. Chue-Sang, Y. Q. Bai, S. Stoff *et al.*, "Use of Mueller matrix polarimetry and optical coherence tomography in the characterization of cervical collagen anisotropy," *Journal of Biomedical Optics*, 22(8), (2017).

- [128] S. Stoff, J. Chue-Sang, N. A. Holness *et al.*, "Cervical Collagen Imaging for Determining Preterm Labor Risks Using a Colposcope with Full Mueller Matrix Capability," *Photonic Therapeutics and Diagnostics Xii*, 9689, (2016).
- [129] J. Chue-Sang, and J. C. Ramella-Roman, "Mueller matrix colposcope for in-vivo cervical collagen imaging of the uterine-cervix," *Proceedings of the SPIE*, In Print, (2017).
- [130] J. Chue-Sang, Y. Bai, S. Stoff *et al.*, "Use of Mueller matrix polarimetry and optical coherence tomography in the characterization of cervical collagen anisotropy," *J Biomed Opt*, 22(8), 1-9 (2017).
- [131] Q. Cao, J. Zhang, E. DeHoog *et al.*, "Demonstration of snapshot imaging polarimeter using modified Savart polariscopes," *Appl Opt*, 55(5), 954-9 (2016).
- [132] Q. Cao, C. Zhang, and E. DeHoog, "Snapshot imaging polarimeter using modified Savart polariscopes," *Appl Opt*, 51(24), 5791-6 (2012).
- [133] S. Murali, [Analysis of an interferometric Stokes imaging polarimeter], (2010).
- [134] M. Takeda, H. Ina, and S. Kobayashi, "Fourier-transform method of fringe-pattern analysis for computer-based topography and interferometry," *Journal of the Optical Society of America*, 72(1), 156-160 (1982).
- [135] H. Luo, K. Oka, E. DeHoog *et al.*, "Compact and miniature snapshot imaging polarimeter," *Applied Optics*, 47(24), 4413-4417 (2008).
- [136] Q. Cao, C. Zhang, and E. DeHoog, "Snapshot imaging polarimeter using modified Savart polariscopes," *Applied Optics*, 51(24), 5791-5796 (2012).
- [137] Q. Cao, J. Zhang, E. DeHoog *et al.*, "Demonstration of snapshot imaging polarimeter using modified Savart polariscopes," *Applied Optics*, 55(5), 954-959 (2016).
- [138] N. Saito, S. Odate, K. Otaki *et al.*, "Wide field snapshot imaging polarimeter using modified Savart plates." 8873, 7.
- [139] K. Oka, and N. Saito, "Snapshot complete imaging polarimeter using Savart plates." 6295, 7.
- [140] T. Novikova, A. Pierangelo, A. De Martino *et al.*, "Polarimetric Imaging for Cancer Diagnosis and Staging," *Optics and Photonics News*, 23(10), 26-33 (2012).
- [141] J. Rehbinder, H. Haddad, S. Deby *et al.*, "Ex vivo Mueller polarimetric imaging of the uterine cervix: a first statistical evaluation," *J Biomed Opt*, 21(7), 71113 (2016).
- [142] N. Ghosh, and A. I. Vitkin, "Tissue polarimetry: concepts, challenges, applications, and outlook." 16, 30.

- [143] G. A. Atkinson, and J. D. Ernst, “High-sensitivity analysis of polarization by surface reflection,” *Machine Vision and Applications*, 29(7), 1171-1189 (2018).
- [144] J. Qi, C. He, and D. S. Elson, “Real time complete Stokes polarimetric imager based on a linear polarizer array camera for tissue polarimetric imaging,” *Biomedical Optics Express*, 8(11), 4933-4946 (2017).
- [145] X. Ma, F. Dong, Z. Zhang *et al.*, “Pixelated-polarization-camera-based polarimetry system for wide real-time optical rotation measurement,” *Sensors and Actuators B Chemical*, (2018).
- [146] R. David, R. Maik, and N. Gunther, "Principle investigations on polarization image sensors." 11144.
- [147] H. Nathan, S. Shuhei, and O. Yukitoshi, “Generating high-performance polarization measurements with low-performance polarizers: demonstration with a microgrid polarization camera,” *Optical Engineering*, 58(8), 1-4 (2019).
- [148] A. H. Nathan, S. Shuhei, and O. Yukitoshi, “Calibration and performance assessment of microgrid polarization cameras,” *Optical Engineering*, 58(8), 1-9 (2019).
- [149] H. Ren, J. Yang, X. Liu *et al.*, “Sensor Modeling and Calibration Method Based on Extinction Ratio Error for Camera-Based Polarization Navigation Sensor,” *Sensors (Basel, Switzerland)*, 20(13), 3779 (2020).
- [150] M. Sarkar, D. S. Segundo Bello, C. van Hoof *et al.*, “Biologically inspired autonomous agent navigation using an integrated polarization analyzing CMOS image sensor,” *Procedia Engineering*, 5, 673-676 (2010).
- [151] T. C. Wood, and D. S. Elson, “Polarization response measurement and simulation of rigid endoscopes,” *Biomed Opt Express*, 1(2), 463-470 (2010).
- [152] K. Satish, P. Harsh, O. Razvigor *et al.*, “Comparative study of differential matrix and extended polar decomposition formalisms for polarimetric characterization of complex tissue-like turbid media,” *Journal of Biomedical Optics*, 17(10), 1-12 (2012).
- [153] J. Vizet, and R. Ossikovski, “Symmetric decomposition of experimental depolarizing Mueller matrices in the degenerate case,” *Applied Optics*, 57(5), 1159-1167 (2018).
- [154] J. Qi, M. Ye, M. Singh *et al.*, “Narrow band 3×3 Mueller polarimetric endoscopy,” *Biomedical Optics Express*, 4(11), 2433-2449 (2013).
- [155] H. R. Lee, T. S. H. Yoo, P. Li *et al.*, [Mueller microscopy of anisotropic scattering media: theory and experiments] *SPIE, EPE* (2018).
- [156] I. Saytashev, S. Saha, J. Chue-Sang *et al.*, “Self validating Mueller matrix Micro-Mesoscope (SAMMM) for the characterization of biological media,” *Optics Letters*, 45(8), 2168-2171 (2020).

- [157] N. Ghosh, [Correction on reported depolarization values for Ghosh et al., JBO 2008. Table 1 reported depolarization $\Delta=0.995$ should be $\Delta=0.005$.], (2021).
- [158] GLOBOCAN, [Cervical Cancer: Estimated Incidence, Mortality and Prevalence Worldwide in 2012], (2012).
- [159] M. Watson, V. Benard, J. King *et al.*, “National assessment of HPV and Pap tests: Changes in cervical cancer screening, National Health Interview Survey,” *Preventive medicine*, 100, 243-247 (2017).
- [160] K. L. MacLaughlin, R. M. Jacobson, C. Radecki Breitkopf *et al.*, “Trends Over Time in Pap and Pap-HPV Cotesting for Cervical Cancer Screening,” *J Womens Health (Larchmt)*, 28(2), 244-249 (2019).
- [161] C. Hoyo, K. S. H. Yarnall, C. S. Skinner *et al.*, “Pain predicts non-adherence to pap smear screening among middle-aged African American women,” *Preventive Medicine*, 41(2), 439-445 (2005).
- [162] D. A. Seehusen, D. R. Johnson, J. S. Earwood *et al.*, “Improving women's experience during speculum examinations at routine gynaecological visits: randomised clinical trial,” *BMJ: British Medical Journal*, 333(7560), 171-173 (2006).
- [163] R. Boddien-Heidrich, S. Walter, S. Teutenberger *et al.*, “What does a young girl experience in her first gynecological examination? Study on the relationship between anxiety and pain,” *J Pediatr Adolesc Gynecol*, 13(3), 139-42 (2000).
- [164] G. S. McPherson, P. Fairbairn-Dunlop, and D. Payne, “Overcoming Barriers to Cervical Screening Among Pacific Women: A Narrative Review,” *Health equity*, 3(1), 22-29 (2019).
- [165] G. Aasbø, K. N. Solbrække, J. Waller *et al.*, “Perspectives of non-attenders for cervical cancer screening in Norway: a qualitative focus group study,” *BMJ Open*, 9(8), e029505 (2019).
- [166] M. Ferdous, S. Lee, S. Goopy *et al.*, “Barriers to cervical cancer screening faced by immigrant women in Canada: a systematic scoping review,” *BMC women's health*, 18(1), 165-165 (2018).
- [167] D. Y. Morales-Campos, S. A. Snipes, E. K. Villarreal *et al.*, “Cervical cancer, human papillomavirus (HPV), and HPV vaccination: exploring gendered perspectives, knowledge, attitudes, and cultural taboos among Mexican American adults,” *Ethnicity & Health*, 1-19 (2018).
- [168] D. Wright, J. Fenwick, P. Stephenson *et al.*, “Speculum ‘self-insertion’: a pilot study,” *Journal of Clinical Nursing*, 14(9), 1098-1111 (2005).
- [169] A. Adcock, F. Cram, B. Lawton *et al.*, “Acceptability of self-taken vaginal HPV sample for cervical screening among an under-screened Indigenous population,”

Australian and New Zealand Journal of Obstetrics and Gynaecology, 59(2), 301-307 (2019).

- [170] J. R. Mourant, T. J. Bocklage, T. M. Powers *et al.*, "In vivo light scattering measurements for detection of precancerous conditions of the cervix," Gynecologic Oncology, 105(2), 439-445 (2007).
- [171] C. T. Lam, M. S. Krieger, J. E. Gallagher *et al.*, "Design of a Novel Low Cost Point of Care Tampon (POCkeT) Colposcope for Use in Resource Limited Settings," PloS one, 10(9), e0135869-e0135869 (2015).
- [172] J. L. Mueller, C. T. Lam, D. Dahl *et al.*, "Portable Pocket colposcopy performs comparably to standard-of-care clinical colposcopy using acetic acid and Lugol's iodine as contrast mediators: an investigational study in Peru," BJOG : an international journal of obstetrics and gynaecology, 125(10), 1321-1329 (2018).
- [173] W. P. Curtis, M. Jonah, and L. David, "Measurement and evaluation of digital cervicography programs in two cervical cancer screening camps in East Africa." 10055.
- [174] M. Underwood, M. Arbyn, W. Parry-Smith *et al.*, "Accuracy of colposcopy-directed punch biopsies: a systematic review and meta-analysis," BJOG: An International Journal of Obstetrics & Gynaecology, 119(11), 1293-1301 (2012).
- [175] J. Chue-Sang, Y. Bai, S. Stoff *et al.*, "Use of Mueller matrix polarimetry and optical coherence tomography in the characterization of cervical collagen anisotropy," Journal of Biomedical Optics, 22, 9 (2017).
- [176] J. Chue-Sang, Y. Bai, S. Stoff *et al.*, "Use of Mueller matrix polarimetry and optical coherence tomography in the characterization of cervical collagen anisotropy." 10043, 11.
- [177] J. Chue-Sang, Y. Bai, S. Stoff *et al.*, "Use of combined polarization-sensitive optical coherence tomography and Mueller matrix imaging for the polarimetric characterization of excised biological tissue," Journal of Biomedical Optics, 21(7), 071109-071109 (2016).

VITA

MARIACARLA GONZALEZ

Born, La Habana, Cuba

2010-2014

B.S., Chemistry
Florida International University
Miami, Florida

2015-2022

M.S. and Ph.D., Biomedical Engineering
Florida International University
Miami, Florida

PUBLICATIONS, PRESENTATIONS AND PROCEEDINGS

- Mariacarla Gonzalez, Razvigor Ossikovski, Tatiana Novikova *et al.*, *Introduction of a 3 x 4 Mueller matrix decomposition method*, Journal of Physics D: Applied Physics, (2021).
- Mariacarla Gonzalez, Karla Alejandra Montejo, Karl Krupp, Vijaya Srinivas, Edward DeHoog, Purnima Madhivanan, Jessica C. Ramella-Roman, *Design and implementation of a portable colposcope Mueller matrix polarimeter*, J. Biomed. Opt. 25(11), 116006 (2020), doi: 10.1117/1.JBO.25.11.116006.
- Joseph Chue-Sang, Mariacarla Gonzalez, Angie Pierre, Megan Laughrey, Ilyas Saytashev, Tatiana Novikova, Jessica C. Ramella-Roman, *Optical phantoms for biomedical polarimetry: a review*, J. Biomed. Opt. 24(3) 030901 (8 March 2019)
- Joseph Chue-Sang, Nola Holness, Mariacarla Gonzalez, Joan Greaves, Ilyas Saytashev, Susan Stoff, Amir Gandjbakhche, Viktor V. Chernomordik, Gene Burkett, Jessica C. Ramella-Roman, *Use of Mueller matrix colposcopy in the characterization of cervical collagen anisotropy*, J. Biomed. Opt. 23(12) 121605 (2018)
- J. Chue-Sang, Yuqian Bai, Susan Stoff, Mariacarla Gonzalez, Jefferson Gomes, Amir Gandjbakhche, Viktor V. Chernomordik, Jessica C. Ramella-Roman., *Use of Mueller matrix polarimetry and optical coherence tomography in the characterization of cervical collagen anisotropy*. J Biomed Opt 22, 1-9 (2017).
- Mariacarla Gonzalez, Camilo Roa, Arturo Jimenez, Rachelle Gomez-Guevara, V. N. Du Le, Tatiana Novikova, Jessica C. Ramella-Roman, *Machine learning powered Mueller matrix microscope for collagen and elastin visualization in the mouse cervix*, Proc. SPIE 11963, Polarized Light and Optical Angular Momentum for Biomedical Diagnostics

2022, (January 23 2022).

- Mariacarla Gonzalez, Ilyas Saytashev, Camila Luna, Brittany Gonzalez, Alejandro Pinero, Manuel Perez, Sharan Ramaswamy, Jessica Ramella-Roman, *Multiphoton microscopy of ECM proteins in baboon aortic leaflet*, Proc. SPIE 10471, Diagnostic and Therapeutic Applications of Light in Cardiology 2018, 104710Y (22 February 2018).

Jessica C. Ramella-Roman, Mariacarla Gonzalez, Joseph Chue-Sang , Karla Montejo, Karl Krup, Vijaya Srinivas, Edward DeHoog, and Purnima Madhivanan, *Development and characterization of a snapshot Mueller matrix polarimeter for the determination of cervical cancer risk in the low resource setting*, Proc. SPIE 10485, Optics and Biophotonics in Low-Resource Settings IV, 104850X ; doi:10.1117/12.2290592. (7 April 2018)

- Mariacarla Gonzalez, Nicole Sevilla, Joseph Chue-Sang, Jessica C. Ramella-Roman., *Quantitative analysis of a scar's pliability, perfusion and metrology*. Proc. SPIE 10067, Optical Elastography and Tissue Biomechanics IV, 100670R (March 2, 2017); doi:10.1117/12.2252676

- Mariacarla Gonzalez, Karla Montejo, Karl Krupp, Vijaya Srinivas, Edward DeHoog, Joseph Chue-Sang, Purnima Madhivanan, and Jessica Ramella-Roman, *Portable, low-cost polarimeter for cervical health diagnosis*, 9th Annual Global Health Conference 2019, Miami, FL May 8, 2019 (Poster presentation)

- Mariacarla Gonzalez, Karla Montejo, Karl Krupp, Vijaya Srinivas, Edward DeHoog, Joseph Chue-Sang, Purnima Madhivanan, and Jessica Ramella-Roman, *Calibration of Low Cost, Portable Mueller Matrix Polarimeter*, in Biophotonics Congress: Biomedical Optics Congress 2018. April 3, 2018. (Poster presentation)

- Mariacarla Gonzalez, Karla Montejo, Karl Krupp, Vijaya Srinivas, Edward DeHoog, Joseph Chue-Sang, Purnima Madhivanan, and Jessica Ramella-Roman, *Low Cost, Portable Mueller Matrix Polarimeter for Cervical Health Determination*, Gordon Research Conference, Lewiston, ME July 14, 2018 (Poster presentation)